Verification of an XFEM Based Slope Stability Analysis Method

by

Stan B. den Hartog

Verification of an XFEM Based Slope Stability Analysis Method

by

Stan B. den Hartog

to obtain the degree of Master of Science
at the Delft University of Technology

Student number: 4594053
Project duration: August 10, 2020 – May 28, 2021
Thesis committee:

Dr. ir. M.A.N. Hendriks,	TU Delft, chair
Dr. ir. F.P. van der Meer,	TU Delft
Dr. P.J. Vardon,	TU Delft
Dr. ir. G. Schreppers,	Diana FEA, supervisor

TU Delft

Abstract

There are multiple numerical methods for analysing the stability of slopes. Commonly used methods for assessing the slope stability are the slip surface method, strength reduction methods or methods based on load increments. What those methods have in common is that the stability of a slope is assessed by a factor of safety or critical stability number. These dimensionless factors give an indication of the global stability of a slope. A critical stability number is computed through load increments while a factor of safety is based on the strength parameters of the soil.

A relatively new XFEM-based method for analysing slope stability is being implemented in the finite element software of Diana FEA. Unique with respect to the other methods is that this method detects onset of localisation and captures the propagation of the slip surface. Therefore, this method is referred to as the propagation method in this work.

The propagation method consist of three main procedure steps. First, onset of localisation is detected during incremental loading of the model and the direction of the localisation plain is obtained. In step two, enrichment elements are implemented at the location of localisation, which are able to reproduce a jump in the displacement field. This is followed by a search algorithm for detection of localisation in adjacent elements. From here on, the implementation of the enrichment elements continues till a fully developed slip surface is present, resulting in global failure of the slope.

Those procedure steps need to be tested and verified. The objective of this thesis is to verify onset of localisation on element level and to provide a method for verification of the point of global failure in analyses with the propagation method.

Onset of localisation is verified with analytical expressions and with numerical results. A critical stability number is used to assess the slope stability in analyses with the propagation method. A relation between the critical stability number and the factor of safety is needed, to be able to compute a factor of safety with the propagation method which is similar to a factor of safety of the slip surface method and a strength reduction method.

This relation is obtained through the definitions of those factors. This creates possibilities to asses the stability of a slope with the propagation method by a factor of safety and this factor of safety can be verified with the results of a strength reduction method and a slip surface method.

In addition, benchmarks are generated with the aforementioned slope stability analysis methods, which can be used for verification of the factor of safety of the propagation method. The benchmarks are the result of parameter and convergence studies. In the parameter studies, the effect of the Poisson ratio and the dilatancy angle on the factor of safety is studied. This is done by computing the maximum vertical displacements during stability analyses with various values of the Poisson ratio and the dilatancy angle. Those displacements are plotted versus the corresponding factor of safety. The resulting plots provide characteristic information which can be used for verification of the propagation method.

The convergence studies are performed in order to obtain reliable factors of safety that can serve as a benchmark. The factors of safety are computed for various mesh sizes and different convergence criteria. From the results, a reliable factor of safety is obtained that can be used as a benchmark for the corresponding finite element model.

In the end, a development version of the propagation method is tested and the results are verified with a benchmark which is generated with a finite element model containing interface elements.

Acknowledgements

There are many people I want to give my gratitude. First, I would like to thank Gerd-Jan Schreppers. He gave me the opportunity for working on my thesis at Diana FEA. As my daily supervisor, he planted good ideas in my mind by asking the right questions, for me to be able to create this thesis and to keep me on track. I want to thank him for his trust and time he invested in me.

Next, I want to thank Max Hendriks as the chairman of my thesis committee. Thanks to him, I was brought in contact with Gerd-Jan. He also always had a quick response to my delivered work, which he revisited with a critical eye. As members of my thesis committee, I also want to thank Frans van der Meer and Phil Vardon for their time and knowledge.

Many thanks to the members of the Diana FEA company, especially to Wijtze Pieter Kikstra, Mehdi Arzanfudi, Tanvir Rahman and Arno Wolthers for answering my questions and for sharing their wisdom. I was always treated as an equal member of the Diana FEA company and my questions were taken seriously.

Special thanks to Pieter Hofman, for stimulating me and motivating me. Without him, I would never be on the level I am today and thanks to him I started my engineering path at TU Delft. Thank you for all the countless sparring sessions we had and for all the joy and fun you brought during our study journey.

Not everything in life is about becoming a better engineer, it is also about becoming a better person and enjoying life. Therefore I cannot give enough gratitude to Kaya Azimi. Thank you for all the love and beautiful times you gave me. You made my journey brighter and you are the reason for me to becoming a better person.

In the end I want to thank my friends and family and especially my parents, who supported me in every possible way. I want to thank them for their trust, patience and financial support.

Stan den Hartog
Nieuwegein, March 2021

Contents

1 Introduction 1
- 1.1 Background . . . 1
- 1.2 Thesis objective . . . 2
- 1.3 Scope of the thesis . . . 3
- 1.4 Derivation of initiation conditions of localisation . . . 3
- 1.5 Analysis methods . . . 7
- 1.6 Solution procedure . . . 8
- 1.7 Thesis outline . . . 9

2 Analysis methods 11
- 2.1 The slip surface method . . . 11
- 2.2 The strength reduction method and the manual strength reduction method . . . 12
- 2.3 The single load increment method and the multiple load increment method . . . 13
- 2.4 Models with interface elements . . . 14
- 2.5 The extended finite element method (XFEM) . . . 14
  - 2.5.1 FEM formulations . . . 15
  - 2.5.2 Enrichment functions for discontinuities . . . 15
  - 2.5.3 XFEM applied in the PM . . . 16

3 Application of the analysis methods 19
- 3.1 Application of methods based on strength reduction . . . 20
- 3.2 Application of methods based on load increments . . . 22
- 3.3 Convergence and parameter studies . . . 23
- 3.4 Relation between methods based on strength reduction and methods based on load increment . . . 23

4 Benchmarks generated with analyses based on strength reduction 27
- 4.1 Effect of the Poisson ratio on the FOS . . . 27
- 4.2 Convergence study . . . 29
- 4.3 Conclusions . . . 32

5 Benchmarks generated with analyses based on load increments 35
- 5.1 Effect of the dilatancy angle on the CSN . . . 35
- 5.2 Convergence study . . . 37
- 5.3 Interface models with linear continuum elements . . . 38
- 5.4 Conclusions . . . 41

6 Verification of the propagation method 43
- 6.1 Verification of onset of localisation . . . 43
  - 6.1.1 Finite element model . . . 43
  - 6.1.2 Numerical results . . . 44
  - 6.1.3 Analytical solutions . . . 47
  - 6.1.4 Conclusions . . . 50
- 6.2 Verification of the propagation method on global level . . . 51
  - 6.2.1 FE-model . . . 51
  - 6.2.2 Testing the development version of the propagation method . . . 51
  - 6.2.3 Discussion . . . 53
  - 6.2.4 Conclusions . . . 54

7 Discussion and conclusions 55
- 7.1 Discussion and conclusions . . . 55
- 7.2 Expectations and recommendations . . . 56

A XFEM examples 59
A.1 The problem . . . 59
A.2 Approximation with standard FEM . . . 60
A.3 Approximation with XFEM . . . 60
A.4 Implementation of XFEM . . . 61
B Slip surface geometry verification 71
C Results Leroy and Ortiz 73
Bibliography 75

1

Introduction

1.1. Background

Stability of a slope is lost when a part of the slope is failing along a slip surface. This process is the result of localisation. Localisation is the process where a smooth displacement field suddenly gives rise to large strains which are localised in narrow bands [26]. As the word implies, localisation starts locally, which is called onset of localisation. The onset of localisation is a well understood phenomena and can be derived mathematically. The progression of localisation may eventually result in global failure along a slip surface.

There are multiple numerical methods for analysing the stability of a slope. These numerical methods compute a factor of safety (FOS) and this FOS gives an indication of the stability of a slope. When the value is equal or larger than one, the slope is stable and when the value is smaller than one, the slope is unstable.

The software of Diana FEA has two built-in functions for analysing slope stability. One of those methods is the slip surface method (SSM). The slip surface method computes a robust estimate of the FOS and is relatively simple to implement, but the method is only based on post-processing of the stresses. Therefore, the method provides no information about the kinematics after failure of the slope. The other method is the strength reduction method (SRM), which computes the FOS by reducing the internal friction angle of the soil and the cohesion by a factor in an iterative procedure. The FOS is obtained if the model cannot converge in a certain amount of iterations and if a user specified norm for the FOS is reached. An advantage of the SRM is that non-uniform stress situations can be used as an initial loading stage of the ground. However, the analysis is computationally expensive due to this iterative procedure for computing the FOS.

Manzari and Nour [17] applied a third method for assessing slope stability. This method is based on load increments instead of reducing the strength parameters of the soil. The unit weight of the soil is incremented till excessive displacements are detected in a part of the slope that is sliding with respect to the stable part of the slope. The stability of the slope is then assessed with a critical stability number (CSN), which is similar to a FOS.

Diana FEA is developing a new method for analysing slope stability. This new method is based on the extended finite element method (XFEM). XFEM is a mesh independent method for modeling discontinuities. Unique with respect to the aforementioned slope stability analysis methods is that this method detects onset of localisation and computes the propagation of the slip surface. Hence, this XFEM-based analysis method will in this work be referred to as the propagation method (PM).

The numerical procedure of the PM can be divided into three main steps. The first step is detecting onset of localisation. The requirement for onset of localisation is that the determinant of a so called acoustic tensor must be zero. Leroy and Ortiz [29] described a numerical algorithm for detecting onset of localisation for associative plasticity models. Sanborn and Prévost [26] expanded this to a more general algorithm for non-associative plasticity. Onset of localisation is detected in the integration points of the finite elements, since onset of localisation is dependent on the stress state. Rudnicki and Rice [13] derived analytical solutions for onset of localisation for a Drucker-Prager material model for 2D cases. Ottoson and Runesson [18] concluded that the solutions of Rudnicki and Rice are a special case of a more general solution. They derived solutions for 3D cases and other material models, such as Mohr-Coulomb and Rankine. Runesson *et al.* [14] provide solutions for explicitly plane strain and plane stress models. The analytical solutions of these papers are derived from the same requirement for onset of localisation. With these solutions it can be determined whether onset of localisation occurs for a given stress state in an arbitrary point. Also the direction normal to the plane of localisation is obtained in this point.

The second step is to implement enrichment elements at the location of localisation. These enrichment elements can reproduce a jump in the displacement field. Therefore, these elements represent a part of the slip surface. In the last step, a search algorithm captures the progression of localisation till the slip surface is fully developed. Global failure of the slope occurs when the slip surface is fully developed.

These steps were implemented by Sanborn and Prévost [26], who combined the detection of onset of localisation with XFEM such that the progression of a slip surface can be captured. Liu [20] proposed a linear cohesive/friction coupled model for the frictional contact interface based on the Mohr-Coulomb frictional law. Wang *et al.* [28] computed the propagation mode and propagation direction by the stress state of specific propagation-control areas.

The steps of the PM need to be tested and verified, since the method is being developed for the software of Diana FEA. The objective of this work is to verify onset of localisation and to provide a method for verification of the point of global failure in an analysis with the PM.

1.2. Thesis objective

The objective of this work is to verify onset of localisation and to provide a method for verification of the point of global failure in analyses with the PM. To be able to accomplish these objectives, the following questions have to be answered

- *How to verify a numerical computation of onset of localisation?*
- *How to verify the point of global failure in an analysis with the PM?*

Onset of localisation can be verified with the analytical solutions from Rudnicki and Rice [13] and Runesson *et al.* [14] and with the numerical results of Leroy and Ortiz [29].

An answer to the second question is to verify the point of global failure with use of the FOS of other analysis methods, since the FOS gives an indication of the global stability of a slope. The other analysis methods are the SSM and the SRM. However, the current research about the PM [26], [20], [28] does not provide a method for computing the FOS with the PM. Now the following question arises

- *How to compute a FOS with the PM which can be compared with the FOS of the SSM and the SRM?*

The PM is based on incremental loading of the weight, while the SSM and the SRM are based on the strength parameters of the soil and not on load increments. Manzari and Nour [17] analyse the stability of a slope by incrementing the unit weight till failure of the slope occurs. Then the CSN is obtained. Since this method is also based on load increments, it is perfectly suitable for computing a CSN with the PM. The problem left is to find a relation between the CSN and the FOS, such that the point of global failure in an analysis with the PM can be verified with the SSM and the SRM. Hence, the last question to be answered in order to achieve the thesis objectives is

- *What is the relation between the CSN and the FOS?*

The objectives of the thesis are summarised below

- Verification of onset of localisation on elements level with analytical expressions and numerical results. This means that onset of localisation must occur for the correct stress state and the correct localisation direction must be obtained.
- Finding a relation between the CSN and the FOS.
- Obtaining reliable benchmarks with numerical slope stability analysis methods, which can be used for verification of the point of global failure of a slope in analyses with the PM.
- Testing a development version of the PM on a FE-model of a slope.

1.3. Scope of the thesis

- The benchmarks are generated for linear and quadratic 2D FE-elements.
- Two FE-models of a slope are used for the parameter study and the convergence study. These models are based on the models of Griffiths and Lane [9] and Manzari and Nour [17] and the results of these papers serve as a reference.
- In the parameter studies, the effect of the Poisson ratio and the dilatancy angle on the FOS and CSN is studied respectively.
- The convergence studies are performed with mesh sizes of 0.25m, 0.5m, 1m and 2m.
- The results of the studies are only valid for the FE-models used in this work. Therefore, the exact same models should be used, when verifying the PM with the benchmarks of this thesis.
- Only plane strain elements are used, which is common for modeling soil. The elements obey a Mohr-Coulomb plasticity law if the model contains non-linear material behaviour. The interfaces, modeled with interface elements or with enrichment elements obey a Mohr-Coulomb friction law.
- The soil is homogeneous.
- The load on the soil elements are uniformly distributed.
- Onset of localisation is verified on element level. Plane strain elements obeying Drucker-Prager yield criteria are used for the verification of onset of localisation.
- The behaviour of the enrichment elements is verified with the results of the FE-model with interface elements.
- The derivations and analyses are based on small strains and displacements.

1.4. Derivation of initiation conditions of localisation

This section gives a mathematical derivation of onset of localisation, since the initiation condition of localisation is an important aspect of the PM method. Tensor notation is used for the derivation.

Localisation is the process where a smooth displacement field suddenly gives rise to large strains, localised in narrow bands [26]. This is an important failure mechanism of ground slopes. Onset of localisation is the beginning of this failure mechanism. The onset of localisation coincides with the loss of ellipticity of the governing equilibrium equations, which means that suddenly discontinuities in the solution are possible [5]. The conditions for onset of localisation can be derived for strong discontinuities and for weak discontinuities. A weak discontinuity is a jump in the gradient of the solution field (C^0 continuity). This jump is across a point in 1D, a line in 2D, or a surface in 3D which from now on will be named the interface. A strong discontinuity is a discontinuity in the solution field itself across an interface [11] (C^{-1} continuity). Requirements for onset of localisation are derived for both weak and strong discontinuities to show the differences and similarities between these conditions.

At local level a material is stable when the product of the the strain rate $\dot{\boldsymbol{\epsilon}}$ and stress rate $\dot{\boldsymbol{\sigma}}$ is positive [21]

$$\dot{\boldsymbol{\epsilon}} : \dot{\boldsymbol{\sigma}} > 0 \tag{1.1}$$

Equation 1.1 holds for geometrical linear models. The relation between the strain and stress tensor can be written as

$$\dot{\boldsymbol{\sigma}} = \boldsymbol{D} : \dot{\boldsymbol{\epsilon}} \tag{1.2}$$

with $\boldsymbol{D}$ the material tangential stiffness matrix. Substitution in equation 1.1 gives

$$\dot{\boldsymbol{\epsilon}} : \boldsymbol{D} : \dot{\boldsymbol{\epsilon}} > 0 \tag{1.3}$$

When the unequal sign becomes an equal sign, material stability is lost. This is called loss of positive definiteness and happens when the determinant of the material tangential stiffness matrix becomes zero.

$$\det(\boldsymbol{D}) = 0 \tag{1.4}$$

An example of loss of material stability is when the slope of the stress-strain curve becomes negative during an uniaxial compression or tension test. This is called strain softening. However, there are materials for which the scalar value of equation 1.1 may become negative without the occurrence of strain softening [6]. This holds for soils and rocks. Constitutive relations of these materials often result in non-symmetric tangential stiffness matrices. The non-symmetry may lead to unstable material behaviour, even in the hardening regime [13]. When equation 1.1 is violated, nothing in general can be said about the continuity of the solution. When positive definiteness is lost, it can result in loss of ellipticity of the governing equations. This means in mathematical terms that discontinuities in the solution are possible [5]. So material instability is not equal to loss of ellipticity, which is the point of interest. Hence, the question is when ellipticity is lost and discontinuities in the solution are possible.

For the derivation of loss of ellipticity the following assumptions are made

- small deformations
- at current state of equilibrium the displacements u_i, stresses σ_{ij} and strains ϵ_{ij} are continuous
- no thermal effects are taken into account
- rate independent elasto-plastic solids are considered
- quasi-static loading conditions

The following derivations are based on the work from [5], [11], [14], [18], [22], [26], [29]. For elasto-plastic solids the definition of the tangential material stiffness matrix is given by

$$\boldsymbol{D} = \begin{cases} \boldsymbol{D}^e & \text{(E)} \\ \boldsymbol{D}^e - \dfrac{1}{A}\boldsymbol{D}^e : \boldsymbol{g} \otimes \boldsymbol{f} : \boldsymbol{D}^e & \text{(P)} \end{cases} \tag{1.5}$$

where (E) and (P) stands for elastic and plastic loading respectively. $\boldsymbol{D}^e$ is the elastic tangential stiffness matrix which is assumed constant and symmetric, while it may represent isotropic as well as anisotropic behavior. The tensors $\boldsymbol{f}$ and $\boldsymbol{g}$ are given by

$$\boldsymbol{f} = \frac{\partial F}{\partial \boldsymbol{\sigma}}, \qquad \boldsymbol{g} = \frac{\partial G}{\partial \boldsymbol{\sigma}} \tag{1.6}$$

Where F and G are the yield function and the plastic potential respectively. If $F = G$, the plastic flow is associated and when $F \neq G$ the plastic flow is non-associated. The yield function F is a function of stress and an internal variable κ. $\partial_{\boldsymbol{\sigma}} F$ is the outer normal to the yield surface and $\partial_{\boldsymbol{\sigma}} G$ is the direction of the plastic flow. The positive parameter A is defined as

$$A = H + \boldsymbol{f} : \boldsymbol{D}^e : \boldsymbol{g} > 0 \tag{1.7}$$

with H the plastic modulus, which is positive, zero or negative for hardening, perfect or softening plasticity respectively. Plastic yielding will take place whenever the following conditions are satisfied

$$F(\boldsymbol{\sigma}, \kappa) = 0 \quad \text{and} \quad \dot{F}(\boldsymbol{\sigma}, \kappa) = \frac{\partial F}{\partial \boldsymbol{\sigma}} : \dot{\boldsymbol{\sigma}} + \frac{\partial F}{\partial \kappa}\dot{\kappa} = 0 \tag{1.8}$$

The condition $\dot{F} = 0$ is Prager's consistency condition. Now consider that within a body a (possible curved) plane S emerges (see Figure 1.1). If this band has a finite width across which the velocity field $\dot{\boldsymbol{u}}$ is continuous, but the gradient of the velocity field $\nabla\dot{\boldsymbol{u}}$ is not, it is called a weak discontinuity. If the width of the band is taken to zero in the limit, the velocity field becomes discontinuous also. This is called a strong discontinuity. First localisation in the form of a weak discontinuity is considered. As stated before, a jump in the gradient of the velocity is assumed to exist.

$$[\![\nabla\dot{\boldsymbol{u}}]\!] = \nabla\dot{\boldsymbol{u}}^+ - \nabla\dot{\boldsymbol{u}}^- \neq 0 \tag{1.9}$$

It is assumed that the jump in the velocity field $[\![\dot{\boldsymbol{u}}]\!]$ along the surface S is constant. Now let the position vector along S be denoted as $\boldsymbol{x}$, then the following holds

$$\mathrm{d}[\![\dot{\boldsymbol{u}}]\!] = [\![\nabla\dot{\boldsymbol{u}}]\!]\mathrm{d}\boldsymbol{x} = 0 \tag{1.10}$$

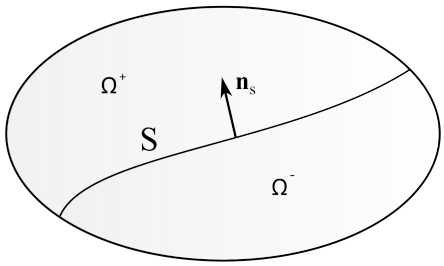

Figure 1.1: A body with a discontinuity, S, and a continuous displacement field at each side of the discontinuity.

where d$\boldsymbol{x}$ is an arbitrary differential vector tangential to S. The general solution to equation 1.11 is [18] [26]

$$[\![\nabla \dot{\boldsymbol{u}}]\!] = \dot{\boldsymbol{g}} \otimes \boldsymbol{n}_S \tag{1.11}$$

with $\boldsymbol{n}_S$ the normal to the discontinuity surface S. The jump in the strain rate follows as

$$[\![\dot{\boldsymbol{\epsilon}}]\!] = \frac{1}{2}\left(\dot{\boldsymbol{g}} \otimes \boldsymbol{n}_S + \boldsymbol{n}_S \otimes \dot{\boldsymbol{g}}\right) \tag{1.12}$$

where g could be interpreted as the relative displacement of points at + side of the discontinuity with respect to points at the − side of the discontinuity [29]. Equilibrium across the surface requires that the traction must be continuous. This means that the jump in the traction is zero.

$$[\![\dot{\boldsymbol{t}}]\!] = \boldsymbol{n}_S \cdot [\![\dot{\boldsymbol{\sigma}}]\!] = 0 \tag{1.13}$$

There are two types of bifurcations possible. Both sides of the surface S can respond plastically (plastic/plastic bifurcation) or one side responds elastically while the other side responds plastically (elastic/plastic bifurcation). Plastic/plastic bifurcation always occurs before elastic/plastic bifurcation [18]. Hence, only plastic/plastic bifurcation is considered. This means that the material tangential stiffness matrix $\boldsymbol{D}$ takes the same value at both sides of the surface S. Substitution of equation 1.2 and 1.12 in equation 1.13 gives

$$\boldsymbol{n}_S \cdot \boldsymbol{D} : (\dot{\boldsymbol{g}} \otimes \boldsymbol{n}_S) = 0 \tag{1.14}$$

where the symmetry property of $\boldsymbol{D}$ is used. For a weak discontinuity to occur, equation 1.14 must be satisfied. A non-trivial solution is only possible when the determinant of the elasto-plastic acoustic tensor $\boldsymbol{A} = \boldsymbol{n}_S \cdot \boldsymbol{D} \cdot \boldsymbol{n}_S$ vanishes.

$$\det(\boldsymbol{n}_S \cdot \boldsymbol{D} \cdot \boldsymbol{n}_S) = \det(\boldsymbol{A}) = 0 \tag{1.15}$$

Thus, when equation 1.15 is satisfied, discontinuities in the gradient of the velocity field can emerge. For strong discontinuities a jump in the displacement field $\boldsymbol{u}$ is possible. This can be represented as

$$\boldsymbol{u} = \bar{\boldsymbol{u}} + H_S(\boldsymbol{x})\,[\![\boldsymbol{u}]\!] \tag{1.16}$$

with $H_S(\boldsymbol{x})$ the Heaviside function at the discontinuity. Differentiation of equation 1.16 gives the strain field as

$$\boldsymbol{\epsilon} = \bar{\boldsymbol{\epsilon}} + H_S(\boldsymbol{x})\,\nabla^{\text{sym}}[\![\boldsymbol{u}]\!] + \delta_S([\![\boldsymbol{u}]\!] \otimes \boldsymbol{n}_S)^{\text{sym}} \tag{1.17}$$

with ∇^{sym} the symmetric gradient operator, $\nabla^{\text{sym}}(\cdot) = \frac{1}{2}(\nabla\otimes(\cdot) + (\cdot)\otimes\nabla)$, $(\cdot)^{\text{sym}}$ the symmetric operator, $(\cdot)^{\text{sym}} = \frac{1}{2}((\cdot) + (\cdot)^T)$, δ the Dirac delta function and $\bar{\boldsymbol{\epsilon}}$ is $\nabla^{\text{sym}}\bar{\boldsymbol{u}}$. Differentiating equation 1.17 with respect to time gives the strain rate field as

$$\dot{\boldsymbol{\epsilon}} = \dot{\bar{\boldsymbol{\epsilon}}} + H_S(\boldsymbol{x})\,\nabla^{\text{sym}}[\![\dot{\boldsymbol{u}}]\!] + \delta_S([\![\dot{\boldsymbol{u}}]\!] \otimes \boldsymbol{n}_S)^{\text{sym}} \tag{1.18}$$

The gradient of the displacement rate jump is much smaller than the jump in the velocity field due to the assumption of infinitesimal displacements. Therefore, the second term in equation 1.18 can be neglected and the strain rate can be written as

$$\dot{\boldsymbol{\epsilon}} = \dot{\tilde{\boldsymbol{\epsilon}}} + \delta_S([\![\dot{\boldsymbol{u}}]\!] \otimes \boldsymbol{n}_S)^{\text{sym}} \tag{1.19}$$

In elasto-plastic material models, the total strain is expressed as a sum of the elastic strain and the plastic strain as $\boldsymbol{\epsilon} = \boldsymbol{\epsilon}^e + \boldsymbol{\epsilon}^p$. Rewriting this as $\boldsymbol{\epsilon}^e = \boldsymbol{\epsilon} - \boldsymbol{\epsilon}^p$ and substitution of this expression in equation 1.2 together with equation 1.19 gives

$$\dot{\boldsymbol{\sigma}} = \boldsymbol{D}^e : \left(\dot{\tilde{\boldsymbol{\epsilon}}} + \delta_S([\![\dot{\boldsymbol{u}}]\!] \otimes \boldsymbol{n}_S)^{\text{sym}} - \dot{\lambda} \frac{\partial G}{\partial \boldsymbol{\sigma}} \right) \tag{1.20}$$

where $\dot{\lambda}\partial G/\partial\boldsymbol{\sigma}$ is $\dot{\boldsymbol{\epsilon}}^p$, with $\dot{\lambda}$ the plastic consistency parameter, which determines the magnitude of the plastic flow. The traction rate can be written as

$$\dot{\boldsymbol{t}} = \dot{\boldsymbol{\sigma}} \cdot \boldsymbol{n}_S = \boldsymbol{D}^e : \left(\dot{\tilde{\boldsymbol{\epsilon}}} + \underbrace{\delta_S([\![\dot{\boldsymbol{u}}]\!] \otimes \boldsymbol{n}_S)^{\text{sym}}}_{\text{unbounded}} - \dot{\lambda} \frac{\partial G}{\partial \boldsymbol{\sigma}} \right) \cdot \boldsymbol{n}_S \tag{1.21}$$

As stated before, the jump in the traction across the surface S must be zero. For this to be true, the unbounded term in equation 1.21 must be canceled out by the plastic strain [26]. This implies that the plastic parameter must be in the form of $\dot{\lambda} = \dot{\lambda}_\delta \delta_S$ [11]. To be able to solve for the positive number $\dot{\lambda}_\delta$, the consistency condition from equation 1.8 is used. Substitution of the unbounded form of the plastic parameter in the stress rate of equation 1.20 and substituting equation 1.20 in the consistency condition gives

$$\dot{F}(\boldsymbol{\sigma}, \kappa) = \frac{\partial F}{\partial \boldsymbol{\sigma}} : \boldsymbol{D}^e : \left(\dot{\tilde{\boldsymbol{\epsilon}}} + \delta_S([\![\dot{\boldsymbol{u}}]\!] \otimes \boldsymbol{n}_S)^{\text{sym}} - \dot{\lambda}_\delta \delta_S \frac{\partial G}{\partial \boldsymbol{\sigma}} \right) + \frac{\partial F}{\partial \kappa} \dot{\kappa} = 0 \tag{1.22}$$

For the consistency condition in equation 1.22 to be satisfied, the bounded terms must sum to zero as well as the unbounded terms [11]. This gives the following two equations

$$\begin{aligned} \frac{\partial F}{\partial \boldsymbol{\sigma}} : \boldsymbol{D}^e : \dot{\tilde{\boldsymbol{\epsilon}}} + \frac{\partial F}{\partial \kappa} \dot{\kappa} = 0 \\ \frac{\partial F}{\partial \boldsymbol{\sigma}} : \boldsymbol{D}^e : \delta_S([\![\dot{\boldsymbol{u}}]\!] \otimes \boldsymbol{n}_S)^{\text{sym}} - \frac{\partial F}{\partial \boldsymbol{\sigma}} : \boldsymbol{D}^e : \dot{\lambda}_\delta \delta_S \frac{\partial G}{\partial \boldsymbol{\sigma}} = 0 \end{aligned} \tag{1.23}$$

From the second equation in 1.23 and using equation 1.6, $\dot{\lambda}_\delta$ can be determined as

$$\dot{\lambda}_\delta = \frac{\boldsymbol{f} : \boldsymbol{D}^e : ([\![\dot{\boldsymbol{u}}]\!] \otimes \boldsymbol{n}_S)^{\text{sym}}}{\boldsymbol{f} : \boldsymbol{D}^e : \boldsymbol{g}} \tag{1.24}$$

Substituting equation 1.24 with $\dot{\lambda} = \dot{\lambda}_\delta \delta_S$ in equation 1.21 and using again that the jump in the traction rate $[\![\dot{\boldsymbol{t}}]\!]$ is equal to zero leads to

$$[\![\dot{\boldsymbol{t}}]\!] = \boldsymbol{D}^e : \left(([\![\dot{\boldsymbol{u}}]\!] \otimes \boldsymbol{n}_S)^{\text{sym}} - \frac{\boldsymbol{f} : \boldsymbol{D}^e : ([\![\dot{\boldsymbol{u}}]\!] \otimes \boldsymbol{n}_S)^{\text{sym}}}{\boldsymbol{f} : \boldsymbol{D}^e : \boldsymbol{g}} \boldsymbol{g} \right) \cdot \boldsymbol{n}_S = 0 \tag{1.25}$$

It can be noted that only the unbounded terms are left, since the continuous part cancels out. Rewriting equation 1.25 leads to

$$\begin{aligned} [\![\dot{\boldsymbol{t}}]\!] &= \boldsymbol{D}^e : \left(([\![\dot{\boldsymbol{u}}]\!] \otimes \boldsymbol{n}_S)^{\text{sym}} - \frac{\boldsymbol{f} : \boldsymbol{D}^e : ([\![\dot{\boldsymbol{u}}]\!] \otimes \boldsymbol{n}_S)^{\text{sym}}}{\boldsymbol{f} : \boldsymbol{D}^e : \boldsymbol{g}} \boldsymbol{g} \right) \cdot \boldsymbol{n}_S = 0 \\ &= \boldsymbol{D}^e : \left(\boldsymbol{I} - \boldsymbol{g} \otimes \frac{\boldsymbol{f} : \boldsymbol{D}^e}{\boldsymbol{f} : \boldsymbol{D}^e : \boldsymbol{g}} \right) : ([\![\dot{\boldsymbol{u}}]\!] \otimes \boldsymbol{n}_S)^{\text{sym}} \cdot \boldsymbol{n}_S = 0 \\ &= \left(\boldsymbol{D}^e - \frac{\boldsymbol{D}^e : \boldsymbol{g} \otimes \boldsymbol{f} : \boldsymbol{D}^e}{\boldsymbol{f} : \boldsymbol{D}^e : \boldsymbol{g}} \right) : ([\![\dot{\boldsymbol{u}}]\!] \otimes \boldsymbol{n}_S)^{\text{sym}} \cdot \boldsymbol{n}_S = 0 \\ &= \boldsymbol{n}_S \cdot \left(\boldsymbol{D}^e - \frac{\boldsymbol{D}^e : \boldsymbol{g} \otimes \boldsymbol{f} : \boldsymbol{D}^e}{\boldsymbol{f} : \boldsymbol{D}^e : \boldsymbol{g}} \right) \cdot \boldsymbol{n}_S \cdot [\![\dot{\boldsymbol{u}}]\!] = 0 \end{aligned} \tag{1.26}$$

With $\boldsymbol{I}$ the fourth-order identity tensor. Now lets define the elastic-perfect plastic tangent stiffness matrix as

$$\boldsymbol{D}^{\text{epp}} = \boldsymbol{D}^{e} - \frac{\boldsymbol{D}^{e} : \boldsymbol{g} \otimes \boldsymbol{f} : \boldsymbol{D}^{e}}{\boldsymbol{f} : \boldsymbol{D}^{e} : \boldsymbol{g}} \tag{1.27}$$

The last equation in 1.26 is a result of minor symmetries in $\boldsymbol{D}^{\text{epp}}$ [26]. A non-trivial solution is only possible when the determinant of the elastic-perfect plastic acoustic tensor $\boldsymbol{A}^{\text{epp}} = \boldsymbol{n}_S \cdot \boldsymbol{D}^{\text{epp}} \cdot \boldsymbol{n}_S$ is zero.

$$\det(\boldsymbol{n}_S \cdot \boldsymbol{D}^{\text{epp}} \cdot \boldsymbol{n}_S) = \det(\boldsymbol{A}^{\text{epp}}) = 0 \tag{1.28}$$

Equation 1.28 is the initiation condition for localisation of strong discontinuities. This condition is almost the same as the initiation condition for weak discontinuities in equation 1.15. The difference is between the elasto-plastic and elastic-perfect plastic tensor $\boldsymbol{D}$ and $\boldsymbol{D}^{\text{epp}}$. The tensor $\boldsymbol{D}$ contains the plastic modulus H, while the $\boldsymbol{D}^{\text{epp}}$ tensor does not. For perfect plasticity the plastic modulus H is zero. This is why $\boldsymbol{D}^{\text{epp}}$ is called the elastic-perfect plastic tensor. Hence, for perfect plasticity the conditions in equation 1.15 and 1.28 become the same.

The material tangential stiffness matrix of the model is described in equation 1.5, which is a function of the plastic modulus H. This means that even though the condition in equation 1.28 does not contain the plastic modulus H, it still depends on the stress state, which is dependent on H [26]. The determinants of the acoustic tensors $\boldsymbol{A}$ and $\boldsymbol{A}^{\text{epp}}$ approach zero from the positive side [29] [14], which will be shown in Chapter 6.1. Also, in general the plastic modulus H initially has a (large) positive value and decreases during loading. The value of H for which the determinant of the acoustic tensor becomes zero is called the critical plastic modulus H^{cr}. For non-associated plasticity the, critical plastic modulus may be larger than zero [13]. This means that even in the hardening regime, onset of localisation can take place. The critical plastic modulus is less than or equal to zero for associated plasticity [13]. If localisation takes place in the hardening regime, a strong discontinuity will precede a weak discontinuity. Conversely, if localisation takes place in the softening regime, a weak discontinuity precedes a strong discontinuity [25].

1.5. Analysis methods

This section gives a concise description of all the analysis methods used in this work. Besides the PM, two methods were mentioned explicitly. The strength reduction method (SRM) and the slip surface method (SSM), which are two built-in methods in Diana FEA. The FE-models used in this thesis are based on models from the work of Griffiths and Lane [9] and Manzari and Nour [17] and the results of those works are used as reference. The methods for assessing slope stability used in these papers differ from the SSM and the SRM. Hence, the methods used in these works are also applied for generation of the benchmarks.

A strength reduction analysis is based on the reduction of the cohesion and the friction angle, which are the strength parameters of the soil. With these two parameters the Mohr-Coulomb envelope can be described (see Figure 1.2). In the SRM of Diana FEA, this reduction is done automatically in an iterative procedure. Griffiths and Lane used [9] a SRM, which is closely related to the SRM of Diana FEA. They applied a single step gravity turn on and the strength parameters are reduced by a factor if the model does converge within a certain amount of equilibrium iterations. The factor used for reducing the strength parameters is called the strength reduction factor (SRF). Then the analysis is run again for the same load. This procedure is repeated till the model does not converge within the user specified amount of iterations. Griffiths and Lane [9] state that global failure of the slope occurs if this non-convergence occurs. At this point, the FOS can be computed, which takes the value of the SRF at this point. This type of analysis is called the manual strength reduction method (MSRM) in this work.

Another method is the SSM, which is a post-processing method. This is a post-processing method because the FOS is computed from the stress state after convergence is reached in a FE-analysis. The FOS is computed from various slip surfaces, by integrating the shear stresses along the slip surfaces. The critical slip surface is the one which attains the smallest FOS.

Manzari and Nour [17] used a different approach for assessing the stability of a slope. Instead of reducing the strength parameters, the unit weight is increased till failure of the slope occurs. Therefore, this method lends itself perfectly for verification of the PM, since the load is also incremented in the PM. When failure occurs the CSN is computed, which is similar to a FOS. In the work of Manzari and Nour it is not mentioned what load increments are used. Therefore, the choice is made to perform analyses with incremental loading and with a single step gravity turn on. The former provides a method for computing the CSN with a single analysis and therefore directly applicable to the PM. The latter is analogous to the single gravity turn on method used by Griffiths and Lane [9]. By utilising both methods, it will be clear whether or not there will be a (big) difference in the CSN due to those loading methods. An analysis applied with incremental loading is called the multiple load increment

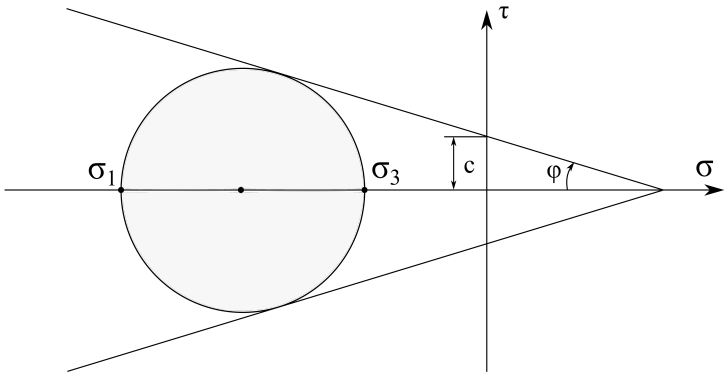

Figure 1.2: Mohr's stress circle of an arbitrary stress state and the envelopes that bound the possible stress states, characterized by the internal friction angle, φ, and the cohesion, c. Local failure occurs if the stress state of a point is outside the shear envelope.

method (MLIM) and an analysis performed with a single step gravity turn on is called the single load increment method (SLIM).

As mentioned before, the new method for assessing slope stability which is being developed in Diana FEA, is called the propagation method (PM). The propagation method can be described with the following procedures. First, onset of localisation is detected in elasto-plastic finite elements. Next, enrichment elements are inserted at the location of the instabilities. These elements can exhibit a jump in the displacement field. Then this discontinuous behaviour is governed by a Mohr-Coulomb friction law. Progression of this discontinuity results in a (critical) slip surface. To detect onset of localisation and to capture the progression of this slip surface makes this third method unique with respect to the other two methods. The procedure is described in more detail in Chapter 2.5.

In this work a development version of the PM is tested on a FE-model of a slope. The development version is restricted to a predefined slip surface in the FE-model, modeled by enrichment elements. The objective is to verify the behaviour of the enrichment elements in this FE-model. The enrichment elements are able to reproduce a jump in the displacement field according to a Mohr-Coulomb friction law. Hence, the best way for verification of the enrichment elements is to compare the results of this development version with the results of a model with interface elements. The results should be approximately the same, since the interface elements are also able to reproduce a jump in the displacement field according to a Mohr-Coulomb friction law. The models with interface elements and enrichment elements are analysed with load increment methods in order to obtain a CSN. An overview of the methods for assessing slope stability and its abbreviations is given in Table 1.1.

	Strength reduction		Load increments		
Method	SRM	MSRM	MLIM	SLIM	SSM
Variables	φ, c	φ, c	γ	γ	$\boldsymbol{\sigma}$
Result	FOS	FOS	CSN	CSN	FOS

Table 1.1: Table with all analysis methods for assessing slope stability used in the thesis. There are the strength reduction methods based on reduction of the friction angle φ and/or the cohesion c and there are the methods based on the increment of the unit weight γ. The SSM is based on post-processing the stresses.

1.6. Solution procedure

In Section 1.2 four main objectives were given. These objectives are shown in the top of the diagram of Figure 1.3. This diagram gives an overview of the solution procedures used for achieving the objectives, the corresponding FE-models, the analysis methods used on those FE-models and the (expected) results. The objectives and the solutions procedures are explained in the following.

The first objective is to find a relation between the FOS and the CSN. Through this relation, a FOS can be

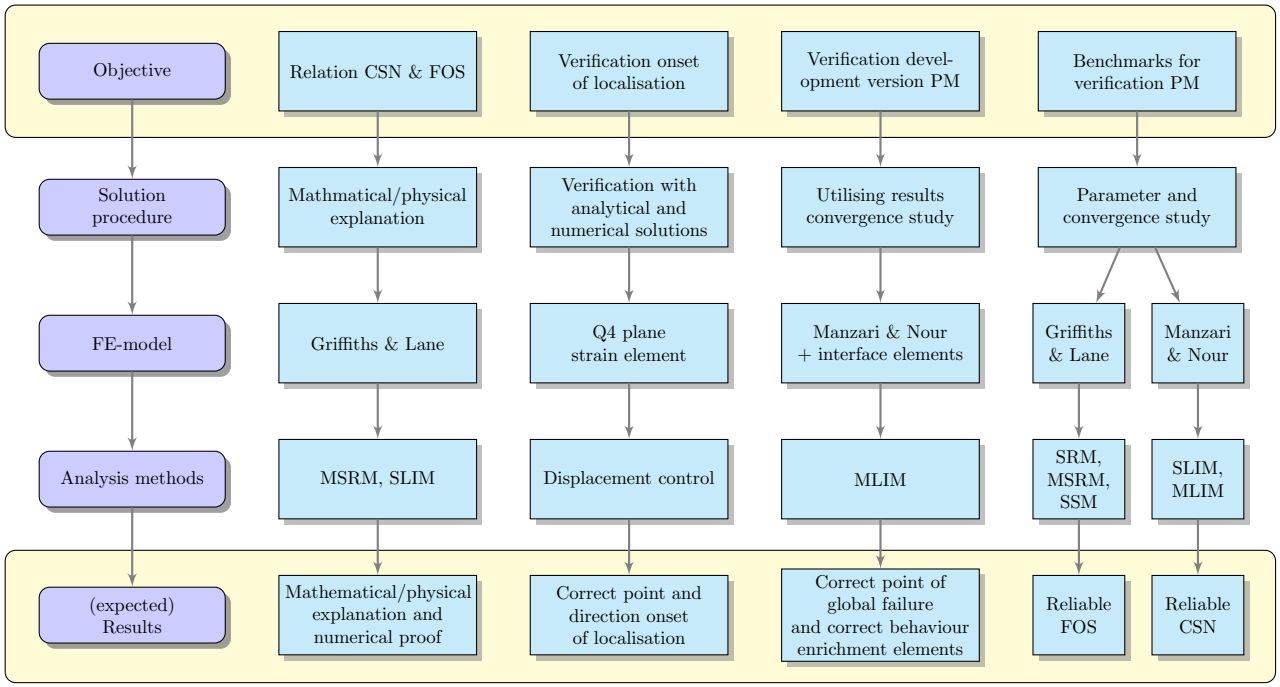

Figure 1.3: Overview of procedure steps of the thesis from the four main objectives to the (expected) results.

computed with the PM which is similar to the FOS of a SSM and a SRM. Then, the FOS of the SSM and the SRM can be used as a benchmark for verification of the PM. A mathematical relation is made through the definitions of the FOS [1] and the CSN and the relation can be physically interpreted by the Mohr-Coulomb shear envelope. Numerical proof is given by results of MSRM and SLIM analyses of the FE-model of Griffiths and Lane [9].

The next objective in the diagram is verification of onset of localisation in a FE-analysis on element level. To verify onset of localisation, the determinant of the acoustic tensor is monitored during a numerical analysis of a plane-strain element. The element is loaded by displacement-control in order to capture plastic behaviour. Onset of localisation must occur for the correct stress state and the right angle of the vector normal to the localisation plane must be obtained. This is verified by numerical results and analytical expressions.

A third objective is to verify a development version of the PM. Here, the behaviour of the enrichment elements have to be tested in a FE-model of a slope. The model of Manzari and Nour [17] is used for this verification. Interface elements are applied, which behave similar to enrichment elements. The interface elements model a pre-defined slip surface. A convergence study of this model should result in a reliable CSN, which can be used as benchmark for verification of the FE-model containing enrichment elements. In the convergence study, a reliable CSN should be obtained by reducing the mesh size in the analyses. The CSN of the model with enrichment elements should be very close to this benchmark. If this is true, the point of global failure is computed correctly in the analysis with the development version of the PM for the corresponding FE-model. More information for conclusions about the correct behaviour of the enrichment elements is provided by the kinematics and the values of the stresses of the enrichment elements.

The last objective is to generate benchmarks, which can be used for the verification of the PM. A convergence and parameter study will be applied on the FE-models of Griffiths and Lane [9] and Manzari and Nour [17]. The convergence study should result in reliable FOSs and the parameter studies will provide information which can be used for for verification of the PM.

1.7. Thesis outline

Chapter 2 describes more extensively the different analysis methods for assessing slope stability and the definitions of the FOS and the CSN. In chapter 3 it is explained how the analysis methods are applied for creating the benchmarks. In the end of Chapter 3 a relation is established between methods based on strength reduction and methods based on load increments. Analogous to this, a method is provided for computing the FOS with the PM

[1] The definition of the FOS of the SRM.

method.

The benchmarks generated with methods based on strength reduction and the SSM are given in Chapter 4. The benchmarks are obtained through a convergence study of the FOS and by a study of the effect of the Poisson ratio on the FOS. Chapter 5 gives the benchmarks, obtained with the analyses based on load increments, of a model with and without interface elements. This chapter provides convergence studies and a study of the effect of the dilatancy angle on the CSN.

Next, the verification of onset of localisation is given in chapter 6. Onset of localisation is verified with numerical and analytical results. Then, the results of an analysis of a slope with a development version of the PM method are presented and compared with the results of a model with interface elements.

Finally, Chapter 7 gives the conclusions and recommendations of the thesis.

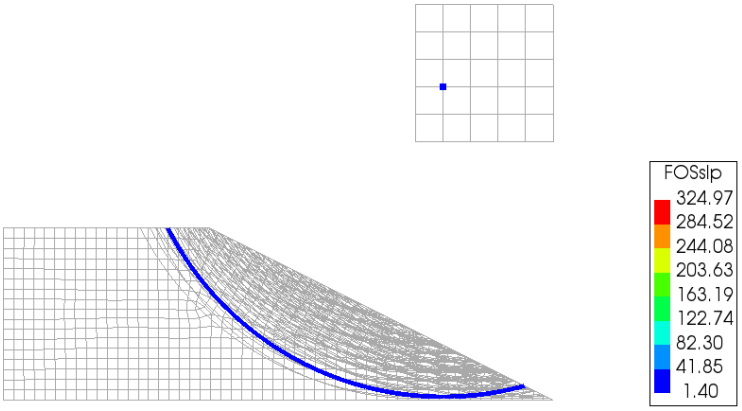

Figure 2.1: FE-model analysed with the slip surface method. The critical slip surface with a corresponding FOS of 1.4 is indicated by the blue line. The center of the circle is indicated by the blue dot in the grid above the slope.

2

Analysis methods

2.1. The slip surface method

With the slip surface method a FOS is computed from the effective stresses in the model. This means that the FOS is computed during the post-processing. The slip surface method works as follows. First a grid is drawn above the soil in the FE-model, as shown in Figure 2.1. Various slip surface circles are generated from the grid points and the intersections with the plane strain soil elements are computed. The slip surface circles are divided in 2-node line elements if the soil is modeled with quadrilateral (Q4) or triangular (T3) elements. The circles are divided in 3-node elements if the soil elements are modeled with higher order elements. These line elements contain integration points, which is shown in Figure 2.2. The stresses are computed in the integration points of the soil elements and are extrapolated to the nodes of the element. Next, the stresses are interpolated in the integration points of the line elements. The stresses in these integration points are transformed such that the stress

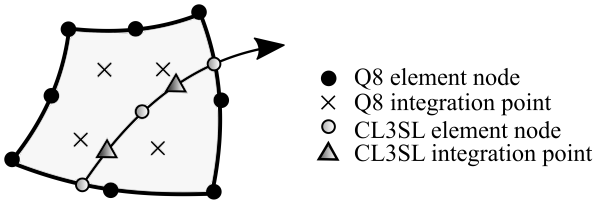

Figure 2.2: Q8-element intersecting with a 3-node slip surface line element (CL3SL). The reduced amount of Gauss points of the Q8 element are only shown for clarification.

components are normal and tangential to the line elements. The FOS can now be computed from the obtained shear stresses with the following integral

$$\text{FOS} = \frac{1}{l}\int \frac{\tau_{\text{MC}}}{\tau} d\xi \tag{2.1}$$

where l is the length of the slip surface, τ is the shear stress in the slip surface and τ_{MC} is the Mohr-Coulomb critical shear stress, defined as

$$\tau_{\text{MC}} = c + \sigma_n \tan(\varphi) \tag{2.2}$$

with c the cohesion, φ the internal friction angle and σ_n the normal stress. The envelope of Figure 1.2 gives a geometrical interpretation of possible values of the maximum Mohr-Coulomb shear stress. The FOS of equation 2.1 is a summation over the shear stresses in the integration points of the line elements, due to the discretization.

$$\text{FOS} = \frac{1}{l_T}\sum_{i=1}^{n} \frac{\tau_{\text{MCi}}}{\tau_i} \tag{2.3}$$

Where l_T the total length of the slip surface elements and i the integration points of the slip surface elements. Equation 2.1 and 2.3 can be interpreted as an average normalised shear stress. The slip surface is stable if the FOS is equal or larger than 1 and unstable if the FOS is smaller than 1. It may be noted that the reduction of the cohesion and the friction angle during the SRM is based on the Mohr-Coulomb shear strength envelope of equation 2.2 [24]. An advantage of the slip surface method is that it gives a good approximation of the FOS of the slope in its current stress state. However, the method provides no information about the progression of the slip surface. The slip surface method is also only applied for circular slip surfaces.

2.2. The strength reduction method and the manual strength reduction method

An analysis with the SRM consist of two phases. In phase one, the current stress state of a soil can be simulated by a standard non-linear analysis using load increments. The resulting stress state is used as a (initial) loading condition of the soil in phase 2. In phase 2, the values of the friction angle φ and/or the cohesion c are reduced iteratively by a factor, which is the FOS (this is not the final FOS). First, an initial FOS is set, which is 1 by default. Then the analysis is run until equilibrium is computed, followed by a reduction of the strength parameters φ and c according to

$$\begin{aligned} c_{\text{n+1}} &= \frac{c}{\text{FOS}_{\text{n+1}}} \\ \tan(\varphi_{\text{n+1}}) &= \frac{\tan(\varphi)}{\text{FOS}_{\text{n+1}}} \end{aligned} \tag{2.4}$$

where $\text{FOS}_{\text{n+1}}$ is computed as

$$\text{FOS}_{\text{n+1}} = \text{FOS}_{\text{n}} + \Delta\text{FOS} \tag{2.5}$$

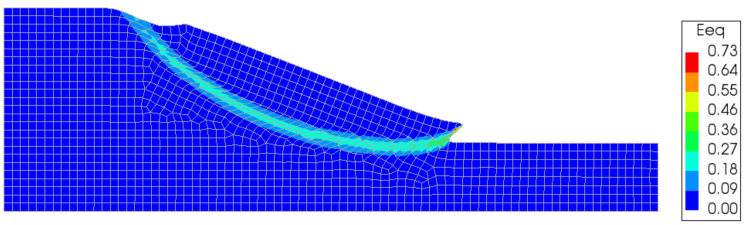

Figure 2.3: Typical result of a strength reduction analysis. The figure shows the mode of the slope at the final factor of safety. The colour indicates the equivalent Von Mises strain.

with ΔFOS a user specified FOS increment. At a certain point during the analysis, no equilibrium can be found within the user specified iteration limit. Then the FOS increment is divided by 2 and the new FOS becomes

$$FOS_{n+1} = FOS_n + \frac{\Delta FOS}{2} \tag{2.6}$$

This procedure is repeated till a user specified tolerance of the FOS is reached. The corresponding FOS is the final FOS, indicating the stability of a slope. The slope is stable if the FOS is larger then 1 and the slope is unstable if the FOS is smaller then 1. The reduced stresses are computed from the stresses obtained in the previous reduction step during the non-linear analysis. First the total strains of the previous reduction step are computed as

$$\boldsymbol{\epsilon}_0 = \boldsymbol{C} : \boldsymbol{\sigma}_0 \tag{2.7}$$

where $\boldsymbol{C}$ is the compliance stiffness matrix. The new stress is computed from the total strains $\boldsymbol{\epsilon}_0$. A return mapping scheme is used to compute the new stresses, if the stress is outside the yield contour due to the reduced strength parameters. Next, the residual force vector is computed as

$$\boldsymbol{r} = \int \boldsymbol{B}^{\mathrm{T}}(\boldsymbol{\sigma}_0 - \boldsymbol{\sigma}) \tag{2.8}$$

From here on, equilibrium is sought with a standard non-linear iteration procedure. A typical failure mode, obtained with a SRM analysis is shown in Figure 2.3. The colours represent the equivalent Von Mises strain [1].

In the MSRM the reduction of the friction angle and the cohesion is done manually. A single step gravity turn on (single load step of the self weight) is applied on a FE-model, with initial (non-reduced) values of the friction angle and the cohesion. Then equilibrium iterations are performed. If the analysis does converge within a user specified amount of iterations, the strength parameters are reduced and the analysis is run again. This reduction is done until the model does not converge within a certain amount of iterations, just as in the SRM. The main difference with the SRM is that the user has to reduce the strength parameters themselves (strength parameters are not reduced automatically) and initial stresses (loading history) are not considered. This is the strength reduction method applied by Griffiths and Lane [9]. As stated before, a single step gravity turn on is applied, followed by equilibrium iterations and no initial stress situation is used as in the SRM. The factor of safety is computed from equation 2.4 at the moment of non-convergence. The results of Griffiths and Lane are used as reference and therefore it is chosen to apply the same method, along with the SRM.

2.3. The single load increment method and the multiple load increment method

Manzari and Nour [17] use another method for assessing the stability of a slope. They assess the stability of a slope with a critical stability number (CSN) instead of a FOS. However, the FOS and the stability number can be related, which will be explained later in Section 3.4. The stability number is defined as

$$N_s = \frac{\gamma H}{c} \tag{2.9}$$

where γ is the unit weight of the soil, H is the height of the slope and c is the cohesion. The unit weight is increased during an analysis instead of reducing the friction angle or the cohesion. Global failure of the slope occurs if large vertical displacements take place in a part of the slope that is sliding with respect to the stable part of the slope. It is stated that the slope fails when this happens and the corresponding stability number is the CSN.

The results from the research of Manzari and Nour [17] are used as reference. However, it is not mentioned in their paper how many load increments are used during an analysis. It could be that they used multiple load increments or they used a gravity turn on (single load step) followed by equilibrium iterations (as applied in the research of Griffiths and Lane [9]). Therefore, it is chosen to do analyses with multiple load increments and with a gravity turn on procedure. The former is called the multiple load increment method (MLIM) and the latter the single load increment method (SLIM).

[1] Appendix B gives the definition of the equivalent Von-Mises strain.

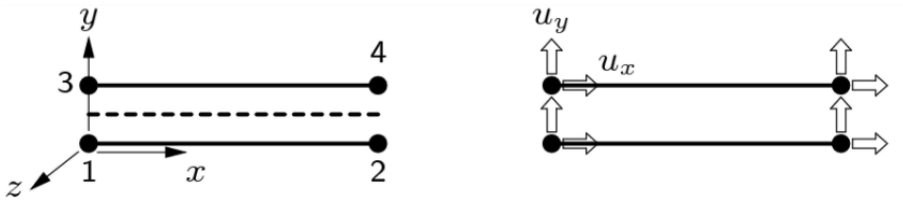

Figure 2.4: 4-node interface element. Figure is taken from [2].

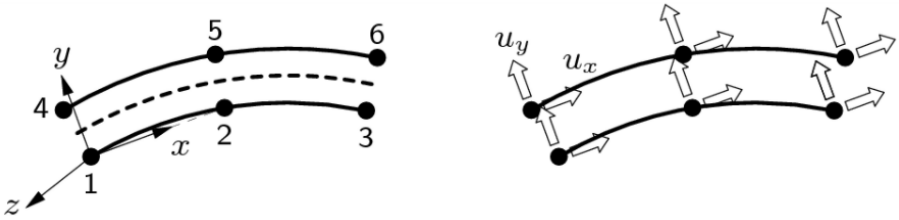

Figure 2.5: 6-node interface element. Figure is taken from [2].

2.4. Models with interface elements

This section gives information of interface elements, utilised for modeling a slip surface. The interface elements can exhibit a jump in the displacement field. Therefore, the models with interface elements are perfectly suited for verification of the enrichment elements in a FE-model of a slope, since both elements can reproduce the same kinematic behaviour. The models with interface elements are analysed with the SLIM and the MLIM in order to obtain a CSN. This CSN is used as a benchmark for verification of the development version of the PM. The remainder of this section provides information about the interface elements.

There are two categories of interface elements [23]. The first category is the zero thickness elements and the second category is the tiny thickness or open interface elements. Interface elements with zero thickness are used in this report, so the nodes are lying on top of each other. If the model is generated with 4-node quadrilaterals, then 4-node line interface elements are used to model the slip surface (see Figure 2.4). 6-node line interface elements are used if the model is run with 8-node quadrilaterals (see Figure 2.5). In this way, compatibility is guaranteed. A normal and shear stiffness modulus have to be defined, which are the elastic material properties. The value of the normal stiffness modulus is based on the following rule of thumb.

$$d_n \approx \frac{E \cdot 1000}{h} \tag{2.10}$$

with E the Young's modulus, and h the element size. Evaluating this rule of thumb results in a relatively large stiffness, which is needed to keep the displacements of the nodes of the interface elements small in the linear elastic stage. Therefore, these stiffnesses are also called penalty or dummy stiffnesses. The assumption is made that the shear stiffness modulus, d_s, is smaller by a factor of 1000. The dimension of the stiffness moduli is force per area per length, *i.e.*, stress per length, for instance N/m^3. The interface elements obey a Mohr-Coulomb friction law. This means that failure in the interface elements occurs if a critical Mohr-Coulomb shear traction is reached. A Newton-Cotes quadrature scheme is used for numerical integration of the stiffness matrix to prevent possible traction oscillations [7].

2.5. The extended finite element method (XFEM)

The extended finite element method (XFEM) is the basically the same as the generalized finite element method (GFEM) [27]. XFEM is GFEM specifically applied to the analysis of discontinuities. GFEM originated from the partition of unity finite element method (PUFEM) [12]. From here on, only the name XFEM will be used.

With standard FEM, it is only possible to model strong discontinuities or weak discontinuities with conforming or matching meshes [16], in which the element edges align with the discontinuities. A strong discontinuity is a jump in the solution field, where a weak discontinuity is a jump in the gradient. The weak discontinuities are reproduced due to the C^0 continuity of the mesh. Elements with double nodes, like interface elements, are needed to be able to represent strong discontinuities like cracks. This means that the representation of the discontinuity is dependent on the location of the elements. For example, in a non-linear analysis a crack must propagate through

interface elements. Hence, the result is not very accurate (when the exact location is not known on forehand) and the elements must be modeled around the discontinuities, which may be a tedious and time consuming job. A solution to this problem is to use adaptive meshes, however this is very computationally expensive [16].

With XFEM it is possible to reproduce discontinuities in the solution field, independent of the mesh. This is possible for strong and weak discontinuities. The down side is that the complexity is moved inside the elements containing the discontinuities (these elements are called enrichment or representing elements in XFEM). Now algorithms are needed for detecting which elements contain the discontinuities and where the discontinuities cross the element edges. Also, numerical integration is more complex, since the element has to be divided into integration elements to be able to numerically integrate the enrichment functions exactly. However, XFEM is performing better than the standard FEM in solving problems with evolving geometric features, such as crack propagation [3].

2.5.1. FEM formulations

The information in this section and Section 2.5.2 is based on the book "Fundamentals of Enriched Finite Element Methods" written by Duarte, Simone and Aragón [8] (to be published in 2022) and on the lecture notes from the course "Enriched Finite Element Methods, ME46080" given by Alejandro M. Aragón.

The standard test/trial FEM space is given by the set of all functions that can be written as a linear combination of finite element shape functions as

$$S_h = \left\{ u^h | u^h = \sum_{\alpha \in I_h} \varphi_\alpha(x) \hat{u}_\alpha, \quad \hat{u}_\alpha \in \mathbb{R} \right\} \tag{2.11}$$

where φ_α are the standard FEM shape functions, associated with nodes x_α, $\alpha \in I_h$, where $I_h = \{1,...,n\}$ is the set of nodes in the mesh. $\hat{u}_\alpha$ are the degrees of freedom (DOFs) and $\mathbb{R}$ is the set of all real numbers.

XFEM can be interpreted as a FEM method with an enriched test/trial space. The standard finite element approximation space, S_h from 2.11, is augmented with the enrichment space, S_e as

$$S_e = \left\{ u^h | u^h = \sum_{\alpha \in I_h^e} \sum_{j=1}^{m_\alpha} \tilde{u}_{\alpha j} \phi_{\alpha j}(x) = \sum_{\alpha \in I_h^e} \varphi_\alpha(x) \sum_{j=1}^{m_\alpha} \tilde{u}_{\alpha j} E_{\alpha j}(x), \quad \tilde{u}_{\alpha j} \in \mathbb{R} \right\} \tag{2.12}$$

where $\tilde{u}_{\alpha j}$ are the enriched DOFs, I_h^e are the enriched nodes, $\phi_{\alpha j}(x)$ are the generalized FEM shape functions, which are the basis functions of a XFEM enrichment space. These generalized FEM functions are a product of Lagrangian finite element shape functions, $\varphi_\alpha(x)$, and an enrichment function $E_{\alpha j}(x)$. α is the index of the node in the mesh and j is the index of the enrichment functions at that node. This means that there are m_α enrichment functions at a node.

The enrichment functions $E_{\alpha j}$ are chosen such that they can reproduce the unknown solution appropriately. This function selection is based on *a priori* knowledge about the problem. This can be the existence of strong and weak discontinuities, or any other phenomenon which can be described by a function.

The total XFEM approximation space is a superposition of the standard FEM space and the XFEM enrichment space

$$S_{XFEM} = \left\{ u^h | u^h = \underbrace{\sum_{\alpha \in I_h} \hat{u}_\alpha \varphi_\alpha(x)}_{\text{std. FEM}} + \underbrace{\sum_{\alpha \in I_h^e} \varphi_\alpha(x) \sum_{j=1}^{m_\alpha} \tilde{u}_{\alpha j} E_{\alpha j}(x)}_{\text{enriched XFEM}}, \quad \hat{u}_\alpha, \tilde{u}_{\alpha j} \in \mathbb{R} \right\} \tag{2.13}$$

Just as with standard FEM, this expression can be substituted in the weak form of the governing equations, obtained through the Galerkin weighted residual method. The enriched DOFs, $\tilde{u}_{\alpha j}$, can be added anywhere in the system matrix. Probably, the most practical way is to first add the standard FEM DOFs in the system and next the enriched DOFs per node.

In the enriched space from 2.12, the Lagrangian shape functions $\varphi_\alpha(x)$ are present. These shape functions form a partition of unity (PoU). The result of this PoU is that the enrichment is exactly represented within the support of the node (group of elements around an enriched node).

2.5.2. Enrichment functions for discontinuities

To model weak discontinuities, the following level set function can be used

$$\phi(\mathbf{x}) = ||\mathbf{x} - \mathbf{x}_{min}|| \operatorname{sign}\left((\mathbf{x} - \mathbf{x}_{min}) \cdot \mathbf{n}_{min}\right) \tag{2.14}$$

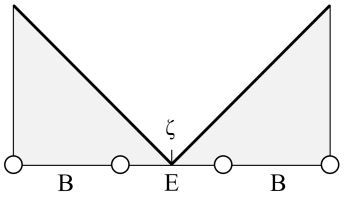

Figure 2.6: Absolute sign distance function with a discontinuity at ζ. The blending elements are indicated by a B and the enrichment element by an E.

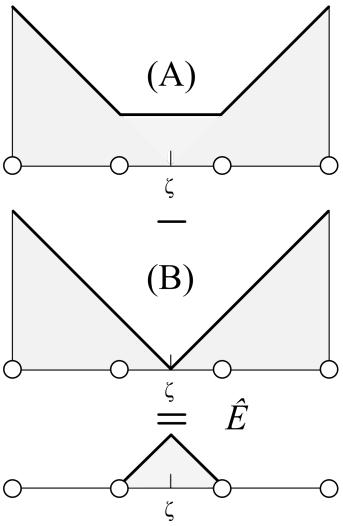

Figure 2.7: Construction of the Möes enrichment function, $\hat{E}$.

This function represents the shortest distance from a certain point x_i to the discontinuity. The sign function states whether the distance is positive or negative.

The absolute value of this sign distance function can be used as enrichment function, which was explored by Sukumar *et al.* Therefore, this enrichment function is called the Sukumar enrichment function, also known as the ramp enrichment function. An example of the absolute distance function is shown in Figure 2.6.

Because this enrichment function is non-zero in the blending elements (elements next to the enrichment elements), some strange behaviour of the approximation may occur and it degrades the convergence rates. This is why it is better to use enrichment functions which are exactly zero in the blending elements.

An enrichment function which is exactly zero in the blending elements is the enrichment function proposed by Möes *et al.*, given in equation 2.15 and shown in Figure 2.7. This enrichment function is called the Möes enrichment function, also known as shifted ramp function. The Möes enrichment function is only active in the enrichment elements and therefore only represented in the enrichment elements. Hence, the DOFs at the nodes retain their physical meaning. Further information about the XFEM method and examples are given in appendix A.

$$M(x) = \underbrace{\sum_{i \in i_h} |\phi(\mathbf{x}_i)| \varphi(\mathbf{x})}_{\text{(A)}} - \underbrace{\left| \sum_{i \in i_h} \phi(\mathbf{x}_i) \varphi(\mathbf{x}) \right|}_{\text{(B)}} \tag{2.15}$$

2.5.3. XFEM applied in the PM

XFEM is a useful method when *a priori* knowledge about the physical problem is available. This is also the case for models with interface elements. This knowledge may be the location of a weak or strong discontinuity and this discontinuity must be predefined in the model. This makes the method not very flexible and creating the FE-models is still a tedious job. However, this *a priori* knowledge is not needed in the PM, since enrichment functions are added in elements when onset of localisation is detected in those elements.

Figure 2.8 shows a localisation band with normal vector $\mathbf{n}$ and slip vector $\mathbf{m}$ (direction of the plastic flow). Across this localisation band the gradient of the displacement field is discontinuous. This is a weak discontinuity.

The width of the localisation band is relatively small compared with the rest of the geometry. Therefore, it is allowed to set the width of the shear band to zero, which still gives a good approximation of the shear band [26] and simplifies the method. When taking the width of the band to zero in the limit, the displacement field itself becomes discontinuous, and thus becomes a strong discontinuity. The shear band becomes a surface in 3D or a curve in 2D.

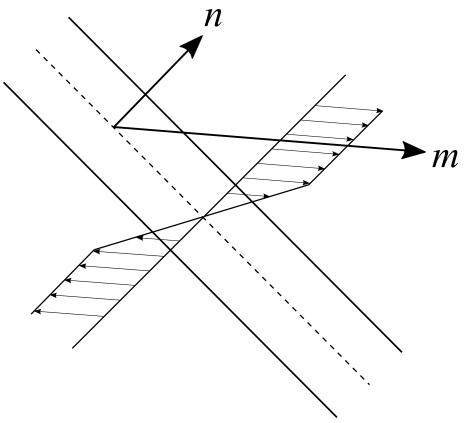

Figure 2.8: Geometry of a weak discontinuity with the normal vector **n** and the slip vector **m**.

The onset of localisation in elasto-plastic solids is detected by a search algorithm described by Leroy and Ortiz [29] for associated plastic flow. Sanborn and Prévost [26] expanded the search algorithm for non-associated plasticity. When the yield criteria are reached (detected in the integration points) in an element, an algorithm for detecting onset of localisation starts. This algorithm is described in Chapter 6.1. In Chapter 1.4, it was shown that the determinant of an acoustic tensor must be zero for onset of localisation to occur. This acoustic tensor is the tangential material stiffness matrix pre- and post-multiplied with the vector normal (vector **n** in Figure 2.8) to the discontinuity. When the determinant is zero, ellipticity of the governing equations is lost. At this point, onset of localisation occurs. By solving this eigen value problem, the direction θ of the normal vector **n** is obtained as is the direction of the plastic flow (vector **m** in Figure 2.8). The vectors **m** are the eigen vectors of the corresponding singular acoustic tensor.

For soils and rocks dilatant behaviour is observed on the cracks and this is why the the slip direction is not perpendicular to the normal of the discontinuity [22]. The solution of this eigen value problem contains multiple directions for the onset of localisation. To choose the appropriate direction, the method of Regueiro *et al.* [22] is adopted. In this paper the direction of the maximum displacement gradient is chosen by $\max(\nabla \boldsymbol{u} : \boldsymbol{m} \otimes \boldsymbol{n})$. After detection of onset of localisation, another algorithm searches for localisation in adjacent elements. Sanborn and Prévost [26] guarantee continuity of the localisation band as follows. If localisation is detected in tip elements, then the shear band is extended by applying enrichment functions to those elements. Of the possible direction vectors $\boldsymbol{n}$, the direction is chosen that is closest to previous direction in the shear band. The band is extended slightly past the edge of the next element.

When localisation in an element is detected, enrichment functions are added to the nodes of the element. This means that extra degrees of freedom (DOFs) are added to the system. These extra enrichment functions augment the standard finite element (FE) space. Shifted Heaviside functions are chosen as enrichment functions. Once inserted, the discontinuities obey a Mohr-Coulomb friction law, which is enforced by a penalty method.

The PM for analysing slope stability can be summarized as follows. Initially, the model contains only standard plane strain continuum elements. This may be 4- or 8-node quadrilaterals for example. Then a load is applied on the system. The load is incremented until an algorithm detects onset of localisation inside an elasto-plastic solid. At this moment, XFEM enrichment functions are added to the localised elements, which are able to reproduce a jump in the displacement field. Then an algorithm searches for onset of localisation in adjacent elements. The procedure of adding enrichment functions to the localised elements continues. These elements are now enrichment elements, which obey a Mohr-Coulomb friction law and may exhibit a jump in the displacement field. Global failure of the slope occurs when the slip surface (localisation band of zero thickness) is fully developed. At this moment, a CSN can be computed according to 2.9. Chapter 3.4 explains the relation between the FOS (equation 2.4) and the CSN (equation 2.9).

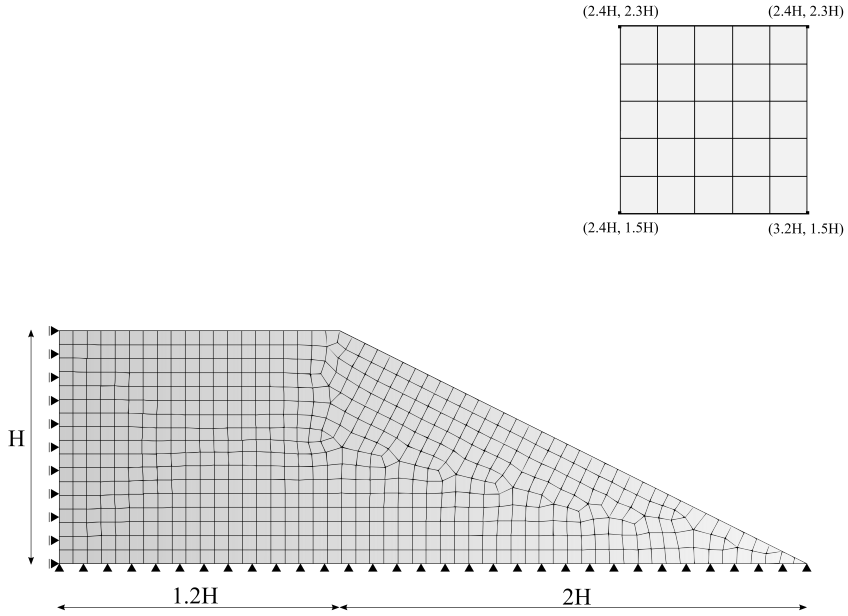

Figure 3.1: Plane strain FE model of a slope with no foundation. The angle of the slope is 26.57° (2 : 1). Rollers on the left constrain the displacement in x-direction and the supports at the bottom constrain displacements in x- and y-direction. The slip surface grid is shown in the top right corner.

3

Application of the analysis methods

In Chapter 1.2 it was stated that reliable benchmarks must be obtained with numerical slope stability analysis methods, which can be used for verification of the point of global failure of a slope in analyses with the PM. This chapter explains how these benchmarks are generated with the analysis methods described in the previous chapter.

In the previous chapters is was explained that the stability of a slope is assessed by a FOS or a similar CSN. Therefore, the FOS and CSN give an indication of the point of global failure of a slope. Hence, the FOS and CSN are used as benchmarks for verification of the point of global failure in analyses with the PM. In Chapter 1.2 it was stated that the slope stability analysis method of Manzari and Nour [17] (SLIM/MLIM) can be used for computing a CSN with the PM. In the following it will be explained which FE-models and corresponding analyses are used for obtaining the benchmarks and how the results are presented.

The first section describes how the results are obtained and displayed for methods based on strength reduction and the SSM. The second section describes the same for methods based on load increments. Both sections describe the FE-models, the material properties and the analysis settings. Then a sections follows about the convergence

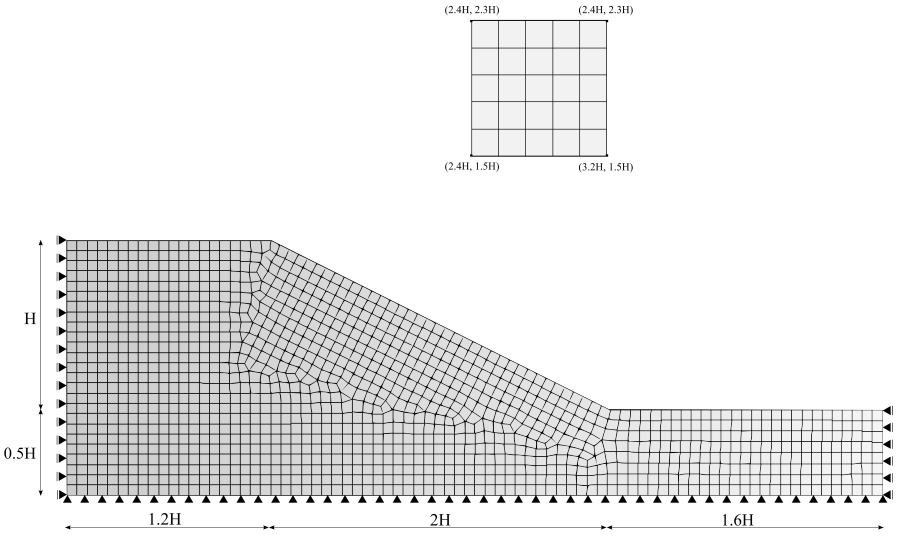

Figure 3.2: FE model of homogeneous slope with foundation layer. Rollers on the left constrain the displacement in x-direction and the supports at the bottom constrain displacements in x- and y-direction. The slip surface grid is shown in the top right corner.

and parameter studies. The last section in this chapter explains the relation between analysis methods based on strength reduction and methods based on load increments. Verification of onset of localisation on local level is discussed in Chapter 6.

3.1. Application of methods based on strength reduction

The FE-models used for computing the FOS and failure modes with the analyses based on strength reduction are based on the models of Griffiths and Lane [9]. The models are shown in Figure 3.1 and 3.2. These models are chosen because the results of Griffiths and Lane serve as a reference. The only difference between the models in Figure 3.1 and 3.2 is the foundation layer.

The soil is modeled with plane strain elements, which obey the following Mohr-Coulomb plasticity rule.

$$F(\boldsymbol{\sigma}) = \frac{1}{2}(\sigma_1 - \sigma_3) + \frac{1}{2}(\sigma_1 + \sigma_3)\sin\varphi - c\cos\varphi = 0 \tag{3.1}$$

The properties of the soil are

$$\psi = 0\,[^\circ], \qquad \varphi = 20\,[^\circ], \qquad \frac{\gamma H}{c} = 20\,[-], \qquad E = 2\cdot 10^8\,[\mathrm{N/m^2}], \qquad \nu = 0.3\,[-] \tag{3.2}$$

where ψ is the dilatancy angle, φ is the friction angle, E the Young's modulus and ν the Poisson ratio. $\gamma H / c$ is the stability number (see Chapter 2.3), which is a dimensionless value. c is the cohesion, γ is the unit weight of the soil and the dimensions of the model are expressed in H. A value of 10 meter is chosen for H, the value of γ is 20000 N/m^3 and the cohesion is 10000 N/m^2. It may be noted that the value of the friction angle and the cohesion are initial values, which are reduced during the analysis. All analyses are run with bi-linear quadrilateral (Q4) and quadratic quadrilateral (Q8) elements [1]. Q4 elements are chosen, because the PM will initially be developed for Q4 and T3 elements. Q8 elements are applied because Griffiths and Lane [9] used Q8 elements and therefore a better comparison with their results can be made. Also, Q8 elements will give better results for a given mesh size, since the rate of convergence in the energy norm of quadratic elements is approximately 1 and 0.5 for linear elements [19].

The SRM requires an initial stress state to be able to run the analysis. This stress state may represent the loading history of the soil. The stresses in the soil elements are computed due to the self weight and are used as an initial stress state of the soil elements in the next step. The FOS is computed after every reduction as described

[1] Due to the meshing a few T3 or T6 elements may be present in the mesh. However, by far the most elements are Q4 or Q8 elements and therefore reference will be made to Q4 or Q8 elements in the results.

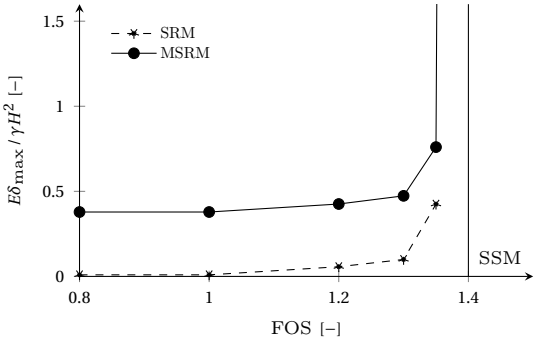

Figure 3.3: Dimensionless maximum displacement versus the FOS. A rapid increase of displacements indicate failure of the slope. The FOS of the SSM is indicated by the vertical line.

in Chapter 2.2. The initial FOS of the models is 1, the initial increment of the FOS is 0.1 and the FOS tolerance is 0.0125. The equilibrium iterations are executed with a secant Quasi-Newton scheme [2] with an iteration limit of 1000. The MSRM does not require an initial stress state and the load is applied with a single load step per analysis. The displacement field is computed during the analyses and the maximum vertical displacement, δ_{max}, is normalised according to

$$\frac{E\delta_{max}}{\gamma H^2}\,[-] \tag{3.3}$$

which is a dimensionless quantity. This dimensionless displacement is plotted versus the FOS. An example is shown in Figure 3.3. The results are generated with the SRM and the MSRM. Those plots capture the kinematic behaviour of the soil with respect to the FOS. Failure of the slope is indicated by a rapid increase in displacements. Griffiths and Lane [9] state that this rapid increase in displacements is analogous to non-convergence of the analysis and therefore they choose to use this non-convergence as failure criterion. The corresponding value of the FOS is the final FOS.

The FOS obtained with the SSM is only computed in the first analysis, *i.e.*, during the analysis with the initial values of the soil parameters. This is because the SSM computes the FOS from the stresses in the soil (see Chapter 2.1). Hence, the displacements are not plotted versus the FOS for the SSM. The FOS computed with the SSM will be indicated by a vertical line, as shown in Figure 3.3, or is given in a table. A slip surface grid is shown in the top right corner of Figure 3.1 and 3.2. Slip surfaces are generated from the grid points with radii of 15 to 22 meters, with increments of a 0.5 meter.

[2] Better results were obtained with this iteration scheme than a standard Newton-Raphson scheme.

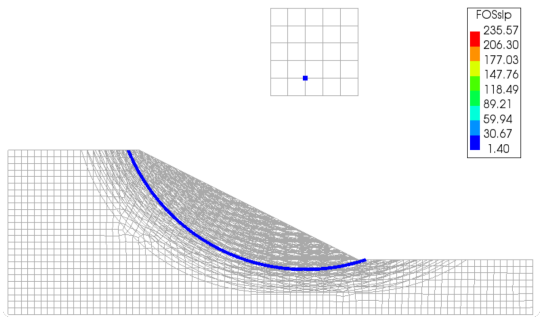

Figure 3.4: A critical slip surface computed with the SSM.

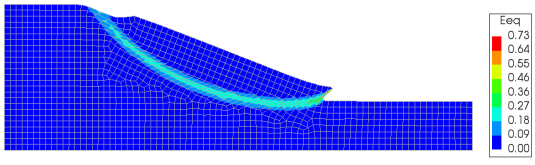

Figure 3.5: Failure mode of the slope with computed with the MSRM.

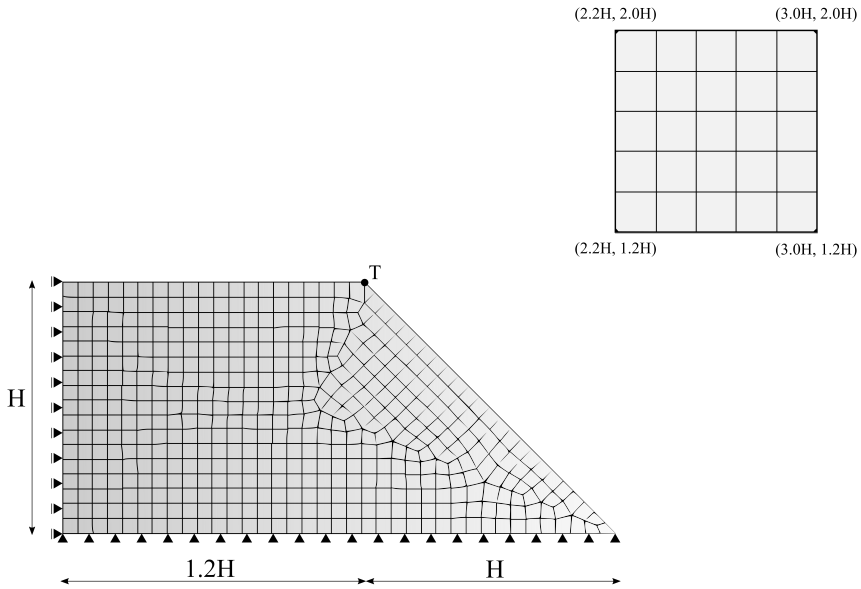

Figure 3.6: FE model of a homogeneous slope with no foundation. The angle of the slope is 45°(1 : 1). The vertical displacement is computed at the tip of the slope, denoted by T.

The plots with the normalised displacement versus the FOS and the final FOSs will serve as benchmark for the PM. However, the PM falls in the category of analysis methods based on load increments. Section 3.4 explains how the two categories are related.

Additional verification of the PM can be done with benchmarks based on the geometry of the critical slip surfaces and localisation bands. An example is shown in Figure 3.4 and 3.5. Figure 3.4 shows the critical slip surface, computed with the SSM. The center point of the circle is indicated by the blue dot in the grid. Figure 3.5 shows the failure mode of a slope, computed with the MSRM. The light blue colour indicates the localisation band (with finite width). The critical slip surface is inside this band. Those critical slip surfaces, localisation bands and failure modes can be compared with the slip surfaces computed with the PM. Appendix B provides additional information about verification of the slip surface geometry.

3.2. Application of methods based on load increments

The SLIM and MLIM are analysis methods based on load increments and the results of those methods is a CSN. The methods are applied on the FE-model of Figure 3.6. This model is based on the model of Manzari and Nour [17] and the results of their research will serve as reference. In Chapter 5.3 a slip surface is pre-defined in the slope of Figure 3.6, modeled with interface elements. The results of the model with interface elements are used for verification of a development version of the PM.

$$\varphi = 30\,[°], \qquad H = 10\,[\text{m}], \qquad c = 10000\,[\text{N/m}^2], \qquad E = 2\cdot 10^8\,[\text{N/m}^2], \qquad \nu = 0.3\,[-] \tag{3.4}$$

The Mohr-Coulomb plasticity rule of equation 3.1 is used. The unit weight, γ, is increased in analyses with the SLIM and the MLIM. A secant Quasi-Newton scheme is used for the equilibrium iterations with a ceiling of 1000 iterations.

The benchmarks generated with methods based on load increments are in the form of dimensionless displacement versus stability number (SN) plots. The vertical displacements at the tip of the slope, indicated by a T in Figure 3.6, are used for generating the plots. An example of an normalised displacement versus SN plot is shown in Figure 3.7. A rapid increase of displacements indicate global failure of the slope and the corresponding SN is the CSN of the slope. Manzari and Nour [17] applied the following dimensionless displacement

$$\frac{G\delta}{Hc}\,[-] \tag{3.5}$$

with G the shear modulus, which attains a value of $8.846\cdot 10^7$ N/m^2, and is computed from the Young's modulus.

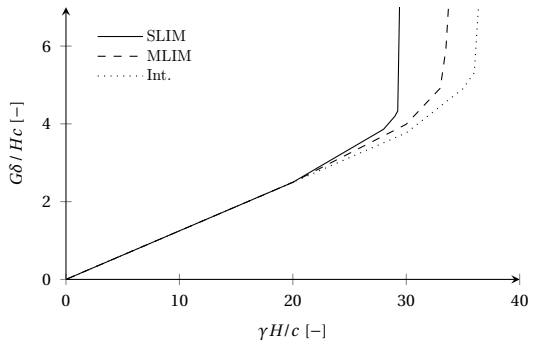

Figure 3.7: Example of a benchmark generated with the MLIM, SLIM and a model with interface elements (Int.). A dimensionless vertical displacement is plotted versus the stability number. A rapid increase of displacements indicate global failure of the slope and the corresponding SN is the CSN of the slope.

3.3. Convergence and parameter studies

In Chapter 4 and 5, convergence studies are performed in order to obtain reliable values of the FOS and CSN which can be used as benchmarks. In those studies, four different mesh sizes of 0.25m, 0.5m, 1m and 2m are used for the aforementioned FE-models. The resulting FOSs and CSNs of the analysis of those models should converge to a certain value if the mesh size is reduced. These (converged) values serve as reliable benchmarks, applicable for verification of the PM.

Griffiths and Lane [9] and Manzari and Nour [17] did not mention which convergence criteria is used in the FE-analyses and therefore it is chosen to use a force vector based convergence criteria. Then convergence occurs if the following criterion is met

$$\frac{\sqrt{\boldsymbol{g}_i^T \boldsymbol{g}_i}}{\sqrt{\boldsymbol{g}_0^T \boldsymbol{g}_0}} <= c \tag{3.6}$$

where $\boldsymbol{g}_0$ is the initial residual force vector and $\boldsymbol{g}_i$ are the residual force vectors obtained in the next iterations ($i = 1, ..., n$). A value of 0.01 and 0.001 is taken for c, which is the threshold value of the criterion.

Parameter studies are performed, additional to the convergence studies. In Chapter 4.1 the effect of the Poisson ratio on the FOS is studied and Chapter 5.1 provides studies of the effect of the dilatancy angle on the CSN. Various values are used for the Poisson ratio and dilatancy angle in the FE-analyses. The results are presented in the aforementioned displacement versus FOS/CSN plots. The objective is to obtain characteristic behaviour from those plots, which can be related to the variation of the soil parameters. Then this characteristic behaviour can be used to verify whether the variations of the soil parameters have the same effect on the results of the PM.

3.4. Relation between methods based on strength reduction and methods based on load increment

This section explains the relation between methods based on strength reduction and methods based on load increments. This relation is needed in order to be able to verify the point of global failure of the PM, indicated by the CSN, with the FOS of the SRM and the SSM. First, the relation is demonstrated with numerical examples, followed by a physical explanation.

The model of the slope without foundation layer in Figure 3.1 is analysed with the SRM and the MSRM. The material and analysis properties are given in Chapter 3.1. In every analysis, a stability number with an initial value of 20 is used, but with a different combination of γ, H and c. This will demonstrate that a different combination of those parameters does not have any influence on the FOS if the initial value of the stability number is the same

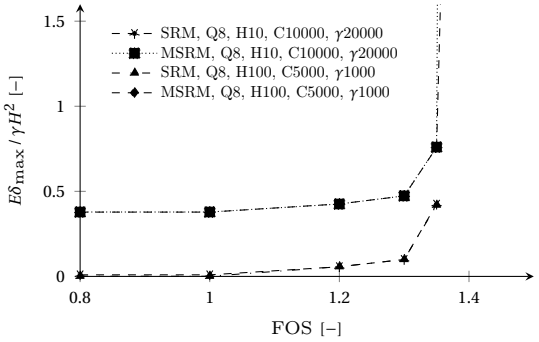

(a) Results of FE analyses with Q8 elements.

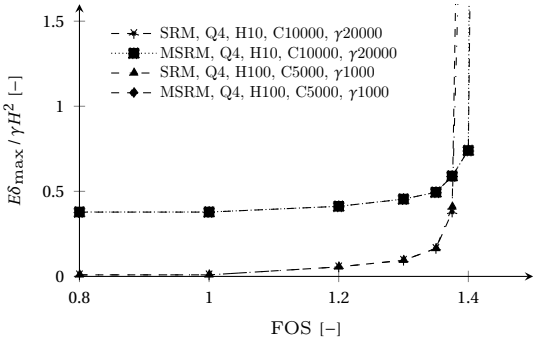

(b) Results of FE analyses with Q4 elements.

Figure 3.8: FOS versus dimensionless displacement of a slope without a foundation. Different values for c, γ and H are taken, but such that the initial value of the stability number, $\gamma H / c$, is 20.

in every analysis [3]. First, analyses are done with $\gamma = 20000\,\mathrm{N/m^3}$, $H = 10\,\mathrm{m}$ and $c = 10000\,\mathrm{N/m^2}$. Then, analyses are run with $\gamma = 1000\,\mathrm{N/m^3}$, $H = 100\,\mathrm{m}$ and $c = 5000\,\mathrm{N/m^2}$.

Figure 3.8 shows that a different combination of γ, H and c, does not result in a different dimensionless displacement and thus the final FOS is the same. This gives the opportunity to establish a relation between methods based on strength reduction and methods based on load increments. With this relation it is possible to compare the CSN, computed with methods based on load increments, with the FOS computed with methods based on strength reduction. The relation can be established through the definition of the stability number, $N_s = \gamma H / c$ and the definition of the FOS of the SRM, $c_{n+1} = c / \mathrm{FOS}_{n+1}$ and $\tan(\varphi_{n+1}) = \tan(\varphi) / \mathrm{FOS}_{n+1}$. Now, lets say that only the cohesion is reduced during a SRM and that the final FOS is equal to a factor λ. Then the reduced value of the cohesion is

$$c_{n+1} = \frac{c}{\mathrm{FOS}_{n+1}} = \frac{c}{\lambda} \tag{3.7}$$

Substitution of this reduction in the definition of the stability number gives

$$N_s = \frac{\gamma H}{(c / \lambda)} = \lambda \cdot \frac{\gamma H}{c} \tag{3.8}$$

This shows that reduction of the cohesion with a factor λ has the same result as increasing the unit weight with this factor λ. Another explanation can be given with use of the Mohr-Coulomb envelope shown in Figure 3.9. Lets assume that a point in the soil has an initial stress situation, represented by the stress point (σ_1, τ_1) (red dot) and this stress point is initially inside the Mohr-Coulomb stress envelope. Then due to reduction of the cohesion by a factor 2, the stress point (σ_1, τ_1) suddenly lies on the Mohr-Coulomb envelope. Now lets increase the stress state by a factor 2, by doubling the unit weight instead of reducing the cohesion. Then the new stress point (σ_2, τ_2) also lies on the edge of the Mohr-Coulomb envelope. Therefore, decreasing the cohesion by a certain factor has the same effect on the stress point as increasing the unit weight by this factor, with respect to the maximum Mohr-Coulomb shear stress.

Now a relation is established between strength reduction methods and load increment methods. However, this relation is only based on a reduction of the cohesion. Figure 3.10 gives numerical proof to substantiate those statements. Two analyses are run with Q8 elements. The cohesion is reduced in one analysis, while the unit weight is increased in the other and the resulting curves in Figure 3.10 are the same.

The next objective is to find a relation between methods with a full strength reduction (reduction of the cohesion and of the friction angle) and methods based on load increments. The only addition to a full strength reduction analysis is that the friction angle is also reduced besides reduction of the cohesion. This means that the

[3] The value of the stability number changes, due to reduction of the cohesion during the analyses.

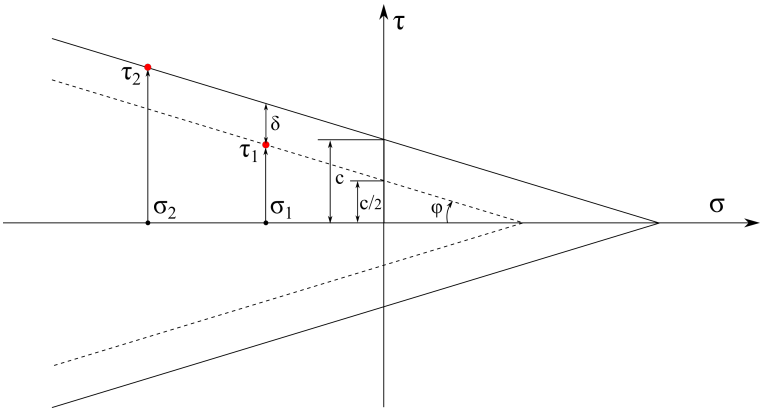

Figure 3.9: Change of the Mohr-Coulomb envelope due to reduction of the cohesion by a factor 2 or change of the stress state due to increasing the unit weight by a factor 2.

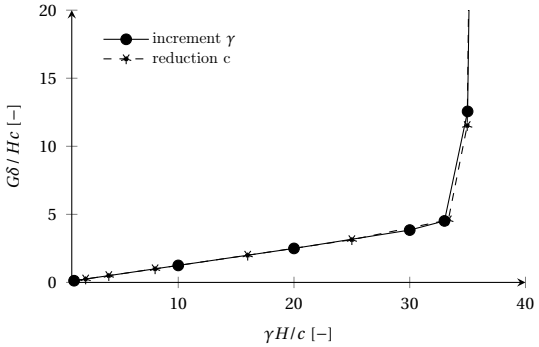

Figure 3.10: Dimensionless maximum displacement versus the stability number of a slope. The cohesion is reduced in one analysis, while the unit weight is increased in the other. The results are generated with 8-node quadrilaterals.

same results can be obtained with a method based on load increments if the friction angle is decreased during the increments of the unit weight. Hence, the following relations are valid

$$\begin{aligned} \gamma_{n+1} &= \frac{\mathrm{FOS}_{n+1}}{\gamma} \\ \tan(\varphi_{n+1}) &= \frac{\tan(\varphi)}{\mathrm{FOS}_{n+1}} \end{aligned} \tag{3.9}$$

The model in Figure 3.1 is analysed with the MSRM and with the SLIM. The friction angle is reduced during the SLIM. Therefore, this method is now not purely based on load increments, but also on reduction of the friction angle. Hence, the resulting method is a **hybrid** method. Figure 3.11 shows that the results of the MSRM are exactly the same as the SLIM with reduction of the friction angle. In this hybrid method, the load is incremented manually and the friction angle is reduced manually, which is a tedious job. However, the analyses can be made more efficient if the load is applied with automatic increments, just as in the MLIM. The only modification would be that the friction angle should be a function of the load increment (or FOS). The relation between the friction angle and the unit weight is obtained by substitution of $\mathrm{FOS}_{n+1} = \gamma \cdot \gamma_{n+1}$ in equation 3.9 and rewriting the equation, which gives

$$\varphi_{n+1} = \frac{\tan(\varphi) \cdot \gamma_{n+1}}{\gamma} \tag{3.10}$$

In accordance with the results of this section the following conclusions are given.

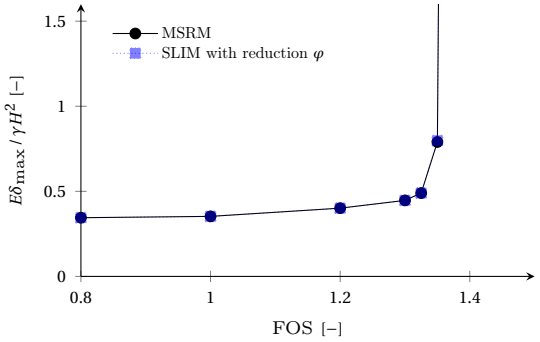

Figure 3.11: FOS versus a dimensionless displacement. Results are generated with the MSRM and with the SLIM. The friction angle is reduced during the SLIM analysis and therefore this method is a hybrid method.

- It is possible to assess the slope stability with the PM by computing a CSN. The CSN is obtained when the slip surface is fully developed. This CSN can be verified with the CSN obtained by the SLIM or MLIM.
- A (hybrid) method is proposed for computing a FOS with the PM, which is similar to a FOS of strength reduction methods and the SSM. Therefore it is possible to utilise the FOS of the strength reduction methods and the SSM as a benchmark for verification of the FOS of the PM.

The last step is to show how the definition of the FOS of the SSM is related to the definition of the FOS of strength reduction methods. For convenience, the definitions are shown again. The definition of the FOS of the SSM is

$$\text{FOS} = \frac{1}{l}\int \frac{\tau_{\text{MC}}}{\tau} d\xi \tag{3.11}$$

which contains the critical Mohr-Coulomb shear stress, which is defined as

$$\tau_{\text{MC}} = c + \sigma_n \tan(\varphi) \tag{3.12}$$

In a SRM the FOS is computed from

$$\begin{aligned} c_{\text{n+1}} &= \frac{c}{\text{FOS}_{\text{n+1}}} \\ \tan(\varphi_{\text{n+1}}) &= \frac{\tan(\varphi)}{\text{FOS}_{\text{n+1}}} \end{aligned} \tag{3.13}$$

Note the similarities between the critical Mohr-Coulomb stress, equation 3.12, and the reduction of the cohesion and the friction angle in equation 3.13. The reduction of the strength parameters in equation 3.13 is based on the reduction of the cohesion and the tangent of the friction angle of the Mohr-Coulomb envelope [24]. The SSM gives an approximation of the most critical slip surface, based on the initial soil situation, *i.e.*, based on the non-reduced soil properties. The method integrates the critical shear stress over the slip surfaces divided by the computed shear stress (local FOS) and the length of the slip surface. This gives a FOS which tells how much capacity is left on this slip surface. The capacity is a factor between the critical Mohr-Coulomb shear stress and the active shear stress on average over the slip circle. This takes into account that locally material failure may occur, but that the system is not failing on global level. Failure of the system only occurs when the average shear stress in the critical slip surface is large enough.

It is expected that the FOS of the SSM is close to the FOS of strength reduction methods, since this is observed in Figure 3.3. Also, there are only relatively small deformations in a SRM until global failure occurs and the excess shear stresses, due to local plasticity, will follow the path of the least resistance. This is similar to finding the critical slip surface with the SSM.

4

Benchmarks generated with analyses based on strength reduction

The results in this chapter can be used for verification of the FOS of the PM. The results may serve as a benchmark if the FOS of the PM is computed according to the hybrid method, *i.e.*, if the unit weight is incremented and the friction angle reduced in the PM. The FE-model and the material properties are given in Chapter 3.1.

First, the effect of the Poisson ratio on the FOS is studied. The FE-model is analysed with the SRM, the MSRM and with the SSM. The analyses are run with various values of the Poisson ratio. The maximum vertical displacement is plotted versus the FOS and the characteristics of these plots can be used for verification of the propagation method.

Next, a convergence study is done in order to obtain a reliable benchmark for verification of the FOS of the PM. The convergence study is performed with the MSRM and in the study four different mesh sizes and two force norms are used.

4.1. Effect of the Poisson ratio on the FOS

The effect of different Poisson ratios on the FOS are shown in Figure 4.1 and 4.2. The results in Figure 4.1 are generated with the MSRM and the results of Figure 4.2 are generated with the SRM. A force norm of 0.01 is used with a maximum of 1000 equilibrium iterations. The FOS is computed with a precision of 0.0125. The values

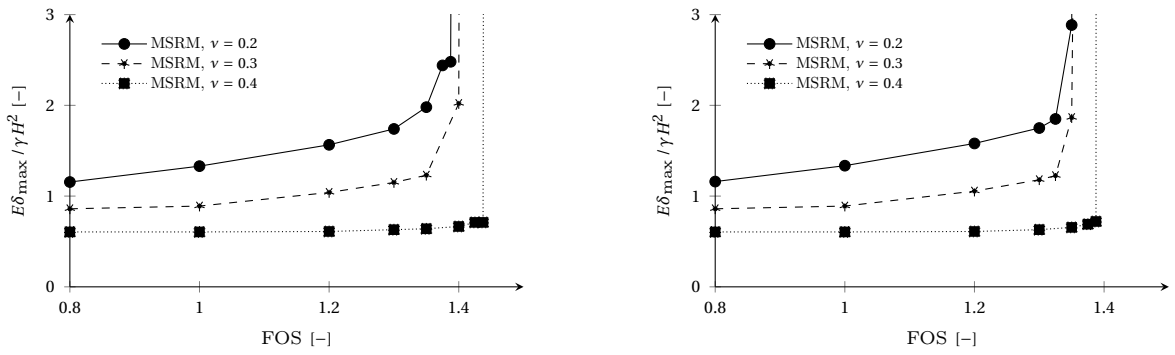

(a) Q4 elements.

(b) Q8 elements

Figure 4.1: Influence of the Poisson ratio on the FOS. The results are generated with the MSRM for the FE-model with foundation layer 3.2. Results are shown for Q4 elements (left figure) and for Q8 elements (right figure).

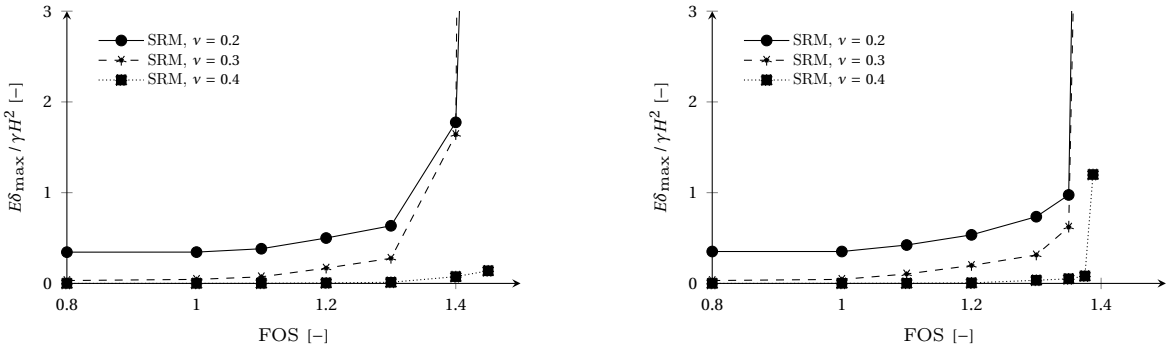

(a) Q4 elements.

(b) Q8 elements

Figure 4.2: Influence of the Poisson ratio on the FOS. The results are generated with the MSRM for the FE-model with foundation layer 3.2. Results are shown for Q4 elements (left figure) and for Q8 elements (right figure).

0.2, 0.3 and 0.4 are used for the Poisson ratio and a mesh size of 0.5 m is used. Both figures show results for Q4 and Q8 elements. A rapid increase in displacements indicate failure of the slope and the corresponding critical FOS can be obtained from the horizontal axis. Table 4.1 gives an overview of the FOS computed with the SRM, MSRM and the SSM.

The results in Figure 4.1a are computed with Q4 elements. From this figure it can be observed that the FOS increases if the Poisson ratio increases. However, from Table 4.1 it can be observed that the differences between the FOS is only 0.025. Figure 4.1b shows results computed with Q8 elements. This figure shows that the FOS, with a value of 1.3625, is equal for a Poisson ratio of 0.2 and 0.3. A Poisson ratio of 0.4 results in a FOS of 1.4, which is larger. Since Q8 elements converge faster to the true solution, it can be concluded that the difference in the FOS of the Q4 elements is probably caused by the poor solution approximation of the Q4 elements for the given mesh size of 0.5 m.

What the figures have in common is the difference in the magnitude of the displacements. The maximum displacements are increasing if the Poisson ratio is decreasing. Thus, the model is acting stiffer if the Poisson ratio is increasing. This is because the elements tend to expand more in the out-of-plane direction if the Poisson ratio becomes larger, but this expansion is constrained by the the plane strain model. Less expansion in out-of-plane direction means less expansion in the in-plane directions due to the constitutive relations. It can also be observed that the failure of the slope is more abrupt if the Poisson ratio is larger and the displacements increase more smoothly for lower values of the Poisson ratio.

The results in Figure 4.2, generated with the SRM, are similar to the results of the MSRM in Figure 4.1. The largest difference is the magnitude of the displacement in the phase before failure of the slope. The displacements of the SRM are smaller because the SRM uses an initial stress state as loading condition on the soil. Therefore, there are almost no displacements before failure of the slope. The MSRM uses an external load on the soil, which results in larger displacements. However, Table 4.1 shows that the final FOS, computed with the SRM, is almost the same as the FOS computed with the MSRM.

Poisson	element	SRM	MSRM	SSM
0.2	Q4	1.4125	1.4	1.41
	Q8	1.3625	1.3625	1.4
0.3	Q4	1.425	1.425	1.39
	Q8	1.3625	1.3625	1.39
0.4	Q4	1.45	1.45	1.41
	Q8	1.3875	1.4	1.41

Table 4.1: FOS for different values of the Poisson ratio computed with the SRM the MSRM and the SSM.

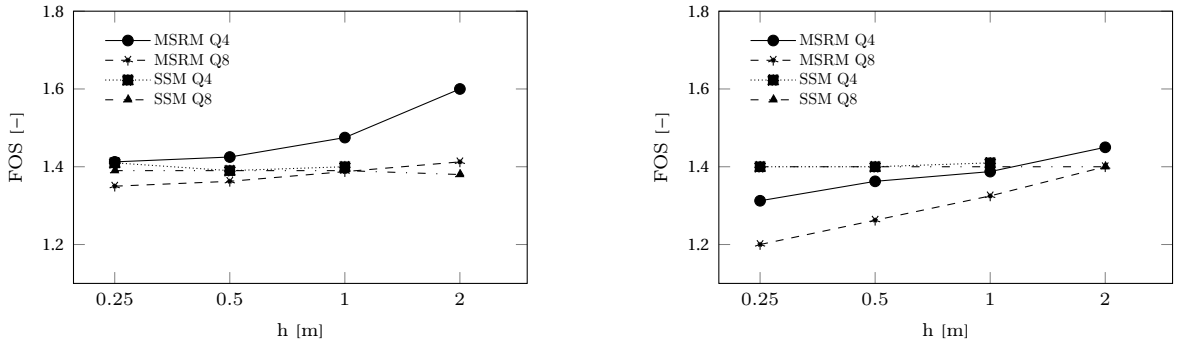

(a) Convergence criterion is 0.01.

(b) Convergence criterion is 0.001.

Figure 4.3: FOS versus mesh size h for Q4 and Q8 elements. The analyses are done with a maximum of 1000 iterations and with a force norm of 0.001 and 0.01 respectively. A log scale is used for the horizontal axis.

The results of the SSM are shown in Table 4.1. It can be observed that the FOS with a value of 1.41 is equal for a Poisson ratio of 0.2 and 0.4. The FOS of a Poisson ratio of 0.3 is 1.39. This is contradictory to the results of the SRM and the MSRM. However, the difference between the values of the FOS is only 0.02 and there are no differences between the FOS computed with Q8 and Q4 elements. This means that for this model, the FOS computed with the SSM is very robust, but the FOS of the SSM does not show characteristic behaviour which can be used for verification of the PM. The SSM also results in a larger FOS than the FOS computed with the SRM and the MSRM with Q8 elements. For this situation, the SRM and the MSRM result in a more conservative FOS than the SSM.

The graphs in Figure 4.1 and 4.2 can be used for verification of the PM. If the propagation method is being tested, the same FE-model with the same analysis properties should be used. The propagation method should be performed with the three values of the Poisson ratio. Then the displacements are computed and plotted versus the FOS. Now, graphs are obtained which must be similar to the graphs in Figure 4.1 and 4.2. If the propagation method is combined with a reduction of the internal friction angle (hybrid method) as described in Chapter 3.4, then also the FOS should be approximately equal. In the next section a convergence study is performed in order to obtain a reliable FOS which can be used as a benchmark.

4.2. Convergence study

In this section a convergence study of the FOS is done with the MSRM and the SSM. The FE-model used is given in Figure 3.2 in Chapter 3.1. The model is based on a model in the paper of Griffiths and Lane [9] and the results obtained in this paper are used as a reference. Four different mesh sizes of 0.25 m, 0.5 m, 1 m and 2 m are used. Griffiths and Lane [9] state that failure of the slope and numerical non-convergence occur simultaneously and that this is accompanied by a vast increase in the displacements within the mesh. The same maximum number of 1000 iterations is used.

The FOS is computed with the MSRM and the SRM for models with Q4 and Q8 elements and plotted versus the mesh size. The results are shown in Figure 4.3 and in Table 4.2. It must be noted that the SSM was not able to compute a FOS for a mesh size of 2 m and Q4 elements. Looking at the plot with a convergence criterion of 0.01, it can be observed that the FOS of the Q4 elements seem to converge to a value of 1.4. However, the FOS of the Q8 elements seem to not converge to a certain value. The results are even worse for the convergence criterion of 0.001. The FOS of the SSM on the other hand, is with an average value of 1.4 and a maximum deviation of 0.2 very stable.

The non-convergence of the FOS is the result of the maximum number of iterations in combination with the mesh size and the convergence criterion. First, in general an analysis with a convergence criteria of 0.001 needs more iterations to find equilibrium than an analysis with a criterion of 0.01, simply because the requirement of the norm of the residual force vector is more strict. For the mesh size it holds that the system of equations becomes

CC	MS	FOS			
		SSM		MSRM	
		Q4	Q8	Q4	Q8
0.01	2	-	1.38	1.6	1.4125
	1	1.4	1.39	1.475	1.375
	0.5	1.39	1.39	1.425	1.3625
	0.25	1.41	1.39	1.4125	1.35
0.001	2	-	1.4	1.45	1.4
	1	1.41	1.4	1.3875	1.325
	0.5	1.4	1.4	1.3625	1.2625
	0.25	1.4	1.4	1.3125	1.2

Table 4.2: FOS for different mesh sizes (MS) and different convergence criteria (CC). The FOS is computed with the SSM and the MSRM.

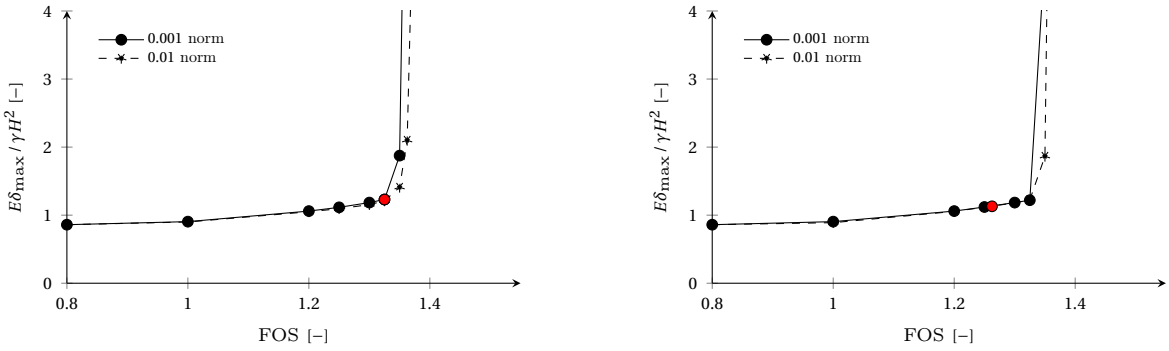

(a) Mesh size h = 1 [m].

(b) Mesh size h = 0.5 [m].

Figure 4.4: FOS versus dimensionless displacement for different convergence norms. The FOS is computed with the MSRM and Q8 elements. The rapid increase in displacements indicates slope failure. The results of Griffiths and Lane [9] are plotted as is the FOS computed by Bishop and Morgenstern [1] indicated by B&M.

larger when the mesh size reduces and a larger system of equations means that more iterations are needed to find equilibrium. As a consequence, the analysis cannot find equilibrium within the specified 1000 iterations for small mesh sizes and a convergence criterion of 0.001. However, this non-convergence may not coincide with slope failure. This is because the displacements, obtained at 1000 iterations, are still equal to the displacements of a converged model with a convergence criterion of 0.01. This is shown in Figure 4.4. The plots are generated with a mesh size of 1 m and 0.5 m. The red dots in these figures indicate non-convergence of the analyses with a 0.001 convergence criterion. It can be observed that this point of non-convergence is still on the graph of the analyses with a convergence criterion of 0.01 [1] and that this point is before excessive displacements in the slope occur. Figure 4.4b also shows that the displacements, obtained after the first point of non-convergence, are equal to the displacements of the analyses with a criterion of 0.01. The initiation point of a rapid increase in displacements is also almost the same. From these observations it can be concluded that the analyses with a criterion of 0.001 are converging, but the maximum amount of iterations is too small to find equilibrium which satisfies the convergence criterion. This statement is verified with a model containing Q8 elements and a mesh size of 1 m. The analysis did not converge in 1000 iterations for a strength reduction factor of 1.325. The corresponding maximum vertical displacement is 0.0246 m. Then the maximum amount of iterations is set to 10000. Now the analysis did converge in 6109 iterations and the corresponding maximum vertical displacement is 0.0245 m.

Then there is another situation observed during the study of the effect of Poisson ratio on the FOS. The analysis is done with Q4 elements, a Poisson ratio of 0.4, a mesh size of 0.5 m and a convergence criterion of 0.01. The results are shown in Figure 4.5. A rapid increase of displacements occurred for a strength reduction

[1] The analyses with a convergence criterion of 0.01 did converge until excessive displacements occurred.

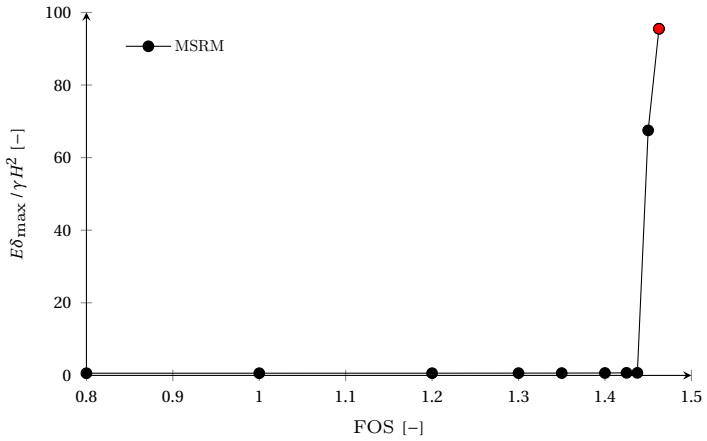

Figure 4.5: The red dot is corresponding to non-convergence of the analysis. The results are generated with Q4 elements, a Poisson ratio of 0.4, a mesh size of 0.5 m and a convergence criterion of 0.01.

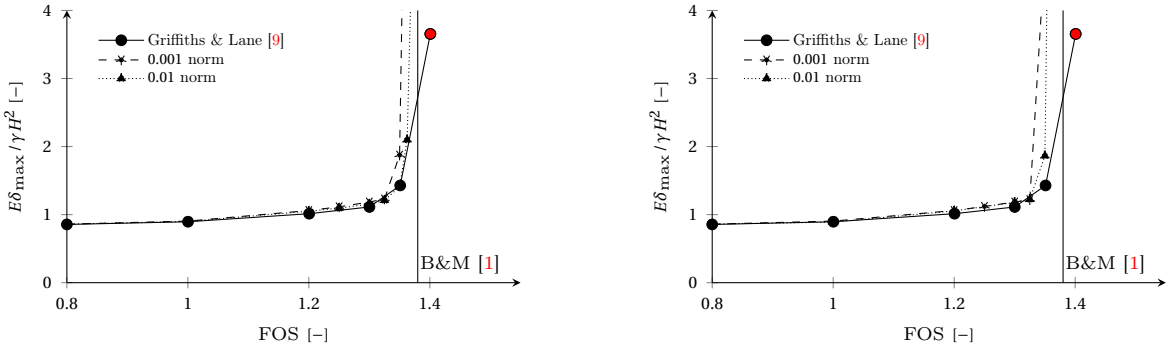

(a) Mesh size h = 1 [m].

(b) Mesh size h = 0.5 [m].

Figure 4.6: FOS versus dimensionless displacement for different convergence norms. The FOS is computed with the MSRM and Q8 elements. The rapid increase in displacements indicates slope failure. The results of Griffiths and Lane [9] are plotted as is the FOS computed by Bishop and Morgenstern [1] indicated by B&M. The FOS of Griffiths and Lane is 1.4 and the FOS of Bishop and Morgenstern is 1.380.

factor of 1.45, however the model **converged** in 790 iterations. Only for the next strength reduction factor of 1.4625, non-convergence did occur (indicated by the red dot).

In Figure 4.6, the results of Griffiths and Lane [9] and Bishop and Morgenstern [1] are added. Bishop and Morgenstern [1] provide a document with a chart containing the FOS of the concerning slope. The value of this FOS is 1.380 and is computed with a limit equilibrium method. Griffiths and Lane computed a FOS of 1.4 and it can be observed that excessive displacements coincide with non-convergence (indicated by the red dot). However, Griffiths and Lane [9] searched for non-convergence with relatively large increments of the FOS of 0.05. In this work, non-convergence is found with a 0.0125 precision of the FOS. Due to this relatively large jump in FOS, non-convergence coincides with excessive displacements and this also results in a larger FOS than the FOS obtained by Bishop and Morgenstern and obtained in this work.

It can be concluded that the assumption of Griffiths and Lane [9] for slope failure only holds for a certain combination of convergence criterion, maximum number of iterations mesh size and increment of the strength reduction factor.

In the end a convergence study is done for the various mesh sizes and convergence criteria, presented in displacement versus FOS plots. The results are shown in Figure 4.7 and 4.8. It was observed that non-convergence in general coincides with excessive displacements for a convergence criterion of 0.01. A maximum of 1000 iterations is far too small to find equilibrium for a convergence criteria of 0.001. However, as explained earlier

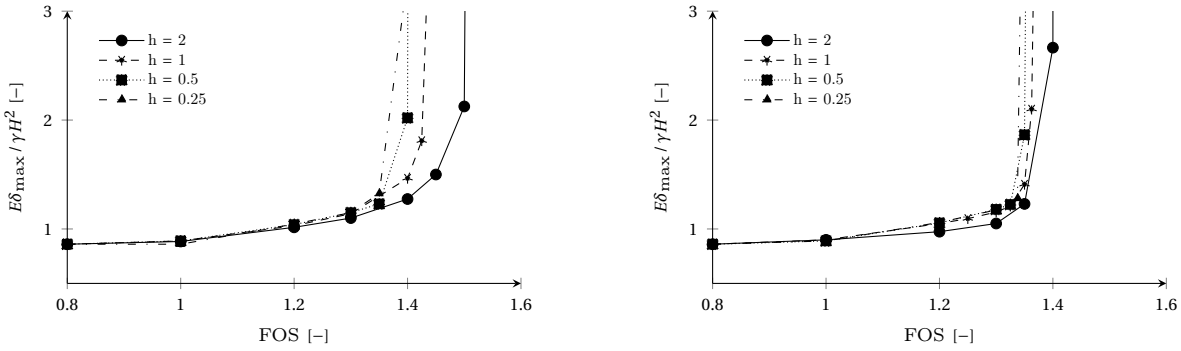

(a) Q4 elements.

(b) Q8 elements

Figure 4.7: Displacement versus FOS for various mesh sizes of Q4 and Q8 elements. A convergence criterion of 0.01 is used.

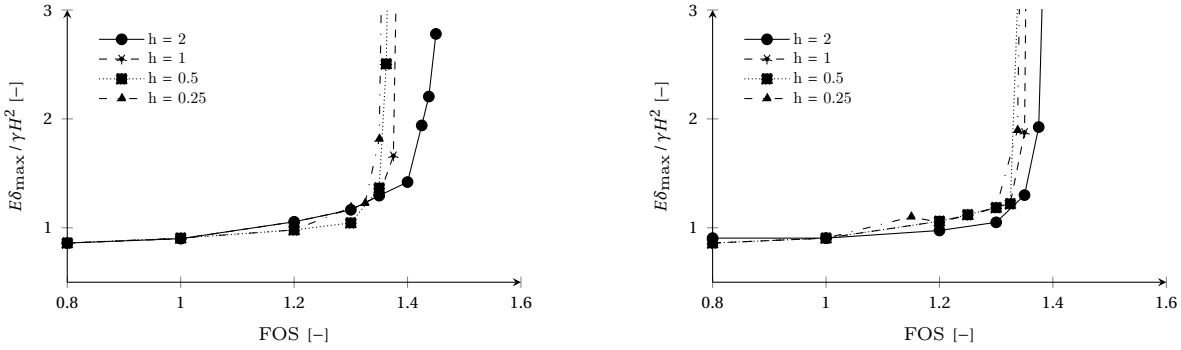

(a) Q4 elements.

(b) Q8 elements

Figure 4.8: Displacement versus FOS for various mesh sizes of Q4 and Q8 elements. A convergence criterion of 0.001 is used.

the displacement versus FOS plots give a good indication of the critical FOS. Table 4.3 gives another overview of the FOSs, but now the FOSs are computed at the moment when excessive displacements occur. Figure 4.9 shows the corresponding convergence plots. Now the FOS seems to converge also for a convergence criterion of 0.001. For both criteria, the FOS computed with the MSRM is 1.35 for the Q8 elements. Since Q8 elements converge faster to the true solution than Q4 elements, this value will be the benchmark representing strength reduction methods for this FE-model.

On the other hand there is the average FOS of the SSM with a value of 1.4 and the FOS obtained by Bishop and Morgenstern [1] of 1.38. Now lets say that the PM is tested and the FOS is between 1.35 and 1.4, then it can be concluded that the point of global failure computed with the PM is correct. If the FOS is just outside this domain, for example 1.34 or 1.41, it can be reconsidered whether this is acceptable or not. The FOS of the PM is probably not correct, if the FOS is far outside this domain.

4.3. Conclusions

In this section, the effect of the Poisson ratio on the FOS is studied. A value of 0.2, 0.3 and 0.4 for the Poisson ratio is used. The study is done with the SSM, MSRM and SRM and the results are in the form of a dimensionless maximum vertical displacement versus FOS plots. The characteristics of the displacements in the graphs can be

CC	MS	FOS			
		SSM		MSRM	
		Q4	Q8	Q4	Q8
0.01	2	-	1.38	1.55	1.4125
	1	1.4	1.39	1.45	1.375
	0.5	1.39	1.39	1.425	1.3625
	0.25	1.41	1.39	1.4125	1.35
0.001	2	-	1.4	1.45	1.4
	1	1.41	1.4	1.3875	1.375
	0.5	1.4	1.4	1.375	1.3625
	0.25	1.4	1.4	1.3625	1.35

Table 4.3: FOS for different mesh sizes (MS) and different convergence criteria (CC). The FOS is computed with the SSM and the MSRM. The FOS is obtained at the moment when excessive displacements occur.

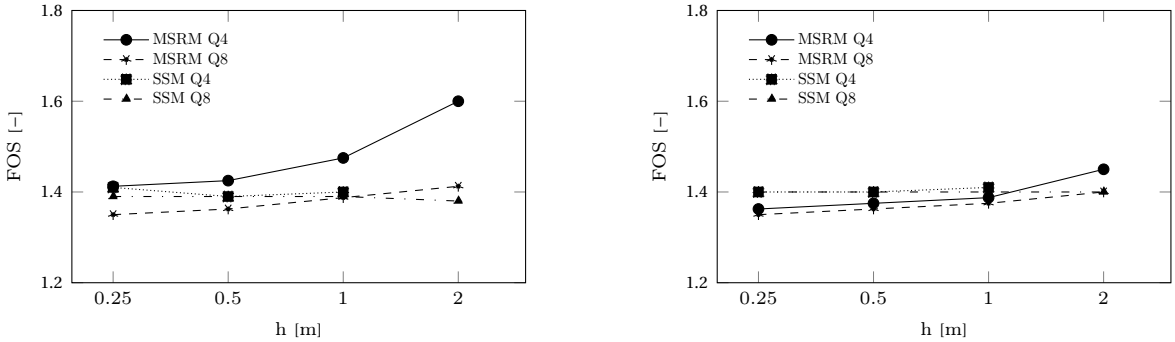

(a) Convergence criteria of 0.01

(b) Convergence criteria of 0.001

Figure 4.9: FOS versus mesh size h for Q4 and Q8 elements. The FOS is obtained when excessive displacements occur. A log scale is used for the horizontal axis.

used for verification of the PM. If the PM is tested, the same FE-model and analysis properties should be used. Then the PM is run with the three Poisson ratios and the following characteristics should be observed.

- If the Poisson ratio becomes larger, the maximum vertical displacements become smaller. This holds for an arbitrary strength reduction factor.
- In general, the FOS is the same for a Poisson ratio of 0.2 and 0.3. This holds for the SRM and the MSRM.
- A Poisson ratio of 0.4 results in the largest FOS. This holds for analyses with the SRM and the MSRM.
- Failure of the slope is more abrupt if the Poisson ratio increases.

The results of the SSM do not provide very useful information, because only the final FOS is computed and the value is approximately the same for every SSM analysis. The value of the FOS for a Poisson ratio of 0.3 is 1.39, which is smaller than the FOS obtained by a Poisson ratio of 0.2 and 0.4, which is 1.41. This is contradictory to the results of the SRM and the MSRM.

Next, a convergence study is performed with the MSRM and the SSM in order to obtain a reliable FOS which can be used as a benchmark. The study is done with four different mesh sizes of 0.25 m, 0.5 m, 1 m and 2 m and two convergence criteria of 0.01 and 0.001 are used. After the study the following conclusions can be made

- A ceiling of 1000 iterations does not always result in a non-convergence of the model which coincides with excessive maximum vertical displacements in the mesh. This holds for small mesh sizes of 0.5 m and 0.25 m and a convergence criterion of 0.001.
- Non-convergence can also occur after initiation of excessive vertical displacements. However, this is only observed in two analyses, both containing Q4 elements. One analysis with a mesh size of 2 m and a Poisson

ratio of 0.3. The other analysis with a mesh size of 0.5 m and a Poisson ratio of 0.4. Both analyses used a convergence criterion of 0.01.

- The FOS converges to a value of 1.35 for the MSRM.
- The FOS, computed with the SSM, is very robust since the values are almost always equal for every mesh size. The average FOS of the SSM is 1.39 for a convergence criterion of 0.01 and the maximum deviation is 0.1. The average FOS is 1.40 for a convergence criterion of 0.001 and the maximum deviation is 0.1.

Based on these conclusions, the following recommendations are given.

- If a convergence criterion of 0.001 is used in combination with a mesh size of 0.5 or smaller, the maximum amount of iterations should be significantly increased (probably more than 10 times). Therefore it is advised to use a convergence criterion of 0.01 if mesh sizes of 0.5 m or smaller are used.
- The FOS should be determined based on initiation of an excessive increase in maximum vertical displacements, rather than on non-convergence of the model.
- The resulting FOS should be between 1.35 and 1.4 if the concerning FE-model is tested with the PM. This range is based on the converged values of the FOS from the MSRM and on the maximum FOS obtained by the SSM. If the FOS is outside this range, some revisiting of the implementation may be needed.

5

Benchmarks generated with analyses based on load increments

In this chapter, analyses are run with the SLIM and the MLIM in order to obtain results which can be used for verification of the CSN computed with the PM. The FE-model is given in Figure 3.6, which is based on the model of Manzari and Nour [17]. First, a study is performed of the effect of the dilatancy angle on the stability of a slope. The characteristics of the results can be used for verification of the PM. Then a convergence study is done to obtain a reliable CSN. The results of Manzari and Nour serve as reference.

Then, results are given for FE-models containing interface elements. These results are used in Chapter 6 for verification of a development version of the PM.

5.1. Effect of the dilatancy angle on the CSN

The soil and model properties are given in Chapter 3.2. The friction angle is kept at a constant value of 30° and values of 0°, 10°, 20° and 30° are taken for the dilatancy angle. A mesh size of 0.5 m is applied.

It is possible to only reduce the cohesion with the SRM in Diana FEA. Therefore, the model is also analysed with the SRM, which will result in a FOS which can be compared with the CSN of the SLIM and the MLIM. This provides additional numerical proof for the relation between methods based on strength reduction and methods

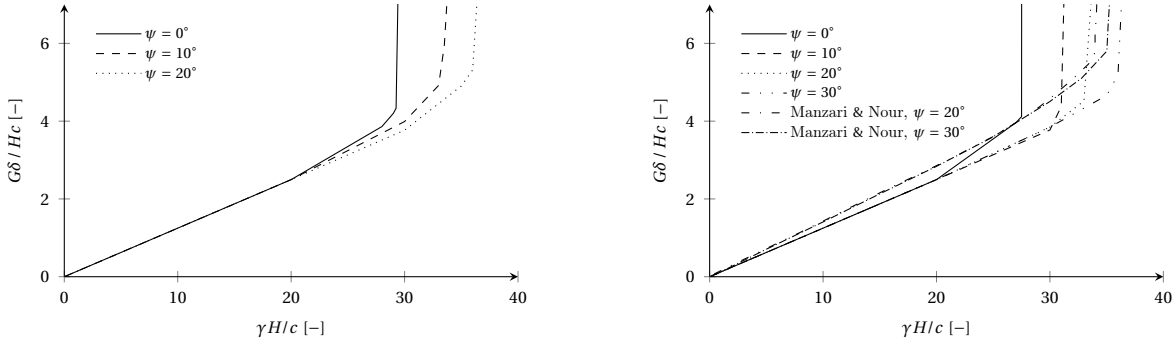

(a) Q4 elements.

(b) Q8 elements.

Figure 5.1: Influence of the dilatancy angle on the FOS. Stability of the slope is lost at initiation of excessive displacements. The analyses are run with the SLIM. Results are shown for Q4 elements (left figure) and for Q8 elements (right figure). The friction angle used is $\varphi = 30°$.

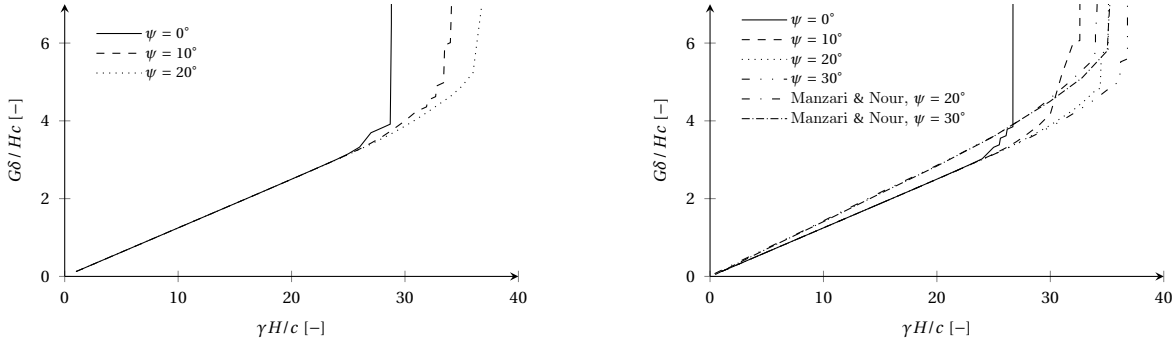

(a) Q4 elements.

(b) Q8 elements.

Figure 5.2: Influence of the dilatancy angle on the stability of the slope in the form of a dimensionless displacement plotted versus the SN. The displacements are the vertical displacements of the tip of the slope. The analyses are run with the MLIM. Initiation of a rapid increase in displacements indicates slope failure. The gravity is incremented with steps of 1000 N/m^3. Results are shown for Q4 elements (left figure) and for Q8 elements (right figure).

based on load increments, obtained in chapter 3.4. The value of the unit weight, γ, for the SRM is 1000 N/m^3, corresponding to a stability number (SN) of 1.

The normalised vertical displacement at the tip of the slope is computed with the SLIM and plotted versus the SN which is shown in Figure 5.1. The results of Manzari and Nour [17] are also shown in the figures. Figure 5.2 shows the same results for the analyses computed with the MLIM. An overview of the SN at failure of the slope is given in Table 5.1.

In Figure 5.1 it can clearly be seen that the CSN is increasing if the dilatancy angle is increasing. This holds for both Q4 and Q8 elements. From Table 5.1 it can be observed that the CSN of the Q4 elements is larger than the CSN of the Q8 elements. This is also observed in the previous chapter and is the result of the stiffer response of the Q4 elements. The results of Manzari and Nour differ from the results obtained in this work. The displacements they obtained in the phase before failure of the slope are larger. Most likely a smaller value for the Young's modulus is used, but the applied value is not given in their research. Although the Young's modulus has little influence on the FOS (and thus the CSN) [9], the difference in the Young's modulus could be the reason for the small difference in the CSN. Other reasons could be differences in loading steps, convergence criterion and in mesh size. These properties were also not given. Hence, the only valuable information from the paper of Manzari and Nour for this thesis is the conclusion that the CSN becomes larger if the dilatancy angle is increasing. The same is observed in the analyses of this work.

Figure 5.2 shows similar results for the MLIM. From Table 5.1 it can be observed that the CSNs are almost equal for every analysis method. This also holds for the SRM. The result of a SRM is the FOS and does not

ψ	element	SRM	SLIM	MLIM	M & N
0°	Q4	29.13	29.5	28.8	–
	Q8	27.06	27.75	26.8	–
10°	Q4	33.88	34	34.5	–
	Q8	31.88	32	32.6	–
20°	Q4	37.25	37.25	37.2	–
	Q8	35.55	35.75	35.8	34.12
30°	Q4	–	–	–	–
	Q8	36.75	36.75	36.9	35.25

Table 5.1: SN for different values of the dilatancy angle, ψ, at failure of the slope. The SN is given for the SRM, the models with 1 load step (SLIM), the models with multiple loading steps (MLIM) and of Manzari and Nour (M & N).

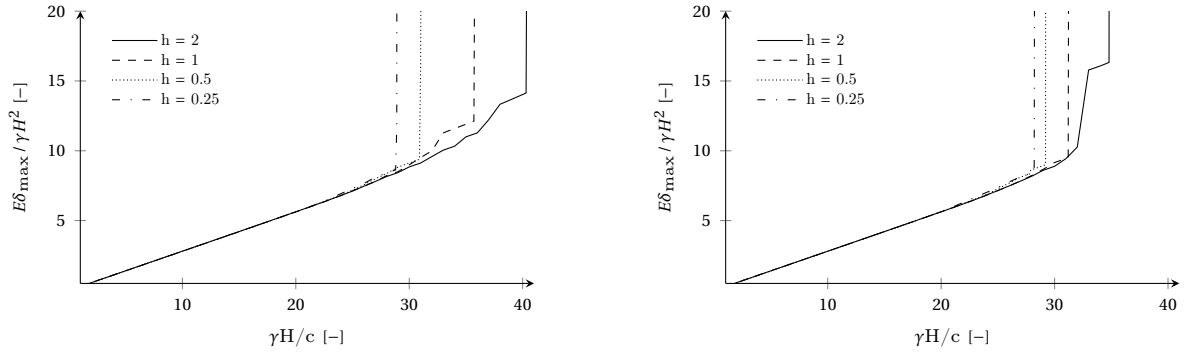

(a) Q4 elements.

(b) Q8 elements

Figure 5.3: Displacement versus CSN for various mesh sizes of Q4 and Q8 elements. A convergence criterion of 0.001 is used.

compute the CSN directly, since the cohesion is reduced during the SRM and the unit weight is not increased as in the SLIM and MLIM. However, as discussed in section 3.4, the combination of γ, H and c does not have any influence on the stability of a slope, as long as the (initial) quotient preserves the same value. This means that increasing γ with a certain factor has the same effect on the stability of the slope as reducing the cohesion with the same factor. Thus, lets say that the FOS obtained with the SRM of a slope has a value of 30. This means that the cohesion is reduced by a factor of 30 before the slope fails and the CSN of the SRM is also 30. Therefore, Table 5.1 provides a numerical proof for the relation between methods based on strength reduction and methods based on load increments. The largest absolute difference between the CSN of the methods is 0.95 and relatively this is 3.4%.

5.2. Convergence study

In this section a convergence study of the same FE-model is performed in order to obtain a reliable CSN. The only difference is that a foundation layer of $0.25H$ is added (see Figure 5.5 and 5.6). Four mesh sizes of 0.25 m, 0.5 m, 1 m and 2 m are applied in the analyses. The value of the convergence criterion is 0.001 with a maximum of 1000 iterations. This results in a rapid increase of displacements of the tip of the slope, coinciding with non-convergence for most of the analyses. For some analyses, non-convergence occurs after initiation of excessive displacements of the tip of the slope. In this case, the initiation of excessive displacements are used as indication for the CSN. The unit weight is increased with 1000 N/m^3 per load step. Just before failure, the increment is set to 100 N/m^3 in order to obtain a more accurate CSN. The following soil properties are used

$$\varphi = 30\,[^\circ], \quad \psi = 0\,[^\circ], \quad \gamma = 1000[\text{N/m}^3], \quad c = 10000\,[\text{N/m}^2], \quad E = 2\cdot 10^8\,[\text{N/m}^2], \quad \nu = 0.3\,[-] \tag{5.1}$$

The displacement versus SN plots for various mesh sizes is shown in Figure 5.3. An overview of the CSNs is shown in Table 5.2 and Figure 5.4 gives convergence plots of the CSN versus mesh size for the Q4 and Q8

MS	Q4	Q8
2	40.4	34.9
1	35.8	31.3
0.5	31.0	29.3
0.25	28.9	28.3

Table 5.2: CSN for different mesh sizes (MS). The CSN is computed with the MLIM and is obtained at the initiation of excessive displacement.

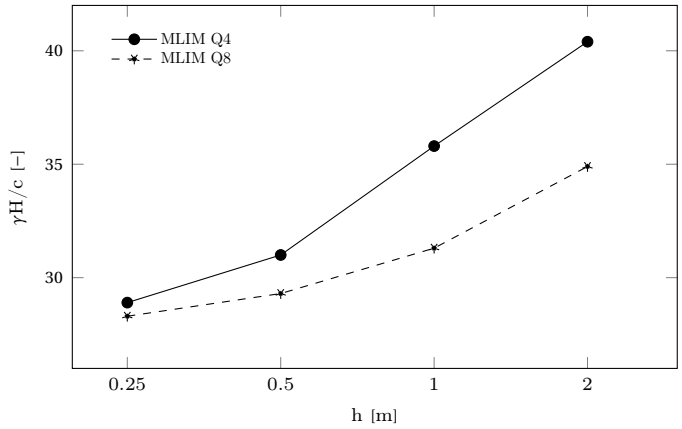

Figure 5.4: CSN versus mesh size h for Q4 and Q8 elements. The CSN is obtained when excessive displacements occur. A log scale is used for the horizontal axis.

elements. A log scale is used for the horizontal axis. It can be observed that there is a big difference in CSNs between the mesh sizes. The difference in CSN between a mesh size of 2 m and 0.25 m is 11.5 for Q4 elements and 6.6 for Q8 elements. It seems that the CSN converges to a value of 28, which can be seen from Table 5.2 and Figure 5.4. A mesh size of 0.25 m results in a CSN of 28.9 and 28.3 for Q4 elements and Q8 elements respectively.

Now the objective is to choose a reliable CSN from the values obtained in this study. Since the PM is still dependent on the mesh size [26] [20] it is not realistic to state that the CSN must be 28 when testing the PM. Instead of having a fixed value, the range $28 - 34$ is given as benchmark for testing the PM. The lower bound of 28 takes into account the convergence of the CSN. The upper bound is based on the standard deviation of the CSNs of Table 5.2, with 28 taken as the mean value. This range could be used as a guide-line if the PM is being tested with an arbitrary mesh size. However, the recommendation is to test the PM for the different mesh sizes and the resulting CSN should also converge to a value of 28.

5.3. Interface models with linear continuum elements

In this section, the FE-model in Figure 5.5 and 5.6 is analysed again [1]. Interface elements are used to model the critical slip surface. With these interface elements it is possible to compute strong discontinuities. The development version of the PM is restricted to a pre-defined slip surface, just like a model with interface elements. Thus both the development version of the PM and a model with interface elements have to pre-define a slip surface in the model and both methods can reproduce a jump in the displacement field. Therefore it is expected that the results of the development version of the PM are very close to the results of the model with interface elements.

[1] The foundation layer of $2.5H = 2.5$ m was added to the FE-model in Figure 3.6 to prevent some issues with the development version of the PM due to the boundary conditions. More information about this issue is given in Chapter 6

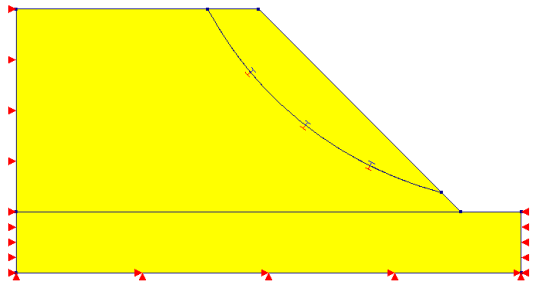

Figure 5.5: FE-model of a slope with interface elements at the location of a slip surface. The location of this slip surface is computed with a load increment method.

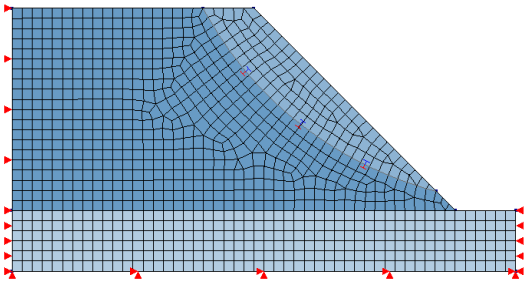

Figure 5.6: Mesh of the FE-model of a slope with interface elements at the location of a slip surface.

element	γ [N/m^3]	E [N/m^2]	ν [–]	c [N/m^2]	φ [°]	ψ [°]
Q4/Q8	1000	$2 \cdot 10^8$	0.3	-	-	-
Interface	1000	$2 \cdot 10^8$	0.3	10000	30	0

Table 5.3: Material properties of the linear continuum elements and the interface elements.

MS	d_n [N/m^3]	d_s [N/m^3]
2	$0.5 \cdot 10^{11}$	$0.5 \cdot 10^8$
1	$1 \cdot 10^{11}$	$1 \cdot 10^8$
0.5	$2 \cdot 10^{11}$	$2 \cdot 10^8$
0.25	$4 \cdot 10^{11}$	$4 \cdot 10^8$

Table 5.4: Shear moduli used for the different mesh sizes in the analyses with interface elements.

Hence, the results of the FE-model in this section are used in Chapter 6 to verify the results of the development version of the PM. The computations are done with linear continuum elements, since the objective is to verify the behaviour of the enrichment elements.

The FE-model is shown in Figures 5.5 and 5.6 and the material properties of the continuum and interface elements are given in Table 5.3 and 5.4. Table 5.4 gives the shear moduli used for the various mesh sizes. These shear moduli are the linear interface properties. The analyses are done with the MLIM and it may be noted that the initial value of the SN is 1. Just as in the previous section, four different mesh sizes of 0.25 m, 0.5 m, 1 m and 2 m are used to obtain a reliable CSN. A convergence criterion of 0.001 is used with a maximum of 1000 iterations.

The interface elements obey a Mohr-Coulomb friction law. Figure 5.5 shows the slip surface along which the interface elements are modeled. The location of this slip surface is computed with a load increment method in order to obtain a realistic slip surface for the model with interface elements. First, an analysis is done with the MLIM on a model without interface elements. Then the location of the critical slip surface is approximated by a curve through the resulting shear band of this analysis. The word approximation is used, because the critical slip surface is somewhere in the shear band, which has a finite width in a model consisting of only continuum elements. The interface elements are modeled along the coordinates of this slip surface. The approximation of the critical slip surface (for the location of the interface elements) results in a more realistic FE-model, but is not necessary in the process for verification of the enrichment elements of the PM. However, as will be explained later, it is very critical to use exactly the same pre-defined slip surface in the verification process.

The failure mode of the slope is shown in Figure 5.7 and the colours indicate the displacement norm. The figure gives an impression of the strong discontinuity in the displacement field. Figure 5.8 shows that the Mohr-Coulomb shear capacity is reached in every point in the slip surface. This capacity is stress based and the values indicate how far the stress state in the interface elements is from the critical Mohr-Coulomb stress. A value of 1 means that the critical stress is reached in an interface element and no more capacity is left. A value of 0 means that a capacity of 100% is left. Global failure of the slope occurs if the shear capacity is reached in all interface elements, as shown in Figure 5.8.

The dimensionless vertical displacement of the tip of the slope is plotted versus the SN for the different mesh sizes and shown in Figure 5.9. An overview of the CSNs of the different analyses is given in Table 5.5. From

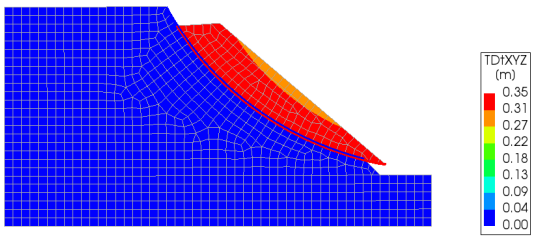

Figure 5.7: Failure mode of the Q8 FE model computed with the SLIM. The colours represent the displacement norm.

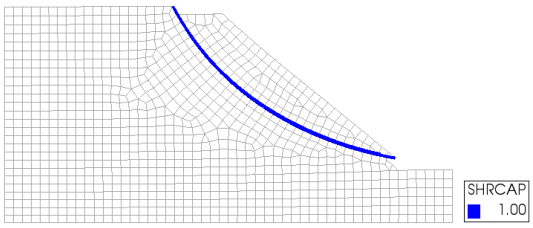

Figure 5.8: Mohr-Coulomb shear capacity in the interface elements.

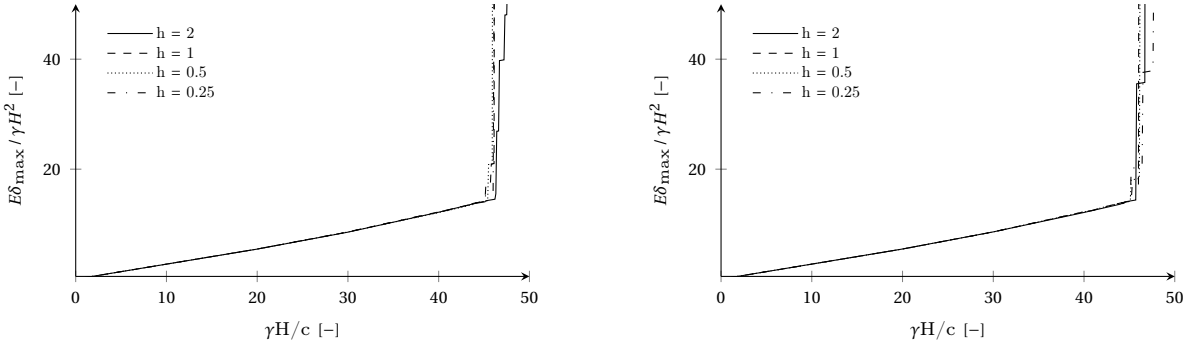

(a) Q4 elements.

(b) Q8 elements

Figure 5.9: Displacement versus CSN for various mesh sizes of Q4 and Q8 elements. A convergence criterion of 0.001 is used.

Figure 5.9a and 5.9b it can be observed that the CSNs are almost equal for all mesh sizes and the analyses with Q4 and Q8 elements. The moment when the full shear capacity in the interface elements is reached is coinciding with the initiation of excessive displacements, *i.e.*, at the kinks in the plots of Figure 5.9. Non-convergence of the analysis happens far beyond the point of a fully reached shear capacity in all analyses and therefore non-convergence is not a good indication for global failure of the slope. From Table 5.5 it can be observed that the CSN is 45.2 for almost every analysis. Therefore, a value of 45.2 will serve as a benchmark when testing the development version of the PM.

It may be noted that there is a big difference in the CSN between models consisting of only continuum elements (Table 5.2) and models containing interface elements (Table 5.5). It seems that the CSNs of the model consisting of interface elements and linear continuum elements is much larger than the model without interface elements. The reason for this gap is the difference between the material models of the continuum elements. The continuum elements in the model with interface elements behave only elastically. Therefore, the continuum elements in the interface model cannot fail according to Mohr-Coulomb plasticity and there will be no redistribution of stresses in the continuum elements. Hence, the failure of the slope is only dependent on the stresses in the interface elements. The load needs to be larger for all interface elements to fail, since there is no local failure in surrounding continuum elements.

The last item to be discussed about the model with interface elements, is the high sensitivity of the CSN to a small change in the geometry of the slip surface. Figure 5.10 shows two slip surfaces. The blue slip surface is the slip surface from the model in Figure 5.5 and resulted in a CSN of 45.2. Now, analyses are run with interface elements along the red slip surface. This is done for a model with Q8 elements and a mesh size of 0.25 m and 0.5 m. The resulting CSNs are 40.1 for both analyses and this means that the absolute difference in the CSN is 5.1 for the red and blue slip surface. Since a small difference in the geometry has such a large impact on the CSN, it is very important to use exactly the same slip surface in the process of testing and verifying the development version of the PM.

MS	Q4	Q8
2	45.2	44.5
1	45.2	45.3
0.5	45.5	45.2
0.25	45.2	45.2

Table 5.5: CSN for different mesh sizes (MS) computed with the MLIM for a model consisting of linear continuum elements and interface elements. The CSN is obtained when the Mohr-Coulomb shear capacity is reached in all interface elements.

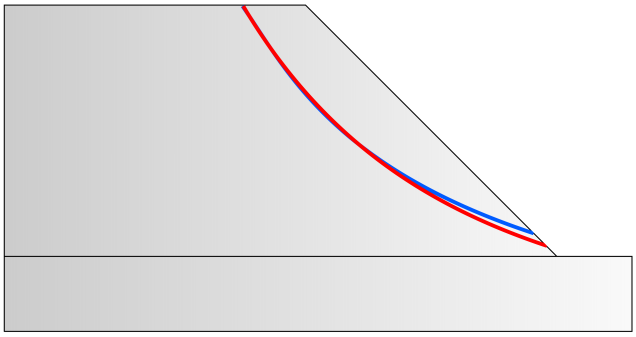

Figure 5.10: Location of two slip surfaces for the model with interface elements. The blue curve is the slip surface of Figure 5.5 and the red curve is the position of a second slip surface.

5.4. Conclusions

In this section, the CSN of a FE-model is computed with an analysis based on load increments. This CSN is equivalent to a FOS of a SRM with a reduction of only the cohesion. First, the effect of the dilatancy angle on the CSN is studied with the MLIM, SLIM and the SRM with only a reduction of the cohesion. The results are plotted in displacement versus SN plots and the characteristics of those plots can be used for verification of the PM.

Then a convergence study is done with the MLIM in order to obtain a reliable CSN. This CSN can be used for verification of the CSN computed with the PM.

Finally, a convergence study is performed of the CSN of a FE-model containing interface elements. The interface elements represent the slip surface and the results of this study are used in the next chapter for verification of the development version of the PM. The following conclusions are made based on those studies.

- First, it can be concluded that the CSN is increased if the dilatancy angle is increased. The largest observed relative difference is 16.52% for an increase of the dilatancy angle of 10°.
- The CSN is almost equal for the SRM, the SLIM and the MLIM in the study of the effect of the dilatancy angle. Therefore, it is recommended to use the MLIM in similar analyses, since those analyses are less computationally expensive and less time consuming.
- If the PM is tested on the FE-model of this chapter, then the resulting CSN should converge to a value of 28 when the mesh size is reduced.
- The convergence study of the CSN of the model with interface elements results in a robust CSN of 45.2. This value is obtained when the shear capacity in all interface elements is reached. Hence, the value of 45.2 serves as a benchmark when testing the development version of the PM.
- A small change in the geometry of the pre-defined slip surface in the model with interface elements has a large impact on the value of the CSN. Therefore it is important to use exactly the same slip surface when verifying the development version of the PM with the results of a model containing interface elements.

6

Verification of the propagation method

In this chapter, onset of localisation is verified numerically and analytically on element level. Then the FE-model of Chapter 5.3 is analysed with the development version of the PM. The objective is to verify if the behaviour of the enrichment elements in a FE-model of a slope is correct. This is done by computing the point of global failure of the slope, which is represented by the CSN. Global failure occurs when the shear capacity is reached in all enrichment elements. The corresponding CSN is then compared with the CSN of the model with interface elements from the previous chapter, which serves as a benchmark. The enrichment elements work properly if the CSN is close to the value of the benchmark.

6.1. Verification of onset of localisation

The objective of this section is to verify onset of localisation. This means that onset of localisation must occur in the appropriate load step and that the correct direction of the localisation plane is obtained. First, the FE plane strain model which is used to obtain the angle of the vector normal to the localisation plane is given. Then, the numerical results are given and discussed, followed by verification of localisation with numerical results and with analytical equations. Three analytical expressions are used for verification of the results. Two are from the paper of Runesson *et al.* [14] and one is from the paper of Rudnicki and Rice [13]. The results of the three expressions are compared with each other, to make sure that the expressions are used correctly.

6.1.1. Finite element model

A non-linear FE analysis of a single quadrilateral (Q4) element is executed. The purpose of this model is to compute the determinant of the acoustic tensor in every load increment and to monitor when this determinant becomes zero. When the determinant becomes zero, the possible directions of the vector normal to the localisation plain are obtained (see Chapter 1.4). For 2D FE-models, two directions of the normal vector are obtained, which are orthogonal. Sanborn and Prévost [26] choose the direction of the maximum displacement gradient for the direction of the normal vector, *i.e.*, the normal vector is chosen which is closest to the direction of the maximum displacement gradient. A computation of this maximum displacement gradient is not included in this work. The model is shown in Figure 6.1. The width and height of the element are 1 meter. Translation in x-direction is constrained for the left edge and bottom edge is constrained in y-direction. The Young's modulus is $E = 2.0 \times 10^8$ N/m^2 and the Poisson ratio is $\nu = 0.2$.

The analysis is run with a full Newton-Raphson scheme. Displacement control is applied on node 3 and 4. A displacement of 4×10^{-4} meter is applied per load increment on these nodes. The model obeys the following Drucker-Prager yield criterion

$$F(\boldsymbol{\sigma}) \leq \sqrt{3J_2} + \alpha p - \beta c = 0 \tag{6.1}$$

with J_2 the second invariant of the deviatoric Cauchy stress tensor $\boldsymbol{\sigma}$, with $p = \frac{1}{3}\sigma_{ii}$, the hydraustatic stress and c is the cohesion. The expressions for α and β are

$$\alpha = \frac{6\sin\varphi}{3-\sin\varphi}, \qquad \beta = \frac{6\cos\varphi}{3-\sin\varphi} \tag{6.2}$$

where φ is the friction angle. The plastic potential takes the following form

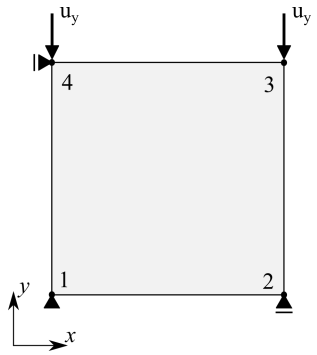

Figure 6.1: Plane strain model with single Q4 element.

$$G(\boldsymbol{\sigma}) = \sqrt{3J_2} + \gamma p \tag{6.3}$$

where the term γ can be expressed as

$$\gamma = \frac{6\sin\psi}{3-\sin\psi} \tag{6.4}$$

With ψ the dilatancy angle. The analysis is run with four different combinations of φ and ψ, which are given in Table 6.1.

Leroy and Ortiz [29] proposed an analytical solution for computing the determinant of the acoustic tensor for 2D cases, which is used to compute the determinants. The determinant can be computed explicitly by solving the following quartic equation [29]

$$\det(\boldsymbol{A}) = a_0 n_1^4 + a_1 n_1^3 n_2 + a_2 n_1^2 n_2^2 + a3 n_1 n_2^3 + a_4 n_2^4 \tag{6.5}$$

where $n_1 = \cos(\theta)$ and $n_2 = \sin(\theta)$, which are the two components of the normal vector $\boldsymbol{n}_S$. The angle θ is relative to the largest principal stress where $\sigma_1 <= \sigma_2 <= \sigma_3$ and σ_1 the largest compressive stress. The coefficients a_i are computed from components of the material tangent stiffness modulus $\boldsymbol{D}$ as

$$\begin{aligned}
a_0 &= D_{1111}D_{1212} - D_{1112}D_{1211} \\
a_1 &= D_{1111}D_{1222} + D_{1111}D_{2212} - D_{1112}D_{2211} - D_{1122}D_{1211} \\
a_2 &= D_{1111}D_{2222} + D_{1112}D_{1222} + D_{1211}D_{2212} - D_{1122}D_{1212} - D_{1122}D_{2211} - D_{1212}D_{2211} \\
a_3 &= D_{1112}D_{2222} + D_{1211}D_{2222} - D_{1122}D_{2212} - D_{1222}D_{2211} \\
a_4 &= D_{1212}D_{2222} - D_{2212}D_{1222}
\end{aligned} \tag{6.6}$$

With these formulas, the determinant is computed in every load increment for different angles of θ, from -90 to 90 degrees, by means of a loop. The angle is incremented with 1 degree. A pseudo code for computation of the localisation angle is shown in Algorithm 1. This algorithm is run in every load increment (when equilibrium is found) in a loop over the integration points and when plastic loading is detected in the concerning integration point.

6.1.2. Numerical results

In this section, the results are represented by three plot types, shown in Figure 6.2, 6.3 and 6.4. Two graphs are shown in each figure. The graphs on the left represent the results obtained in this work and the graphs on the

model	1	2	3	4
φ	20°	20°	25°	30°
ψ	0°	20°	0°	0°

Table 6.1: Combinations of φ and ψ for the FE analysis.

Algorithm 1 Algorithm localisation angle

$a_i \leftarrow \boldsymbol{D}$ ▷ compute a_i from components $\boldsymbol{D}$
for $\theta \leftarrow -90$ to 90 **do** ▷ loop over localisation angles
    $\mathrm{n}_1 \leftarrow \cos(\theta)$ ▷ compute normal vector components
    $\mathrm{n}_2 \leftarrow \sin(\theta)$
    $\det(\boldsymbol{A}) = a_0 n_1^4 + a_1 n_1^3 n_2 + a_2 n_1^2 n_2^2 + a3 n_1 n_2^3 + a_4 n_2^4$
    if $\det(\boldsymbol{A}) \leq 0$ **then**
        $\boldsymbol{n} \leftarrow \cos(\theta), \sin(\theta)$ ▷ compute localisation angle
    end if
end for

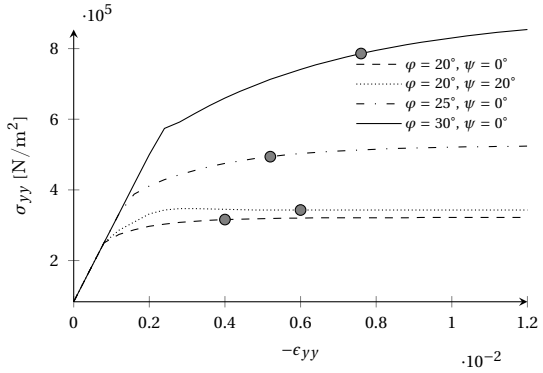

(a) Results of the analysis with the plane strain Q4 element and perfect plasticity model.

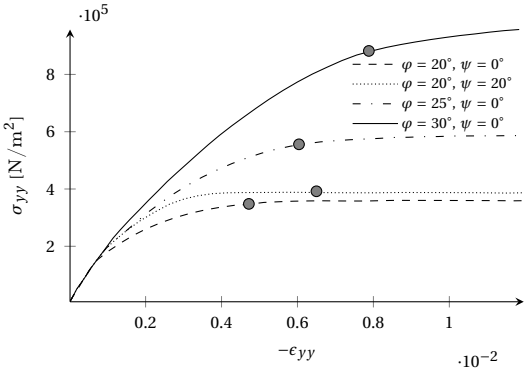

(b) Results of Leroy and Ortiz [29].

Figure 6.2: Stress-strain diagram of the Q4-element in compression for various values of φ and ψ. Onset of localisation is indicated by the grey dots.

right are from the research of Leroy and Ortiz [29] [1], which are used for verification of the numerical results of this work. The original figures of Leroy and Ortiz can be found in Appendix C.

The stress-strain diagram in the y-direction is given in Figure 6.2 for various combinations of the friction angle φ and dilantancy angle ψ. The difference between elastic and plastic loading is clearly visible in Figure 6.2a. The values of the determinant of the acoustic tensor is plotted versus the localisation angle theta and is shown in Figure 6.3 for load step 1, 5 and 10 and a friction angle $\varphi = 20°$ and a dilatancy angle $\psi = 0°$. The values of the determinants are normalised with the value of the determinant of the elastic acoustic tensor, which is the acoustic tensor during elastic loading. The value of the determinant reaches a value below zero for the first time in load step 10, for which the strain attains a value of $\epsilon = 0.004$. Figure 6.4 shows the evolution of the minima of the determinant during loading for various values of φ and ψ. In the elastic stage, the normalised value attains a value of 1.

The stress-strain diagrams in Figure 6.2a and 6.2b show similar results. The points of onset of localisation are marked with a grey dot and are approximately the same for both figures. Also, both figures show about the same loading pattern, except for the elastic loading branch. The difference between elastic and plastic loading is clearly visible in Figure 6.2a while Figure 6.2b shows a smooth transition. This smooth transition is due to the friction hardening Leroy and Ortiz [29] applied, which is a function of equivalent plastic strain. The definition of the hardening parameter of the friction angle is described in a model from de Borst [4], which is defined such that a smooth transition between elastic and plastic loading takes place and such that plastic loading starts at the same loading point. At a critical value of the plastic strain, $\bar{\epsilon}_c^p$, the friction angle attains its maximum value, φ_f. These maximum values of the friction angle, shown in Figure C.1, are the same as the values of the friction angle used in the model of section 6.1.1.

The yield function of equation 6.1, used for the FE-model in section 6.1.1, does not contain friction hardening and the values of the friction angle are fixed. Therefore, the difference between elastic loading and plastic loading

[1] The results of Leroy and Ortiz are extracted with WebPlotDigitizer.

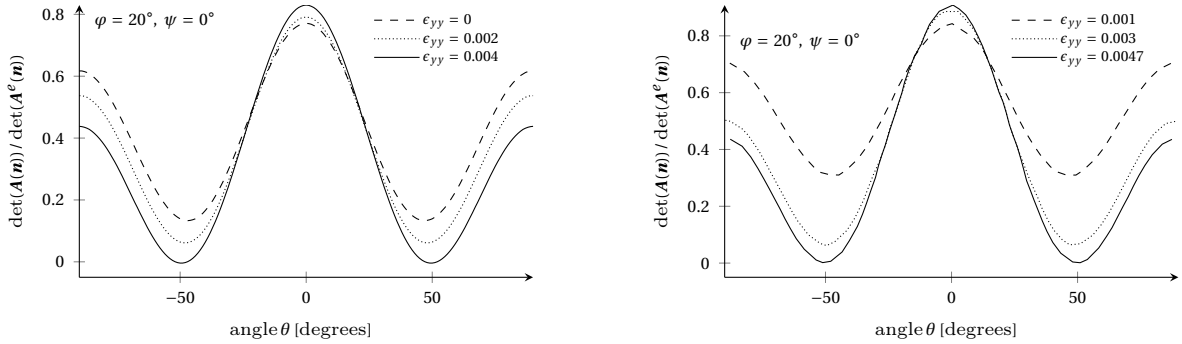

(a) Results of the analysis with the plane strain Q4 element.

(b) Results of Leroy and Ortiz [29].

Figure 6.3: Evolution of the determinant of the acoustic tensor $\boldsymbol{A}(\boldsymbol{n})$ during loading, up to onset of localization.

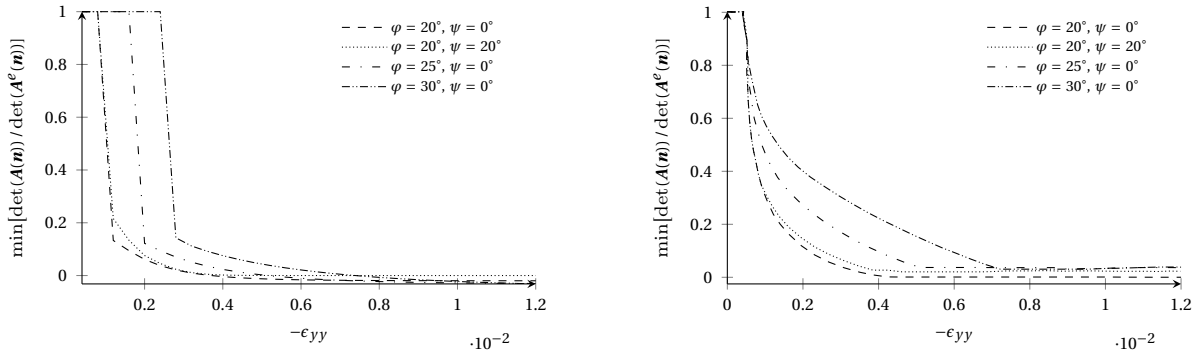

(a) Results of the analysis with the plane strain Q4 element.

(b) Results of Leroy and Ortiz [29].

Figure 6.4: Evolution of the minima of the determinant during loading.

is visible in Figure 6.2a. Also, yielding does occur at different loading points, because the yield functions are dependent on the values of φ. The strains at the localisation points are larger in Figure 6.2a than in Figure 6.2b, which is also the result of the difference in the definition of the friction angle.

Looking at the evolution of the determinant of the acoustic tensor $\boldsymbol{A}$ in Figure 6.3, it can be noticed that both models show similar results. In the FE analysis with $\varphi = 20°$ and $\psi = 0°$ (Figure 6.3a), the determinant of the acoustic tensor reaches a value just below zero corresponding to a localisation angle of 50°. This is the same result as is obtained by Leroy and Ortiz (Figure 6.3b). Results of the localisation angle for all combinations of φ and ψ are given in Table 6.2, together with the results of Leroy and Ortiz. The table shows similar outcomes for all FE-analyses. Only a small difference can be observed for load case 3 and 4. A plausible reason for this difference is that Leroy and Ortiz used smaller angle increments of 0.5°. Figure 6.4 shows the evolution of the minima of the determinants during compressive loading and the results of the two graphs in this figure are also similar. The difference in smoothness is caused by the difference in the definition of the friction angle as is described earlier. The normalised minima of the determinants adopt a value of 1 during elastic loading.

model	φ	ψ	FE-model	Leroy & Ortiz
1	20°	0°	50°	50°
2	20°	20°	59°	59°
3	25°	0°	51°	51.5°
4	30°	0°	52°	53°

Table 6.2: Angle of the vector normal to the localisation plane, with respect to the first principal stress.

6.1.3. Analytical solutions

There are several papers in which the direction of the vector normal to the localisation surface is derived analytically as is the critical value of the corresponding plastic modulus, H^{cr}. Those solutions are derived from the requirement of the determinant of the acoustic tensor (see Chapter 1.4).

Rudnicki and Rice [13] give analytical solutions for 2D stress situations, but the Drucker-Prager yield function used, is different from the one used in Diana FEA. Ottosen and Runesson [18] give more general solutions for 3D stress cases and for more yield criteria. Runesson *et al.* [14] give analytical solutions, explicitly for plane stress and plane strain situations. In the latter, the same Drucker-Prager yield criteria is used as in the software of Diana FEA and therefore this work is used for further verification of the numerical results. Runesson *et al.* [14] derived analytical solutions for the direction of localisation and for H^{cr} with use of spectral properties of the acoustic tensor. First, the expressions of the localisation angle and H^{cr} are given and subsequently it will be explained how to used those expressions. For plane strain models, the general expression for the angle of the normal vector is given as

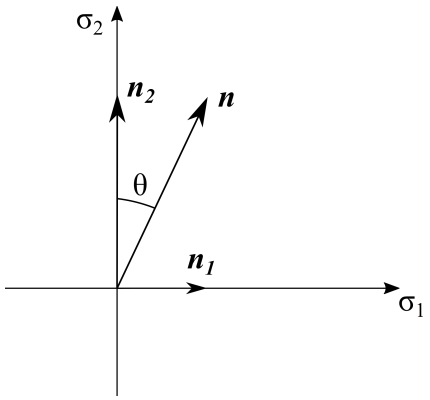

Figure 6.5: Orientation of the normal vector $\boldsymbol{n}$.

$$\tan^2\theta = \frac{n_1^2}{n_2^2} = -\frac{c_1}{c_2} \tag{6.7}$$

This equation holds for the case $f_1 > f_2$, $g_1 > g_2$, with f_i and g_i the principal components of the gradient of the yield function and the gradient of the plastic potential respectively as given as in equation 1.6. Orientation of the vector components is given in Figure 6.5. This case is valid for the loading conditions of the model in section 6.1.1. Furthermore, the components c_1 and c_2 are given as

$$\begin{aligned} c_1 &= f_1(g_1 - g_2) + g_1(f_1 - f_2) + \nu h \geq 0 \\ c_2 &= f_2(g_1 - g_2) + g_2(f_1 - f_2) + \nu h \leq 0 \end{aligned} \tag{6.8}$$

with ν the Poisson ratio. For h, the following expression holds

$$h = f_3(g_1 - g_2) + g_3(f_1 - f_2) \tag{6.9}$$

For the same loading conditions, Runesson *et al.* derived a general expression for the critical plastic modulus as

$$\frac{H^{cr}}{2G} = \frac{(f_1 g_2 - f_2 g_1)^2 + \nu^2 h^2 + 2\nu(f_1 g_2 - f_2 g_1)(g_3(f_1 - f_2) - f_3(g_1 - g_2))}{4(1-\nu)(f_1 - f_2)(g_1 - g_2)} - \frac{f_3 g_3}{1-\nu} \tag{6.10}$$

where G is the shear modulus. Runesson *et al.* also derived expressions for the localisation angle and the critical plastic modulus **explicitly** for the Drucker-Prager yield criteria of equation 6.1. Then, the expression for c_1 and c_2 are

$$\begin{aligned} c_1 &= 9(s_1 + \nu s_3) + (1+\nu)q(m+n) \geq 0 \\ c_2 &= 9(s_2 + \nu s_3) + (1+\nu)q(m+n) \leq 0 \end{aligned} \tag{6.11}$$

where s_i are the principal deviatoric stress tensor components, $q = \sqrt{3J_2}$, m and n are given as

$$m = \frac{6\sin\varphi}{3 - \sin\varphi}, \qquad n = \frac{6\cos\psi}{3 - \sin\psi} \tag{6.12}$$

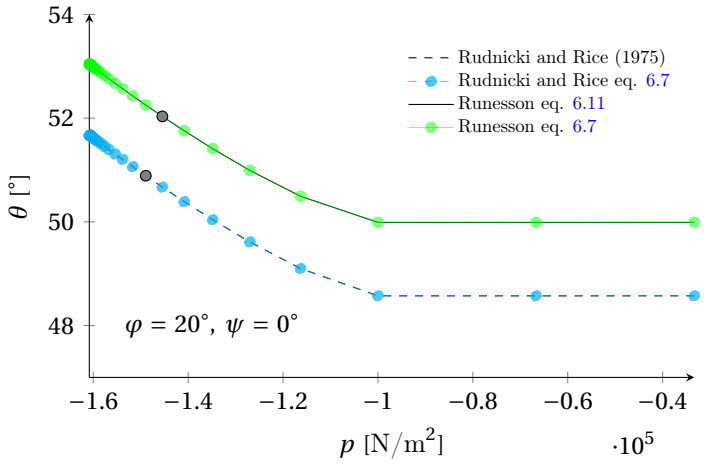

Figure 6.6: Angle θ [°] plotted against hydraustatic stress p [N/m^2]. The grey dots indicate the load step for which the value of H^{cr} becomes positive.

Now θ can be calculated with equation 6.7. The expression for the critical plastic modulus is

$$\frac{H^{\text{cr}}}{2G} = \frac{1+\nu}{36(1-\nu)}\left(2(m-n)^2 - (1-\nu)\left(\frac{9s_3}{q} + m + n\right)^2\right) \tag{6.13}$$

Equation 6.7 contains a general expression for computing the angle θ of the vector normal to the localisation plane and equation 6.8 contains general expressions for the c_i terms, which need to be substituted in equation 6.7. Those c_i terms are functions of the Poisson ratio and of the principal components of the gradients of the yield function and the plastic potential, which are functions of stress. Equation 6.8 is general, because every yield function can be used in these expressions. The same generalisation holds for equation 6.10, which is an expression for H^{cr}. Equation 6.8 and 6.10 are used as follows. First, the gradients of the yield function and the plastic potential are computed. Next, a relevant stress state is substituted in those gradients and now the expressions in those equations can be evaluated. Now, onset of localisation occurs when the plastic modulus of the corresponding stress state is smaller than or equal to the value of H^{cr}. Thus, at a certain moment during (plastic) loading of the FE-model, there may be a stress state for which this requirement is met and the localisation angle can then be computed for this stress state.
Equation 6.11 and 6.13 are the result of a substitution of the Drucker-Prager yield function (equation 6.1) and plastic potential (equation 6.3) in equations 6.8 and 6.10 and are therefore only valid for this Drucker-Prager yield function and plastic potential. Both the general equations 6.8 and 6.10 and the equations 6.11 and 6.13 are used in the verification process, since the expressions for θ and H^{cr} are very extensive and an error is easily made.

Rudnicki and Rice [13] also derived formulas for θ and H^{cr}, but they applied a different Drucker-Prager yield function. However, the analytical solutions of this research are also used to verify the solutions of the general expressions for θ and H^{cr} in equation 6.7 and 6.10. This is done by substitution of the Drucker-Prager yield function of Rudnicki and Rice [13] in the general equations 6.7, 6.8 and 6.10 and evaluating the resulting equations for the concerning stress states. The outcomes for θ and H^{cr} are then compared with the results of the evaluated expressions from Rudnicki and Rice [13].

θ and H^{cr} are plotted against the hydraustatic stress, which is shown in Figure 6.6 and 6.7 respectively. The stresses are obtained from the non-linear FE-analysis of the model in section 6.1.1. From Figures 6.6 and 6.7 it can be observed that the expressions of Rudnicki and Rice [13] result in solutions which are exactly equal to the solutions obtained with the general equation 6.7 of Runesson *et al.* [14]. The same holds for (the explicit Drucker-Prager) equations 6.11 and 6.13 of Runesson *et al.*. Hence, it can be concluded that the general expressions for θ (eq. 6.7) and H^{cr} (eq. 6.10) give good results for certain stress states after substitution of the required yield function. The numerical results can now be compared with the analytical results. The grey dots in the graphs indicate the load step for which the value of H^{cr} becomes positive. At this point, localisation (may) occurs. From Figure 6.7 it can be observed that due to the discrete load increments, a value of 0 for H^{cr} is slightly exceeded. Table 6.3 shows analytical solutions of θ and H^{cr} for different load cases at different load steps. The load steps

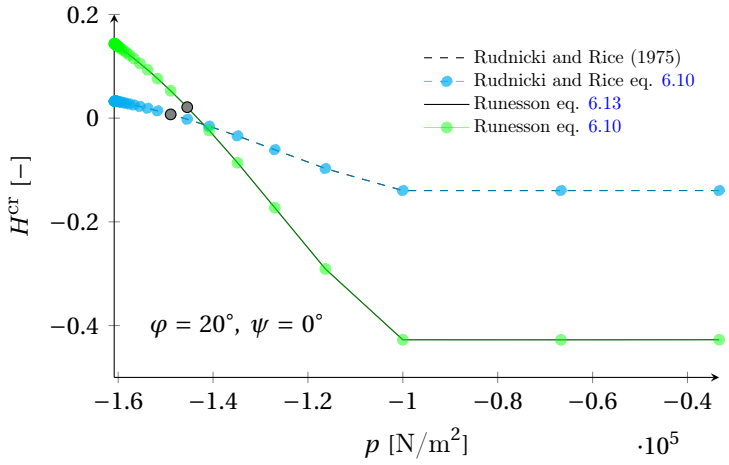

Figure 6.7: Plastic modulus H^{cr} [−] plotted against hydraustatic stress p [N/m^2]. The grey dots indicate the load step for which the value of H^{cr} becomes positive.

shown, are chosen such that the value of H^{cr} changes of sign. As stated before, when H^{cr} becomes positive, onset of localisation can occur, since the plastic modulus of the FE-model has a constant value of zero. H^{cr} does not become positive for load case 2. The reason for this will be explained later on.

Sanborn and Prévost [26] state that for localisation to occur, the value of the plastic modulus must be below the value of H^{cr} and plastic loading must take place. From Figure 6.2a it can be observed that the material is yielding at the points of onset of localisation. The value of the plastic modulus of the FE-model in section 6.1.1 has a constant value of zero (no hardening). For load case 1, the value of H^{cr} becomes positive in load step 10 ($\epsilon_{yy} = 4.0 \times 10^{-3}$). This is exactly the same load step as when the determinant becomes zero in the numerical calculation. The same holds for load case 3 and 4, for which the determinant becomes zero in load step 13 and 19 respectively. An overview of analytical and numerical results of θ at the load step when the determinant of the acoustic tensor becomes negative is given in Table 6.4. It can be observed that the analytical and numerical solutions are approximately the same. The small difference is probably due to the precision of the loop for computing the value of the determinant in the numerical analyses. As stated before, the loop computes the determinant with a precision of 1° and when the analytical solutions are rounded, the same values are obtained

load case						
1	θ [°]	49.13	49.35	49.53	49.67	49.77
$\varphi = 20°$	H^{cr}/G	-0.0284	-0.0044	0.0128	0.0251	0.0337
$\psi = 0°$	$F(\boldsymbol{\sigma})$ [N/m^2]	19.6	−3.36	−5.70	−32.9	15.5
	$-\epsilon_{yy}$	3.2×10^{-3}	3.6×10^{-3}	4.0×10^{-3}	4.4×10^{-3}	4.8×10^{-3}
2	θ [°]	58.53	58.61	58.66	58.67	58.70
$\varphi = 20°$	H^{cr}/G	-4.13×10^{-4}	-1.68×10^{-4}	-6.23×10^{-5}	-2.28×10^{-5}	-8.87×10^{-6}
$\psi = 20°$	$F(\boldsymbol{\sigma})$ [N/m^2]	−5.4	17.1	22.4	−9.24	−18.2
	$-\epsilon_{yy}$	5.2×10^{-3}	5.6×10^{-3}	6.0×10^{-3}	6.4×10^{-3}	6.8×10^{-3}
3	θ [°]	50.33	50.50	50.64	50.77	50.88
$\varphi = 25°$	H^{cr}/G	-0.0404	-0.0168	0.0024	0.0180	0.0307
$\psi = 0°$	$F(\boldsymbol{\sigma})$ [N/m^2]	−10.8	−14.1	−6.15	−9.05	3.92
	$-\epsilon_{yy}$	4.4×10^{-3}	4.8×10^{-3}	5.2×10^{-3}	5.6×10^{-3}	6.0×10^{-3}
4	θ [°]	51.76	51.86	51.95	52.03	52.12
$\varphi = 30°$	H^{cr}/G	-0.0233	-0.0068	0.0078	0.0208	0.0324
$\psi = 0°$	$F(\boldsymbol{\sigma})$ [N/m^2]	1.87	8.52	−24.1	−7.18	−2.31
	$-\epsilon_{yy}$	6.8×10^{-3}	7.2×10^{-3}	7.6×10^{-3}	8.0×10^{-3}	8.4×10^{-3}

Table 6.3: Analytical solutions of θ and H^{cr} at different load steps, for various values of φ and ψ.

load case	analytical	numerical	load step	ϵ
1	49.5°	50°	10	4.0×10^{-3}
2	58.7°	59°	15	4.0×10^{-3}
3	50.6°	51°	13	5.2×10^{-3}
4	51.9°	52°	19	7.6×10^{-3}

Table 6.4: Analytical and numerical solutions of θ at the load step when the determinant of the acoustic tensor becomes zero.

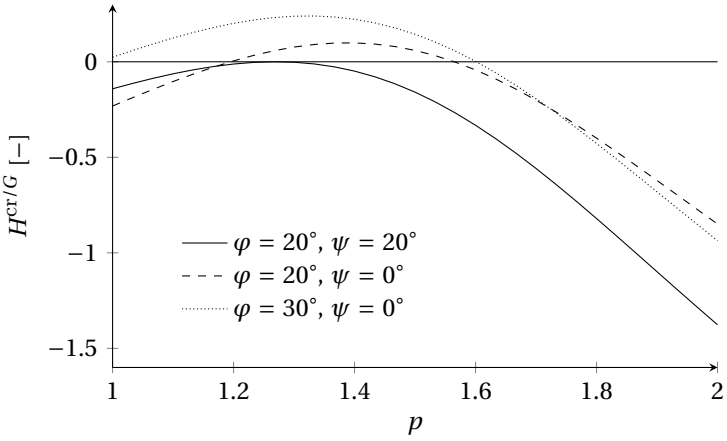

Figure 6.8: Plastic modulus H^{cr} [−], plotted against the hydraustatic stress p for associated and non-associated plastic flows.

as for the numerical results.

The results of load case 2 will be elucidated in this last part of the discussion. The determinant of the acoustic tensor never becomes bigger than or equal to zero during the non-linear FE-analysis of load case 2. This is analogous with the analytical results. When $\varphi = \psi$, the plastic flow is associated and when the plastic flow is associated, H^{cr} never becomes bigger than zero [13]. Figure 6.8 shows the value of H^{cr}/G versus the hydraustatic stress for associated and non-associated plastic flows. The stress state is chosen such that it varies from axially-symmetric extension to axially-symmetric compression. It can be observed that the value of H^{cr} only becomes zero for exactly one stress state when the plastic flow is associated. During a non-linear FE-analysis modeled with perfect plasticity, this stress state will not be reached due to the discrete load increments. This stress state can only be approached, as is the case for load case 2 (see Table 6.4). Therefore, onset of localisation can only occur for a model with an associated plastic flow if an tolerance is set for the minimal value of the determinant. For load case 2, a tolerance of 1×10^{-4} is used. The result is that onset of localisation occurs in load step 15 for load case 2.

6.1.4. Conclusions

Non-linear FE-analyses of a single Q4 plane strain element are executed for different combinations of the friction angle and the dilatancy angle. The objective is to obtain the correct point of onset of localisation and the corresponding localisation angle. The determinant of the acoustic tensor is computed during the numerical analyses, since onset of localisation occurs if the value of the determinant becomes smaller than zero. The results are verified with the numerical results of Leroy and Ortiz [29] and with the analytical results of Runesson *et al.* [14] and Rudnicki and Rice [13]. It can be concluded that the determinants and the localisation angles are computed correctly for plane strain models obeying a Drucker-Prager yield criteria with perfect plasticity. Special care must be taken when the plastic flow is associated and if the value of the plastic modulus is zero, because in this case, onset of localisation cannot occur during a numerical computation. A solution for this problem is to use a tolerance for the determinant of the acoustic tensor. In this work, a tolerance of 1×10^{-4} is used.

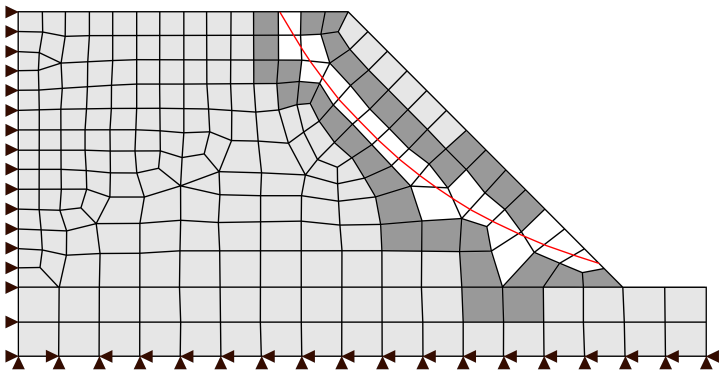

Figure 6.9: FE-model of a slope. The white coloured elements are the enrichment elements and the dark coloured elements are the blending elements. The red line is the mesh independent interface (slip surface) crossing the enrichment elements.

6.2. Verification of the propagation method on global level

In this section a development version of the PM is tested. The development version is restricted to Q4 elements and a pre-defined slip surface, modeled with enrichment elements which can reproduce a jump in the displacement field. The objective is to verify if the behaviour of the enrichment elements is correct in a FE-model of a slope during a non-linear analysis. The value of the CSN of the model with interface elements from Chapter 5.3 is used as a benchmark. This value gives an indication of the stability of the slope and it is required that the CSN of the PM is more or less equal to the benchmark. First, the FE-model is given, followed by the results of the PM. Some issues did arise in the analyses with the PM due to the enrichment elements. It is explained why these issues arise and how they are solved. Then, a discussion of the results follows and the chapter ends with the conclusions.

6.2.1. FE-model

The FE-model of the slope is shown in Figure 6.9. This is the same model as the model with interface elements and linear continuum elements from Chapter 5.3 (Figure 5.5). The only difference is that enrichment and blending elements are used instead of interface elements. The elements with the white colour are the enrichment elements and the elements with the dark colour are the blending elements. It can be observed that the slip surface is crossing the enrichment elements. The material properties of the linear continuum elements and the enrichment elements are given in Table 6.5. The blending elements have the same material properties as the linear continuum elements.

Just like the interface elements, the enrichment elements obey a Mohr-Coulomb friction law and failure in the enrichment elements occurs when the critical shear stress in the enrichment elements is reached. The analyses are run with a convergence criterion of 0.001, with a ceiling of 1000 iterations and the unit weight γ is incremented till non-convergence occurs. The enrichment elements have a normal stiffness modulus, d_n, of $1.11 \cdot 10^{11}\,\mathrm{N/m^3}$ and a shear stiffness modulus, d_s, of $1.11 \cdot 10^{8}\,\mathrm{N/m^3}$, which are the linear material properties of the interface in the enrichment elements.

6.2.2. Testing the development version of the propagation method

The analysis of the FE-model with enrichment elements was not able to converge in the first load increment. The displacement norm is shown in Figure 6.10 and the shear traction in the interface of the enrichment elements is shown in Figure 6.11. From the latter it can be observed that the shear traction is only large in a single corner of an enrichment element (blue dot). This enrichment element is also strongly deformed. Hence, the reason for this analysis error can be found in the modeling of this enrichment element.

In Figure 6.9 it can be seen that the interface in the concerning enrichment element is very close to the node of

element	γ [N/m^3]	E [N/m^2]	ν [−]	c [N/m^2]	φ [°]	ψ [°]
Q4/Q8	1000	$2 \cdot 10^8$	0.3	-	-	-
Enrichment el.	1000	$2 \cdot 10^8$	0.3	10000	30	0

Table 6.5: Material properties of the linear continuum elements and the enrichment elements.

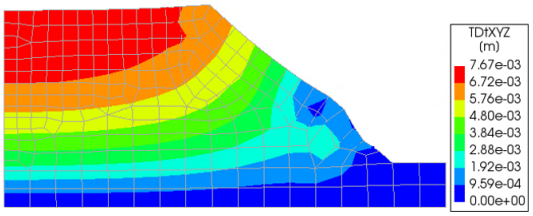

Figure 6.10: Displacement norm of the XFEM model. The model did not converge in the first load increment.

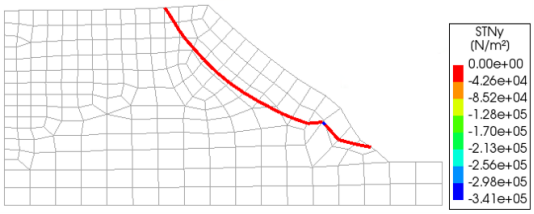

Figure 6.11: Mohr-Coulomb shear traction in the interface.

the element. Therefore, the corresponding integration element becomes very small. In the XFEM, the integration elements are needed to be able to properly integrate the enrichment functions. Figure 6.12 shows an enrichment element, crossed by an interface (red line). The enrichment functions in the element, in this case Heaviside functions, are non-smooth. Numerical quadrature is based on smooth polynomials. In order to exactly integrate non-smooth functions numerically, the non-smooth functions have to be made smooth again. Therefore, the enrichment element is divided in triangular integration elements, as shown in Figure 6.12. This way, the non-smooth Heaviside function is divided into smooth functions in those integration elements. Now, the Heaviside function can be properly integrated with Gauss quadrature.

However, numerical issues arise when the interface is too close to the nodes of the element, such as in the concerning element in Figure 6.11. If the interface becomes closer to the nodes, then the integration elements become smaller. And if the integration elements become smaller, the values in the corresponding stiffness matrices become smaller. The result is an ill-conditioned system of equations and the system cannot be solved. This is the reason for the non-convergence of the analysis of the model in Figure 6.9 in the first load increment. A remedy would be to create a FE-model with enrichment elements, which do not contain interfaces close to the nodes [2].

Therefore, the model in Figure 6.9 is generated again, with a manually generated mesh around the interface. The mesh is generated such that the integration elements are large enough to prevent an ill-conditioned system of equations. The updated mesh is shown in Figure 6.13. The load on the slope is applied again, until failure occurs. Figure 6.14 shows the displacement norm of the slope at the moment of failure. It is clearly visible that failure of the slope occurs in the interface of the enrichment elements and that the results are similar to those of the model with interface elements (see Figure 5.7). It must be noted that the discontinuity seems a weak discontinuity, instead of a strong discontinuity, but this is the result of the linear interpolation of the displacements inside the enrichment elements during the post-processing of the displacements.

The dimensionless displacement is plotted versus the SN and shown in Figure 6.16, together with the results of the model with interface elements.

[2] The purpose of XFEM is that it should not be dependent on the orientation of the mesh. However, the integration elements must not be too small to prevent singularities. When the XFEM method is fully developed, this issue is solved in a more elegant way.

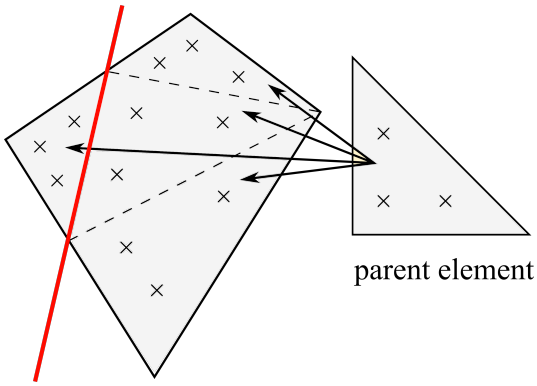

Figure 6.12: Enrichment element, divided in integration elements.

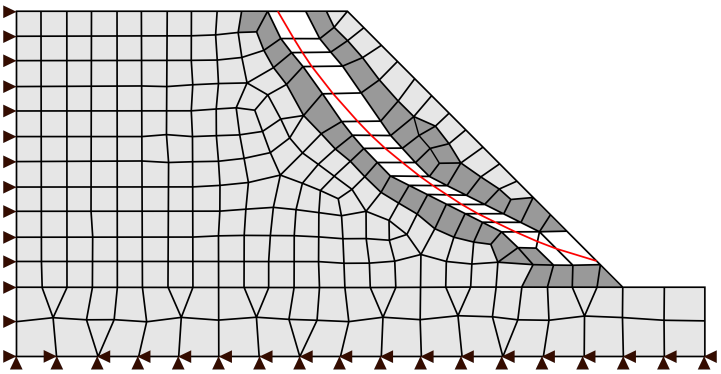

Figure 6.13: XFEM model of a slope with a manually generated mesh around the interface. The white coloured elements are the enrichment elements and the dark coloured elements are the blending elements. The red line is the mesh independent interface (slip surface) crossing the enrichment elements.

6.2.3. Discussion

There are some issues regarding to the integration elements of the enrichment elements used in the PM. As seen from the results in Section 6.2.2, the analyses did not converge when the interfaces are too close to the nodes of the elements, *i.e.*, when the interface cuts the element in two parts with significantly different sizes. This leads to ill-conditioning of the system matrix and the system of equations becomes near singular. Hence, the analysis is not able to convergence and locally spurious modes occur as was observed in Figure 6.10 and 6.11. This ill-conditioning problem of the XFEM is well known. Fries [10] mentions three solutions to circumvent the issues. The first solution is simply blocking the enriched degrees of freedom in the elements with small integration elements. However, this probably interrupts the continuity of the slip surface which is unwanted. The second solution is to move the nodes near the interfaces. This solution is effective, but not simple to implement and also restricts a fully mesh independent interface. The third solution is a stabilisation technique provided by Loehnert [15], although this is limited to symmetric matrices and is not applicable to problems with instability phenomena on element level. Both limitations are valid for this work, since onset of localisation is an instability on element level and the dilatant behaviour results in non-symmetric matrices.

A fourth solution could be to manipulate the indices of the stiffness matrix of the integration elements that causes the ill-conditioning. The values of these indices should be kept at a threshold value if the values of the indices in the stiffness matrix become too small. This threshold value should be large enough, such that (near) singularity of the global system of equations is avoided. The downside is that locally the stiffness is changed. Further research is needed to investigate whether this is a realistic and applicable solution.

The failure mode in Figure 6.14 is correct, since the failure mode is similar to that of the model with interface elements in Figure 5.7. The difference is that the model with interface elements clearly shows a strong discontinuity, where Figure 6.14 shows a weak discontinuity. This difference is caused by the post-processing of the displacements in the enrichment elements, where the displacements are linearly interpolated. The shear traction in the slip surface, shown in Figure 6.15, is not correct. The value of the shear traction seems to make random jumps, while the value should be smooth. Figure 6.16 shows very large values for the CSNs of the PM. A CSN of 190 is obtained with the SLIM and 200 with the MLIM, while the value of the benchmark is 45.2 (see Chapter

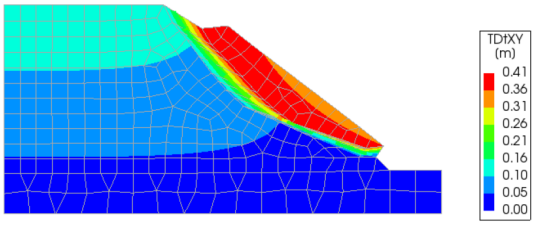

Figure 6.14: Displacement norm of the converged analysis of the XFEM model.

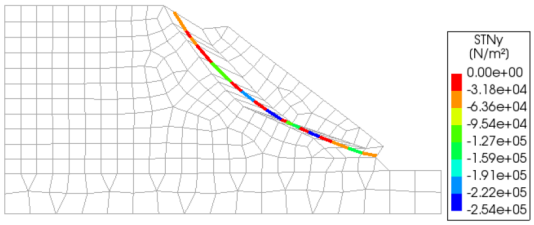

Figure 6.15: Mohr-Coulomb shear traction in the interface.

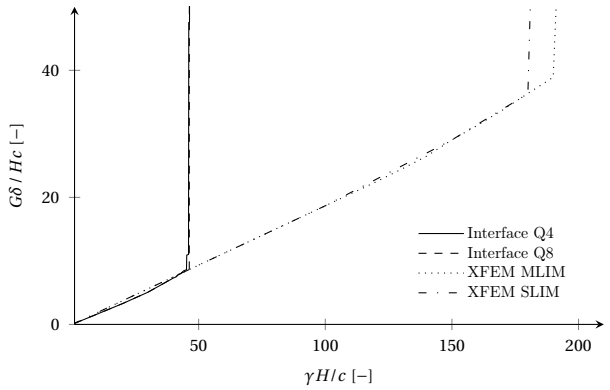

Figure 6.16: Dimensionless displacement versus the stability number. The results of the PM are plotted together with the results of the model with interface elements. Q4 and Q8 elements and a mesh size of 0.5m are used for the results of the model with interface elements.

5.3), obtained by the model with linear interface elements. This is more than 4 times larger and means that the enrichment elements do not work properly in a non-linear analysis of the FE-model of the slope. Further investigation is needed to be able to solve this problem. Probably, the high value of the CSN is the result of the incorrect computation of the shear traction in the interface. The displacements in the linear elastic phase are equal, which means that the linear behaviour of the interface in the enrichment elements is correct.

6.2.4. Conclusions

In this section, a development version of the PM is tested. A non-linear analysis of a slope with linear continuum elements and enrichment and blending elements is executed. The objective is to test the enrichment elements, which are part of the PM. To achieve this, a predefined slip surface is used, and the results are compared with the results of the FE-model containing interface elements, which serve as a benchmark.

First it was observed that system of equations becomes singular when the interfaces are too close to the nodes of the enrichment elements. Therefore, the PM can only be tested properly if the integration elements are large enough. To overcome this error, the enrichment elements are manually created around the interface. More pragmatic solutions were proposed by Fries [10]. One of those solutions seems applicable for the PM, which is to move the nodes near the interfaces. However, this imposes a restriction on the mesh independency of the interface. A fourth solution is proposed in this work, which is to set a threshold value for the indices of the stiffness matrix of the integration elements. Further research is needed to investigate what the best solution would be.

In the end it can be concluded that the CSN, computed with the development version of the PM, is not correct. A value of 190 is obtained with the SLIM and 200 with the MLIM. This is more than 4 times larger than the value of the benchmark (45.2). This benchmark was obtained by a convergence study of the FE-model, containing interface elements. The shear traction is not computed correctly in the enrichment elements, which is probably the cause for the large values of the CSN.

7

Discussion and conclusions

7.1. Discussion and conclusions

A relatively new XFEM-based method for analysing slope stability is being implemented in the finite element software of Diana FEA. Unique with respect to other numerical slope stability methods, like the strength reduction method (SRM) or the slip surface method (SSM), is that this method captures onset of localisation and the progression of the slip surface. Enrichment elements are representing the slip surface and are able to reproduce a jump in the displacement field. This XFEM-based analysis method is called the propagation method (PM) in this work. The PM can be applied to FE-models consisting rate independent elasto-plastic solids.

The process of the PM can be divided in three steps. First, onset of localisation is detected during load increments in the integration points of the elements. Then enrichment elements are implemented at the location of localisation, which are able to reproduce a jump in the displacement field. In the consecutive load increments an algorithm searches for detection of localisation in adjacent elements. Continuity of the slip surface is guaranteed by extending the slip surface slightly past the edge of the elements. From here on, the implementation of the enrichment elements continues till a fully developed slip surface is present, resulting in global failure of the slope. The objective of this work is to verify onset of localisation and to provide a method for verification of the point of global failure in a computation with the propagation method.

The requirement for onset of localisation in a point is that the determinant of an acoustic tensor must be zero. The acoustic tensor is dependent on the stress state and on the material properties and therefore the onset of localisation requirement is being monitored at the integration points of the FE-elements. If the requirement is met, onset of localisation occurs and the corresponding vector, normal to the localisation plane, is obtained. In this work, a plane strain element is analysed in order to verify whether onset of localisation occurs in the correct load step and if the corresponding localisation angle is correct. The results are verified with the numerical results of Leroy and Ortiz [29] and with the analytical solutions of Runesson *et al.* [14] and Rucnicki and Rice [13]. The plane strain model is tested for associative and non-associative plastic flows and a Drucker-Prager yield function with perfect plasticity. Since the results are equal to the results of Leroy and Ortiz [29] and to the analytical solutions, it can be concluded that onset of localisation is detected properly and that the corresponding normal vector is correct. Special care must be taken when the plastic flow is associated and if the value of the plastic modulus is zero, because in this case, onset of localisation cannot occur during a numerical computation. A solution for this problem is to use a tolerance for the determinant of the acoustic tensor.

A critical stability number (CSN) is a dimensionless factor that gives an indication of the stability of a slope. In order to obtain the CSN, the unit weight of the slope is increased until global failure occurs. It is possible to directly compute a CSN with the PM, since an analysis with the PM is based on load increments. The CSN is then computed at global failure of the slope, *i.e.*, when the slip surface is fully developed.

The SRM and the SSM assess the stability of a slope by a factor of safety (FOS). The FOS is similar to a CSN, but computed differently. A relation between the CSN and the FOS is needed to be able to compute a CSN with the PM which is equivalent to a FOS of the SRM and the SSM. Then it is possible to verify the CSN of the PM with the FOS of the SRM and the SSM. The relation between the CSN and the FOS is established mathematically through the definitions of those factors and by a physical interpretation. The assumptions are that the soil is homogeneous, the unit weight is uniformly distributed and the soil undergoes no hardening or softening. A method is proposed for computation of a FOS with the PM, which is equivalent to a FOS of the

SRM and the SSM. This method combines increments of the unit weight with reduction of the internal friction angle of the soil. Numerical proof showed that a FOS is obtained by this hybrid method, which is exactly similar to a FOS of a SRM.

Next, parameter studies and convergence studies were performed in order to obtain benchmarks which can be used for verification of the CSN and the FOS of the PM. It must be mentioned that the benchmarks are only valid for the corresponding FE-models.

The effect of the Poisson ratio on the FOS is studied and the results are presented in displacement versus FOS plots. The characteristics of these plots can be used for verification of the FOS of the PM. A value of 0.2, 0.3 and 0.4 for the Poisson is used. In general, the FOS obtained for a Poisson ratio of 0.2 and 0.3 is equal and a value of 0.4 results in the largest FOS. Failure of the slope is more abrupt of the Poisson ratio increases. The convergence study of the FOS with the manual strength reduction method (MSRM) and the SSM resulted in the following benchmarks. The MSRM converged to a value of 1.35 and with the SSM a value of 1.40 is obtained.

Then the effect of the dilatancy angle on the CSN was studied in order to obtain characteristic behaviour which can be used for the verification of the PM. It can be concluded that the CSN increases if the dilatancy angle is increased. A convergence study of the CSN resulted in a value of 28. Next, a convergence study was performed of the FOS of a FE-model with interface elements and linear continuum elements in order to obtain a benchmark which is used for verification of a development version of the PM. This resulted in a robust value of 45.2 for the CSN.

In the end, a development version of the PM was tested and verified. The objective was to verify the behaviour of the enrichment elements in a FE-model of a slope. The benchmark of the model with interface elements is used for the verification. An error occurred in the analysis with the development version of the PM when the interfaces are too close to the nodes of the enrichment elements. When this happens, the system of equations becomes ill-conditioned, which results in non-convergence of the analysis. To overcome this error, the enrichment elements are manually created around the interface. A more pragmatic solution is to move the nodes near the interfaces in an automatic procedure. In the end it can be concluded that the CSN, computed with the development version of the PM, is not correct. A value of 190 was obtained, which is about 4 times larger than the value of the benchmark (45.2). The shear traction is not computed correctly in the enrichment elements, which is probably the cause for the large values of the CSN.

7.2. Expectations and recommendations

- For a FE-model with an associated plastic flow and perfect plasticity, it is recommended to use a tolerance for the value of the determinant of the acoustic tensor. Otherwise onset of localisation will not be detected, since the determinant only approaches a value of zero.
- It is proposed to model the friction angle as a function of the unit weight in order to compute a FOS with the PM which is similar to a FOS of the SRM and the SSM. It is expected that this reduction of the friction angle can be integrated in the PM.
- Further investigation is needed to resolve the ill-conditioning problem of the enrichment elements. The same holds for the enrichment elements in a FE-model of a slope. The shear traction in the interface of the enrichment elements is not computed correctly. Therefore a proper behaviour is expected if the shear traction is computed correctly.
- The FOS should result in a value between 1.35 and 1.40 when testing the PM on the FE-model of Griffiths and Lane [9]. A combination of unit weight increments and friction angle reduction (hybrid method) should be used.
- If the PM is tested on the model of Manzari and Nour [17] (only increments of the unit weight), the CSN should converge to a value of 28 when the mesh size is reduced.
- When generating benchmarks for other FE-models, special care must be taken for the choice of the convergence criterion, the maximum number of iterations, mesh size and precision of the FOS. Non-convergence of the analyses may occur, while the slope is still stable. Therefore, the advice is given to compute the FOS or CSN at initiation of excessive vertical displacements in the sliding part of the slope.
- This work provides benchmarks generated with models containing interface elements and **linear** continuum elements. These benchmarks are used to verify the behaviour of the enrichment elements in a FE-model of a slope with linear continuum elements. The next step in the verification process would be to verify

enrichment elements in a model with **non-linear** continuum elements, with results of a model containing interface elements and non-linear continuum elements.

A

XFEM examples

In this section an example is given of the application of XFEM on a problem with a weak discontinuity to give an illustration of the method. This self worked-out example is part of an answer on problem 1 from the course "Enriched Finite Element Methods (ME46080)", given by Alejandro M. Aragón at the technical university of Delft. The final project of the course is given at the back of this example. The problem is solved with use of standard FEM and with XFEM to show that optimal convergence is recovered with XFEM. The convergence rates are determined with the relative error in the energy norm.

A.1. The problem

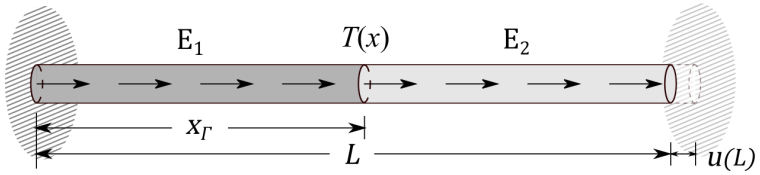

Figure A.1: A 1D bar with weak discontinuity in the center, indicated by $\Gamma(x)$. The Young's modulus changes value across the interface.

The 1D bar boundary value problem is (see also Figure A.1)

$$-\frac{d}{dx}(EA\frac{du}{dx}) = T(x) \qquad 0 < x < L, \tag{A.1}$$

The essential boundary conditions (BCs) are u(0) = 0 and u(L) = 1. The length of the bar = 10 and the cross sectional area, A = 1. The material interface x_Γ is located at L/2. The bar is subjected to a distributed force per unit length given by:

$$T(x) = 25x - \frac{15}{2}x^2 + \frac{1}{2}x^3 \tag{A.2}$$

The exact solution to this problem is given by

$$u(x) = \begin{cases} \frac{1}{E_1}(E_2 B x + g(x) & x \le x_\Gamma \\ B(x-L) + 1 + \frac{1}{E_2}(g(x) - g(L)) & x \ge x_\Gamma \end{cases} \tag{A.3}$$

where B and g(x) are

$$B = \frac{E_1 E_2 - g(x_\Gamma)(E_2 - E_1) - g(L)E_1}{E_2((E_2 - E_1)x_\Gamma + LE_1)}, \qquad g(x) = -\frac{25}{6}x^3 + \frac{5}{8}x^4 - \frac{1}{40}x^5 \tag{A.4}$$

This analytical solution can easily be obtained by using software like Maple. The Young's modulus, E_1 = 10000 and E_2 = 1000. The exact strain energy is U = 92.95522186, which is obtained by evaluating the following expression

$$U = \int_{\Omega} \frac{1}{2} EA \left(\frac{du}{dx}^2 \right) dx \tag{A.5}$$

The exact solution and it's derivative are shown in Figure A.2

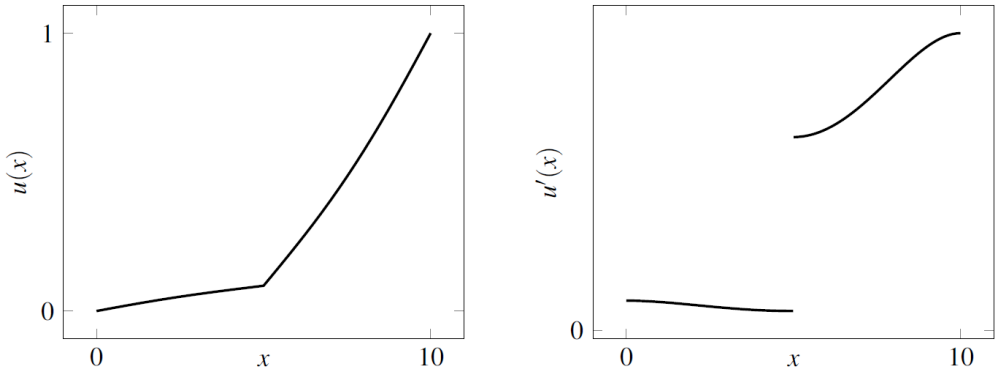

Figure A.2: Analytical solution of the boundary value problem and it's derivative.

A.2. Approximation with standard FEM

First, the problem is solved by using standard FEM (linear shape functions) with 2, 4, 8 16 and 32 elements and with 3, 5, 9, 17 and 33 elements. The shape functions used are $\varphi 1 = \frac{1-x}{2}$ and $\varphi 2 = \frac{1+x}{2}$. The results are shown in Figure A.3a and Figure A.3b.

It can be observed that the model with an even number of elements gives a good approximation of the exact solution. The discontinuity is determined by the C^0 continuity of the approximation. The model with an odd number of elements gives a bad approximation of the exact solution. This is caused by the location of the interface and the positioning of the elements. The interface is located in the middle of an element and this element can not reproduce the weak discontinuity.

The relative error in the energy norm is calculated with the following expression

$$\mathscr{E} = \sqrt{\left| \frac{U - U_h}{U} \right|} \tag{A.6}$$

where U is the exact strain energy and U_h the strain energy of the approximation. The strain energy of the approximation, U_h is

$$U_h = \mathbf{u}^T \mathbf{K}\, \mathbf{u} \tag{A.7}$$

with $\mathbf{u}$ the DOFs and $\mathbf{K}$ the system matrix. The relative error in the energy norm is plotted against mesh size h and shown in Figure A.4. It can be observed that the rate of convergence (ROC) = 1 and algebraic for the even elements, which is optimal for linear elements in 1D. The ROC for the odd elements is 0.51, which is far from optimal.

A.3. Approximation with XFEM

In this section, optimal convergence rates are retrieved using XFEM. The Sukumar enrichment function (Figure 2.6) is used to show that spurious behaviour occurs if enrichment functions are chosen which are not of zero value in the enriched nodes. If the enrichment function is not zero in the enriched nodes, then the enrichment function is also active in the blending elements (Figure 2.6). The second enrichment function is the Möes enrichment function (Figure 2.7). This function is constructed in such a way that the function is of zero value in the enriched nodes. Hence, the enrichment function is not active in the blending elements. The XFEM approximations are shown in Figure A.5.

In Figure A.5a and A.5c the approximation with the Sukumar enrichment is shown. The standard DOFs are plotted and it can be noted that these DOFs are not lying on the displacement field at the location of the enriched nodes. This means that the standard DOFs do not have a physical meaning at the enriched nodes. This is due to the

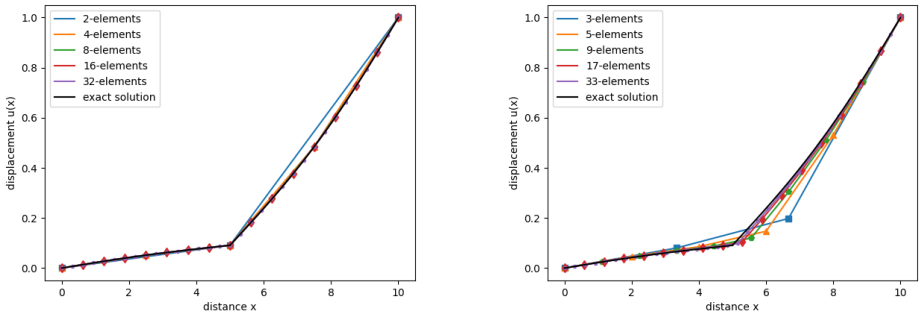

(a) Interface at the nodes of the middle elements.

(b) Interface in the middle element.

Figure A.3: Displacement field u(x) vs. the length of the bar x.

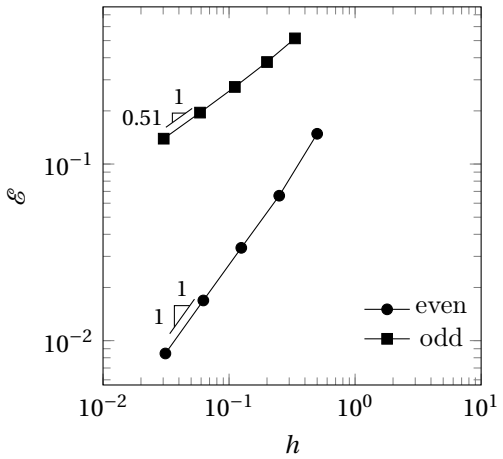

Figure A.4: Loglog plot of the relative error in the energy norm against element size of linear approximation.

enrichment function, which is not zero at the enriched nodes. It can also be observed that the displacement field has a kink inside the representative element, which represents the weak discontinuity. However, the displacement field acts strange around the discontinuity, which is caused by the active enrichment function inside the blending elements. Figure 2.7 and A.5d shows the approximation with the Möes enrichment. Now the standard DOFs preserve their physical meaning, because the enrichment function has a zero value in the nodes. The representative element shows a perfect kink at the location of the discontinuity.

The relative error in the energy norm of the XFEM approximation is calculated and plotted against the mesh size. The error and corresponding convergence rates are shown in Figure A.6. Both approximations have algebraic convergence, but the convergence rate of the Sukumar approximation is 0.50, while the convergence rate of the Möes approximation is 1. This means that optimal convergence is recovered using XFEM and an appropriate enrichment function.

A.4. Implementation of XFEM

In this section, the implementation of XFEM with the Möes enrichment function is described for problem A.1 with 3 elements. Figure A.8 shows the 3 bar elements and the standard shape functions φ_i. The middle element is the representative element and nodes 2 and 3 are enriched with the Möes enrichment functions E_{21} and E_{31}. The enrichment functions are constructed such that they are of zero value at nodes 2 and 3 and in the blending elements. The interface is at x_Γ.

The general approximation field of XFEM is described with the following equation

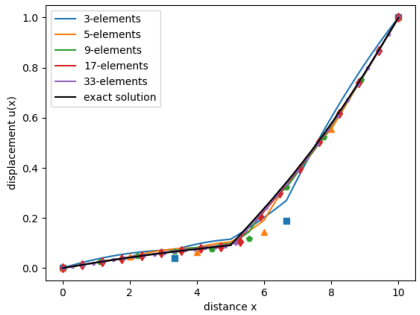

(a) Sukumar approximation.

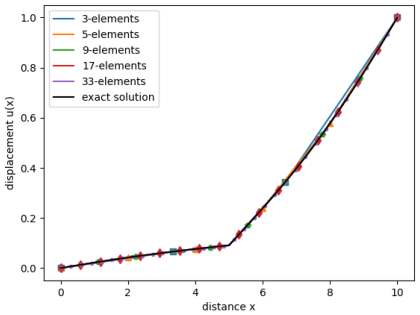

(b) Möes approximation.

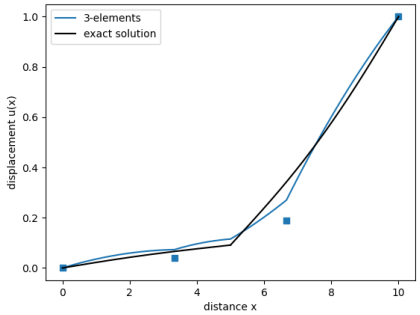

(c) Sukumar approximation with 3 elements.

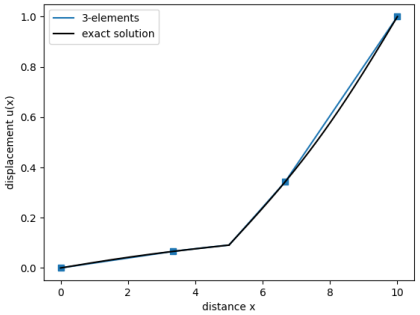

(d) Möes approximation with 3 elements.

Figure A.5: Displacement field u(x) vs. the length of the bar x of GFEM approximations.

$$u^h(x) = \underbrace{\sum_{\alpha \in I_h} \hat{u}_\alpha \varphi_\alpha(x)}_{\text{std. FEM}} + \underbrace{\sum_{\alpha \in I_h^e} \varphi_\alpha(x) \sum_{j=1}^{m_\alpha} \tilde{u}_{\alpha j} E_{\alpha j}(x)}_{\text{enriched XFEM}} \tag{A.8}$$

Only node 2 and 3 are enriched with 1 enrichment function. Hence equation A.8 becomes

$$u^h(x) = \underbrace{\sum_{\alpha=1}^{4} \hat{u}_\alpha \varphi_\alpha(x)}_{\text{std. FEM}} + \underbrace{\sum_{\alpha=2}^{3} \varphi_\alpha(x) \tilde{u}_\alpha E_\alpha(x)}_{\text{enriched XFEM}} \tag{A.9}$$

Note that the summation over the enriched DOFs vanishes, because there is only 1 enrichment per node. Now, recall that the expression for an element stiffness matrix of a bar in parent coordinates is

$$\mathbf{K}_e = \int_{\Omega_e} EA\mathbf{B}^T(\xi)\mathbf{B}(\xi)\, j\, d\xi \tag{A.10}$$

or in discrete form

$$\mathbf{K}_e = \sum_i EA\mathbf{B}^T(\xi_i)\mathbf{B}(\xi_i)\, j\, W_i \tag{A.11}$$

where $\mathbf{B}(\xi_i)$ the strain displacement matrix, evaluated at the Gauss points ξ_i, j the determinant of the Jacobian matrix and W_i the corresponding weights. The standard shape functions in parent coordinates are

$$\varphi_1 = \frac{\xi - 1}{2}, \quad \varphi_2 = \frac{\xi + 1}{2} \tag{A.12}$$

Substitution of A.12 in A.13 gives the element stiffness matrices of element 1 and 3

$$\mathbf{K}_1 = \begin{bmatrix} 3000 & -3000 \\ -3000 & 3000 \end{bmatrix}, \quad \mathbf{K}_3 = \begin{bmatrix} 300 & -300 \\ -300 & 300 \end{bmatrix} \tag{A.13}$$

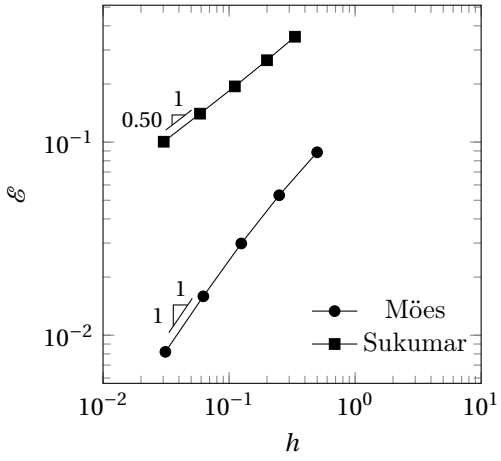

Figure A.6: Loglog plot of the relative error in the energy norm against element size of GFEM approximation.

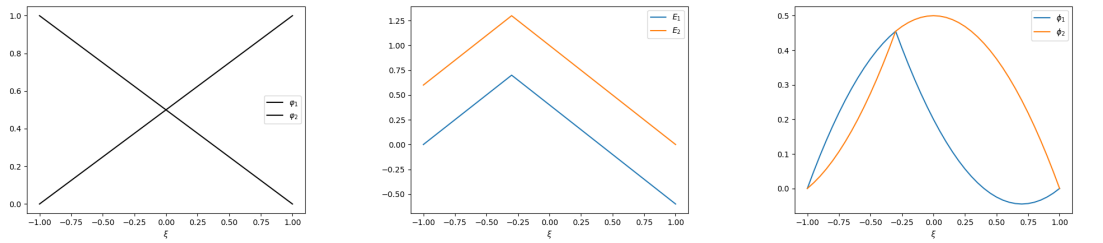

(a) Partition of unity. (b) Möes enrichment functions. (c) Generalized enrichment function.

Figure A.7: Construction of generalized enrichment functions: $\varphi_\alpha \cdot E_\alpha = \phi_\alpha$.

Figure A.8: XFEM approximation of the BV problem with 3 elements.

The values of the indices of the element stiffness matrix $\mathbf{K}_1$ are different than the indices of matrix $\mathbf{K}_3$, because the Young's modulus takes different values at the left and the right of the interface. Note that node 2 and 3 are enriched, but the enrichment functions are constructed in such a way that they are zero in the blending elements. That is why only the standard shape functions are acting in elements 1 and 3. If the enrichment functions are not zero at the nodes, then the enrichment functions are also acting in the blending elements, as is the case with the Sukumar enrichment. Now for the stiffness matrix of the second element, the complete expression of equation A.9 is active. In this equation $\hat{u}$ are the standard DOFs and $\tilde{u}$ are the enriched DOFs. The enrichment functions E_2 and E_3 are specified in parent coordinates. This is possible if the location of the interface is mapped from global to parent coordinates. It is also possible to specify the enrichment function in global coordinates. The benefit of specifying the enrichment function in global coordinates is that no coordinate transformation is involved, but the downside is applying the chain rule when computing the strain-displacement matrix. However, in this example the enrichment function is in parent coordinates. The enrichment functions E_2 and E_3 are

$$E_2 = |\xi_\Gamma + 1| - |\xi - \xi_\Gamma|, \quad E_3 = |\xi_\Gamma - 1| - |\xi - \xi_\Gamma| \tag{A.14}$$

where ξ_Γ is the location of the interface in the parent element. In this example $\xi_\Gamma = 0$. Substitution in equation A.14 gives

$$E_2 = 1 - |\xi|, \quad E_3 = 1 - |\xi| \tag{A.15}$$

The result is shown in Figure A.8. Note that the enrichment functions E_1 and E_2 are on top of each other, since the interface is in the middle of the element. A graphical illustration of these enrichment functions is shown in Figure A.7. This Figure shows the construction of the generalized enrichment functions, ϕ_α. Multiplication of the linear partition of unity shape functions, φ_α, with the Möes enrichment functions, E_α gives the generalized enrichment functions, ϕ_α, and the second term of equation A.9 is formed. It can be noted that the Möes enrichment functions

are not zero at the nodes if the interface is not in the middle of the element. This is why the multiplication with the partition of unity is performed. The multiplication forces the enrichment functions to zero at the other nodes.

The full approximation of the displacement field in the middle element becomes

$$u^h = \varphi_2 \hat{u}_2 + \varphi_3 \hat{u}_3 + \varphi_2 E_2 \tilde{u}_{21} + \varphi_3 E_3 \tilde{u}_{31} \tag{A.16}$$

where $\tilde{u}$ are the enriched DOF's, which will be added in the back of the system matrix as DOF 5 and 6. So in matrix form the displacement field is

$$u^h = \begin{bmatrix} \varphi_2 & \varphi_3 & \varphi_2 E_2 & \varphi_3 E_3 \end{bmatrix} \cdot \begin{bmatrix} \hat{u}_2 \\ \hat{u}_3 \\ \tilde{u}_{21} \\ \tilde{u}_{31} \end{bmatrix} \tag{A.17}$$

Substitution of equation A.17 in equation A.10 gives

$$\mathbf{K}_e = \int_{-1}^{\xi_\Gamma} E_1 \mathbf{B}^T(\xi)\mathbf{B}(\xi)\, j\, d\xi + \int_{\xi_\Gamma}^{1} E_2 \mathbf{B}^T(\xi)\mathbf{B}(\xi)\, j\, d\xi \tag{A.18}$$

The element stiffness matrix of the middle element is a summation of two definite integrals over integration elements. This means that the element has to be split in two sub domains. One on the left of the interface and one on the right. Otherwise the C^0 continuity can not be captured. Numerical integration of these integration elements involves extra mapping procedures which is not explained in this section.

The element stiffness matrix K_e becomes

$$\mathbf{K}_2 = \begin{bmatrix} 1650 & -1650 & -1350 & -1350 \\ -1650 & 1650 & 1350 & 1350 \\ -1350 & 1350 & 2200 & 1100 \\ -1350 & 1350 & 1100 & 2200 \end{bmatrix} \tag{A.19}$$

Assembly of the element stiffness matrices gives the system stiffness matrix as

$$\mathbf{K} = \begin{bmatrix} 3000 & -3000 & 0 & 0 & 0 & 0 \\ -3000 & 4650 & -1650 & 0 & -1350 & -1350 \\ 0 & -1650 & 1950 & -300 & 1350 & 1350 \\ 0 & 0 & -300 & 300 & 0 & 0 \\ 0 & -1350 & 1350 & 0 & 2200 & 1100 \\ 0 & -1350 & 1350 & 0 & 1100 & 2200 \end{bmatrix} \tag{A.20}$$

After proper sampling of the force vector, the system of equations can be solved. The displacement vector $\mathbf{u}$ is

$$\mathbf{u} = \begin{bmatrix} 3000 & 0.06575009 & 0.34249906 & 1 & -0.11073523 & -0.11569575 \end{bmatrix} \tag{A.21}$$

Evaluating expression A.9 gives the displacement field as shown if Figure A.5d.

Final Project

Enriched Finite Element Methods (ME46080)

In this project we study the performance of GFEM for problems with weak discontinuities. You *must* do PROBLEM 1 and choose either PROBLEM 2 or PROBLEM 3.

PROBLEM 1.— MATERIAL DISCONTINUITY [1]
Consider the 1-D boundary value problem

$$-\frac{\mathrm{d}}{\mathrm{d}x}\left(EA\frac{\mathrm{d}u}{\mathrm{d}x}\right)=T(x) \qquad 0<x<L, \tag{1}$$

with BCs $u(0)=0$ and $u(L)=1$. The bar consists of two materials with elastic modulus $E_1=10000$ and $E_2=1000$. The length of the bar is $L=10$ and the cross section $A=1$. The material interface is located at $x_\Gamma=L/2$. The bar is subjected to a distributed force per unit length given by

$$T(x)=25x-\frac{15}{2}x^2+\frac{1}{2}x^3. \tag{2}$$

The exact solution to this problem is given by

$$u(x)=\begin{cases}\frac{1}{E_1}\left(E_2Bx+g(x)\right) & x\le x_\Gamma\\ B(x-L)+1+\frac{1}{E_2}\left(g(x)-g(L)\right) & x\ge x_\Gamma\end{cases}, \tag{3}$$

where the constant B and the function $g(x)$ are given by

$$B=\frac{E_1E_2-g(x_\Gamma)(E_2-E_1)-g(L)E_1}{E_2\left((E_2-E_1)x_\Gamma+LE_1\right)}, \qquad g(x)=-\frac{25}{6}x^3+\frac{5}{8}x^4-\frac{1}{40}x^5,$$

respectively [1]. The exact strain energy for this problem is $U=92.95522186$. Figures 1a and 1b show the exact solution (3) and its derivative, respectively.

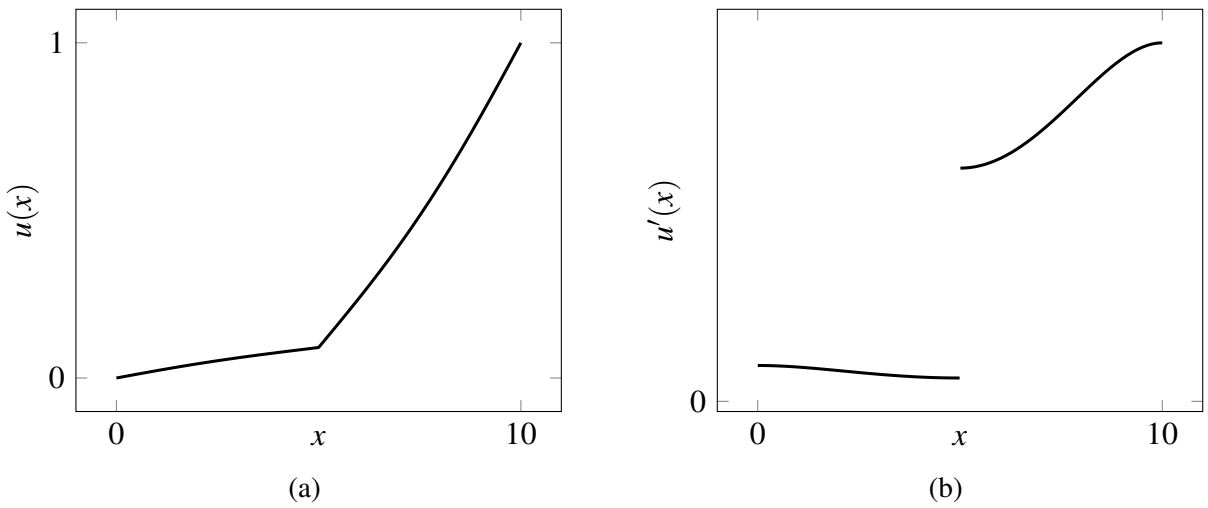

Figure 1: Exact solution (a) and its derivative (b) for problem (1) subjected to load (2).

Project tasks

1. Solve the problem using the *h*–version of FEM with linear Lagrange elements on uniform meshes consisting of
   - *i)* A sequence of meshes with an even number of elements, and thus the material discontinuity is at a node; and
   - *ii)* A sequence of meshes with an odd number of elements, and thus the discontinuity is located at the center of an element. For this case the stiffness matrix of the element containing the material interface must be integrated using two "integration elements".

   Make a log-log plot of the relative error in the energy norm versus the mesh size h. In all cases, compute the rate of convergence in the energy norm and indicate it in the plots.

2. Solve the problem with the sequence of odd elements using GFEM considering the following enrichments for material interfaces
   (i) Sukumar's enrichment [2];
   (ii) Möes' enrichment [3]; and
   (iii) Propose your own enrichment trying to deliver an optimal rate of convergence. Explain the rationale behind the proposed enrichment.
3. Repeat the problem above using the p–FEM and p–GFEM on uniform meshes with approximations of orders $p = 1,\ldots,5$. Use *(a)* four elements; and *(a)* five elements. Choose enrichment functions that will deliver exponential convergence.
   Make a log-log plot of the relative error in the energy norm versus the total number of degrees of freedom (DOFs). In all cases, compute the rate of convergence in the energy norm and indicate it in the plots.
4. Study the stability of all methods above. Make a plot of the condition number of the stiffness matrix as a function of $1/h$ for h–FEM and as a function of the total number of DOFs for p–FEM and p–GFEM. The condition number of the reduced matrix $\boldsymbol{K}_{\text{ff}}$ is defined as
$$\text{cond}\,(\boldsymbol{K}_{\text{ff}}) \equiv \frac{\lambda_{\max}}{\lambda_{\min}}, \tag{4}$$
   where $\lambda_{\max}$ and $\lambda_{\min}$ are the matrix maximum and minimum eigenvalues. For this problem, study what happens when an interface approaches a node of the original mesh.
5. Discuss (compare and draw conclusions) your results. One page limit.

PROBLEM 2.— PLATE WITH ELASTIC INCLUSION

Consider the circular linear elastic body $\Omega = \Omega_1 \cup \Omega_2$ with radius $b = 2$ shown in Figure 2. The body is composed of two materials as illustrated in the figure. The radius of the subdomain Ω_1 is $a = 0.4$. The Lamé constants in Ω_1 and Ω_2 are $\lambda_1 = \mu_1 = 0.4$ and $\lambda_2 = 5.7692, \mu_2 = 3.8461$, respectively. These values correspond to $E_1 = 1$, $\nu_1 = 0.25$ and $E_2 = 10$, $\nu_2 = 0.3$. Displacements in the radial direction and with magnitude equal to b are prescribed on the boundary $\partial\Omega$ of the domain.

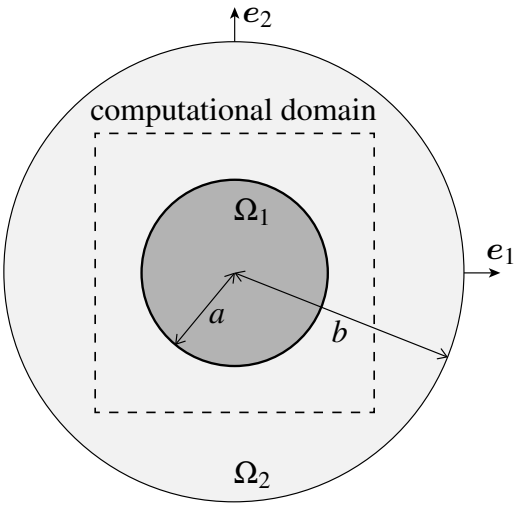

Figure 2: Bi-material boundary value problem. The square computational domain is represented by the dashed lines.

The exact solution of this problem in polar coordinates is given by [2]

$$u_r(r) = \begin{cases} \left[\left(1-\frac{b^2}{a^2}\right)\alpha + \frac{b^2}{a^2}\right] r & \text{for} \quad 0 \le r \le a, \\ \left(r - \frac{b^2}{r}\right)\alpha + \frac{b^2}{r}, & \text{for} \quad a \le r \le b, \end{cases} \tag{5}$$
$$u_\theta(r) = 0,$$

where

$$\alpha = \frac{(\lambda_1+\mu_1+\mu_2)b^2}{(\lambda_2+\mu_2)a^2 + (\lambda_1+\mu_1)(b^2-a^2) + \mu_2 b^2}.$$

The radial and hoop strains are given by

$$\varepsilon_{rr}(r) = \begin{cases} \left(1-\frac{b^2}{a^2}\right)\alpha + \frac{b^2}{a^2} & \text{for } 0 \le r \le a, \\ \left(1+\frac{b^2}{r^2}\right)\alpha - \frac{b^2}{r^2} & \text{for } a < r \le b \end{cases} \tag{6}$$

and

$$\varepsilon_{\theta\theta}(r) = \begin{cases} \left(1-\frac{b^2}{a^2}\right)\alpha + \frac{b^2}{a^2} & \text{for } 0 \le r \le a, \\ \left(1-\frac{b^2}{r^2}\right)\alpha + \frac{b^2}{r^2} & \text{for } a < r \le b \end{cases} \tag{7}$$

respectively. The stresses are given by

$$\begin{aligned} \sigma_{rr}(r) &= 2\mu\varepsilon_{rr} + \lambda\left(\varepsilon_{rr} + \varepsilon_{\theta\theta}\right), \\ \sigma_{\theta\theta}(r) &= 2\mu\varepsilon_{\theta\theta} + \lambda\left(\varepsilon_{rr} + \varepsilon_{\theta\theta}\right), \\ \sigma_{r\theta}(r) &= 0. \end{aligned} \tag{8}$$

where appropriate Lamé constants are used depending on the value on r.

In order to avoid meshing a circular domain, a square domain with edge length $L = 2$ is used (see dashed lines in Figure 2). The exact tractions are applied on the boundary of the square domain and point displacement constraints are applied in order to prevent rigid body motion. The components of the exact tractions $\bar{\boldsymbol{t}}$ in Cartesian coordinates can be computed by first transforming (8) and then computing $\bar{\boldsymbol{t}} = \boldsymbol{\sigma}\boldsymbol{n}$, where $\boldsymbol{n}$ is the unit normal vector to the boundary.

Project tasks

1. Solve the problem using the h–version of FEM and uniform meshes. Use a sequence of meshes with 11×11, 20×20, 40×40, 80×80 elements. Use linear and quadratic Lagrange elements.
2. Add enrichments for material interfaces:
   i) Sukumar's enrichment [2] defined as
   $$L_\alpha^\Gamma(\boldsymbol{x}) = \left|\|\boldsymbol{x}\| - a\right|. \tag{9}$$
   Here, we assumed that the origin of the global coordinate system is at the center of the circular domain Ω.
   ii) Propose and implement your own enrichment(s) for interfaces like the one in this problem. Try to choose one that will deliver optimal rate of convergence for linear and quadratic approximations (same rate as in a problem with a smooth solution). Explain the rationale behind the proposed enrichment.
3. Compute the exact strain energy using the exact solution. Alternatively, you can estimate the exact strain energy using the procedure based on *a posteriori* error estimates derived in class.
4. For each element type and enrichment used, make a log-log plot of the relative error in the energy norm versus the number of DOFs. In all cases, compute the rate of convergence in the energy norm and provide the computed/estimated exact strain energy.
5. Discuss (compare and draw conclusions) your results. One page limit.

When solving the problem with enrichment functions, we must identify elements cut by the material interface. This can be done by computing the *level set value* of all mesh nodes. The level set value Φ_i for a given node $\boldsymbol{x}_i$ is a scalar that represents the distance from the node to the circular interface, *i.e.*, $\Phi_i = \|\boldsymbol{x}\| - a$ (again assuming the center of the circle is at $\boldsymbol{x}_c = \boldsymbol{0}$). Notice that the level set value is negative for nodes that lie within the circle. Once the level set value for all mesh nodes is known, we can identify cut elements as follows:

- Loop over all elements $\Omega_e \in \Omega$;
- For each element Ω_e, loop over its edges;
- An edge defined by two nodes $\boldsymbol{x}_i$ and $\boldsymbol{x}_j$ is crossed by the circular interface if $\Phi_i\Phi_j < 0$.

PROBLEM 3.— GFEM$^{\text{GL}}$ MULTI-SCALE ANALYSIS OF A HETEROGENEOUS BAR

In this project, we study the application of the Generalized Finite Element Method with global-local enrichments (GFEM$^{\text{gl}}$) [4] to multi-scale material simulations. Let us consider a 1-D model problem governed by the differential equation

$$-\frac{\mathrm{d}}{\mathrm{d}x}\left(E(x)A\frac{\mathrm{d}u}{\mathrm{d}x}\right) = 0 \qquad 0 < x < L, \tag{10}$$

with boundary conditions

$$\begin{aligned} u(0) &= 0, \\ E(L)A\left.\frac{\mathrm{d}u}{\mathrm{d}x}\right|_{x=L} &= P. \end{aligned}$$

Eq. (10) represents the equilibrium equation for a bar of length L with cross section A, and Young's modulus $E(x)$, the latter which is an oscillatory function given by

$$E(x) = \begin{cases} E_H & \text{if } 0 \le x \le \frac{3L}{8}, \\ \tilde{E}(x) & \text{if } \frac{3L}{8} < x < \frac{5L}{8}, \\ E_H(x) & \text{if } \frac{5L}{8} \le x \le L, \end{cases} \tag{11}$$

where the *homogenized* Young modulus, E_H, is taken as

$$E_H = \frac{E_1 E_2}{E_1 \bar{V}_2 + E_2 \bar{V}_1}, \tag{12}$$

with volume fractions $\bar{V}_1 = \bar{V}_2 = 0.5$ and $E_1 = 1, E_2 = 40$. These are the material properties of the white and black phases shown around the center of the bar in Figure 3.

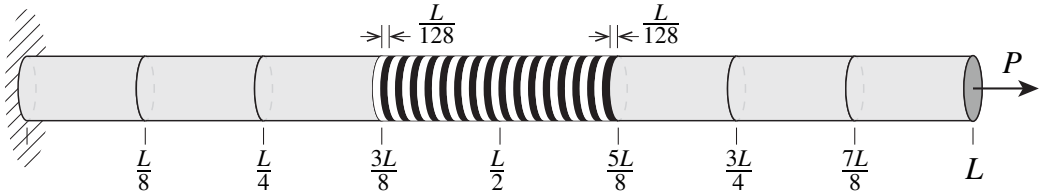

Figure 3: Bar with heterogeneous material. The white and black phases have Young's modulus $E_1 = 1$ and $E_2 = 40$, respectively.

Young modulus $\tilde{E}(x)$ represents a periodic heterogeneous material given by

$$\tilde{E}(x) = \begin{cases} E_1 & \text{if } x \in \text{white phase}, \\ E_2 & \text{if } x \in \text{black phase}. \end{cases} \tag{13}$$

The length of each phase is taken as $\Delta L = L/128$, as illustrated in Figure 3.

It is assumed that the assumptions of the homogenization theory are valid away from the center of the bar. The solution of the problem in the region where $E(x) = \tilde{E}(x)$ varies very quickly due to changes in material property. As a result, a very fine finite element mesh must be used for acceptable accuracy.

Many problems of engineering relevance behave like this model problem: Homogenized material properties can be used everywhere except at some critical locations near stress risers, cracks, *etc.* In those regions, the actual material properties must be used for accurate results. However, this may require extremely fine meshes. In this project we explore the application of the GFEM$^{\text{gl}}$ to this class of problems. Similar 3-D problems are solved in [4] using GFEM$^{\text{gl}}$.

The exact solution of this problem is given by

$$u(x) = P\int_0^x \frac{1}{E(x)}\,\mathrm{d}x = \begin{cases} \frac{P}{E_H}x & \text{if } 0 \le x \le \frac{3L}{8}, \\ \frac{P}{E_H}\frac{3L}{8} + P\int_{\frac{3L}{8}}^{x} \frac{1}{\tilde{E}(x)}\,\mathrm{d}x & \text{if } \frac{3L}{8} < x < \frac{5L}{8}, \\ \frac{P}{E_H}\frac{3L}{8} + P\frac{L}{8}\left(\frac{1}{E_1}+\frac{1}{E_2}\right) + \frac{P}{E_H}\left(x - \frac{5L}{8}\right) & \text{if } \frac{5L}{8} \le x \le L. \end{cases} \tag{14}$$

Project tasks

1. Compute the exact strain energy for the problem. Derive it analytically using the expression for the bilinear form, $B(u,u)$, of the problem and the exact solution. Your solution should have at least 12 significant figures.
2. Solve the problem with the standard FEM and $p = 1$. Adopt uniform meshes with element size

$$H = \left\{\frac{L}{8}, \frac{L}{16}, \frac{L}{32}, \frac{L}{64}, \frac{L}{128}, \frac{L}{256}\right\}.$$

   Note that the Young modulus is not constant within each finite element (except for the finest mesh). This must be taken into account when integrating the stiffness matrix. Use a large number of Gauss points (20 or more) or an adaptive integration scheme. If using Gauss points, show that the rule selected is sufficiently accurate. Plot the FEM solution for the first five mesh sizes.

   Make a log-log plot of the relative error in the energy norm in ordinates, defined as

$$e_r = \sqrt{\frac{U - U_h}{U}},$$

   versus the number of degrees of freedom (DOFs) (1 curve with six data points).
3. Follow the steps below to solve the problem with GFEM$^{\text{gl}}$:

   i) Solve the *initial global problem* using a uniform mesh and element size $H = L/8$. Let $u_G^0(x)$ be the solution of this problem.

ii) Define the following local problem in local domain $\Omega_L = \left\{ x | \, \frac{L}{4} < x < \frac{3L}{4} \right\}$, as illustrated below in Figure 4.

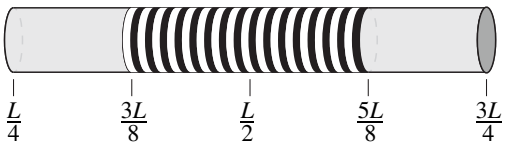

Figure 4: Local problem with heterogeneous material.

Apply the following displacement boundary conditions

$$u_L(\frac{L}{4}) = u_G^0(\frac{L}{4}),$$
$$u_L(\frac{3L}{4}) = u_G^0(\frac{3L}{4})$$

Solve for local solution $u_L(x)$ using a uniform mesh with element size $h = L/64$.

iii) Use the local solution $u_L(x)$ as enrichment at nodes of the global mesh in the enrichment zone

$$I_E = \left[\frac{3L}{8}, \frac{5L}{8} \right].$$

There are only three nodes in I_E when a mesh with $H = L/8$ is used in the global problem.

iv) Solve the *enriched global problem* on the same mesh used for the initial global problem enriched with the local solution as described above. Let $u_G^E(x)$ be the solution of this problem. Note that the stiffness matrix of the enriched global problem must be integrated using, for example, the mesh used to solve the local problem or adaptive integration.

v) Compute the relative error in the energy norm of the solution $u_G^E(x)$.

4. Repeat Task 3 for the following element sizes in the global problem: $H = \left\{ \frac{L}{16}, \frac{L}{32} \right\}$. Adopt in all cases
   i) the same element size $h = L/64$ in the local problem;
   ii) the same enrichment zone $I_E = \left[\frac{3L}{8}, \frac{5L}{8} \right]$ in the enriched global problem. Note that as the mesh of the global problem is refined, more nodes will be enriched with the local solution $u_L(x)$.

   Make a log-log plot of the relative error in the energy norm versus the number of DOFs in the enriched global problem (one curve with three data points).
5. Repeat Tasks 3 and 4 with element size in the local problem $h = L/128$ and global element sizes $H = \left\{ \frac{L}{8}, \frac{L}{16}, \frac{L}{32}, \frac{L}{64} \right\}$. Plot in log-log scale e_r of enriched global problem versus H (one curve with four data points).
6. Repeat Tasks 3 and 4 with element size in the local problem $h = L/256$ and global element sizes $H = \left\{ \frac{L}{8}, \frac{L}{16}, \frac{L}{32}, \frac{L}{64}, \frac{L}{128} \right\}$. Plot in log-log scale e_r of enriched global problem versus H (one curve with five data points).
7. Plot the solution $u_E^G(x)$ computed on the global mesh with $H = L/8$ and local mesh with $h = L/64$. You need to sample $u_G^E(x)$ at several points, not just at the nodes of the global mesh. Sample it at $x = n\Delta L$, $n = 0, 1, \ldots, 128$.
   Repeat the plot for the cases $h = L/128$ and $h = L/256$ ($H = L/8$ in both cases). Compare with the FEM solution computed on the global mesh with $H = L/8$ and the exact solution.
8. Discuss (compare and draw conclusions) about your results. What conclusions can you draw about the performance of the h–version of the FEM, GFEM$^{\text{gl}}$, for problems with heterogeneous materials? Limit your discussion to one page.

Presentation of results

Each student must submit a final project report. This report should be in the format of a technical paper. You can consult an ASCE journal (*e.g.*, Journal of Engineering Mechanics) to get an idea of what is an appropriate format for a technical paper. Handwritten papers are not acceptable. All papers must be submitted in hardcopy and in pdf. You should make the report as concise as possible, and thus do not copy material from the course material unless it is really needed. For the report, *less is more*! Data generated in your investigation must be presented in an appropriate graphical or tabular format. Figures should be clear, informative, and well labeled. Source code supporting the project must be included and documented in an appendix to the report.

Note on collaboration

The final product (report, code, results and discussion, *etc.*) must be your own individual work. You are encouraged to discuss issues pertaining to the understanding of the projects with other students in the class within reasonable and customary bounds. You must *write your own code*, you must *select your own parameter values* in your studies, and *your discussion of results should be completely independent*. You should be able to divide your development into understanding and execution. To get to understanding of a given topic is generally OK for collaboration, execution steps generally are not. Certainly, if you are sharing electronic files, you have probably gone too far. If you are unsure of what constitutes acceptable collaboration, please ask.

Evaluation

Each enumerated item above will be graded and you may get total or partial credit depending on how you addressed the item. The final grade out of 100 points you obtain for the report (and for the course), will be the average you get between the two problems. Before submitting the report, consider the following:

- **Technical Execution** Have you conquered the technical aspects of your topic well? For example, have you written your computer program correctly? Are the equations used in your implementation correct? Do you have a strategy for deciding if your answers are right (verification of implementation and equations)?
- **Communication** Have you described what you did and what you found in a manner that I can appreciate by simply reading your paper? Do you use words well? Have you organized the paper well? Do you use graphical presentation of data effectively? Does the report have conclusions?
- **Technical Insight** (Discussion) Have you gone beyond simply calculating something to actually pondering the outcome of those calculations? Can you shed an interesting light on any computed results? Your conclusions are just a summary of what you did or actually bring new insight?

References

[1] D. W. Kim, W. K. Liu, Y.-C. Yoon, T. Belytschko, and S.-H. Lee. "Meshfree point collocation method with intrinsic enrichment for interface problems". In: *Computational Mechanics* 40.6 (2007), pages 1037–1052 (cited on page 1).

[2] N. Sukumar, D. Chopp, N. Moës, and T. Belytschko. "Modeling holes and inclusions by level sets in the extended finite-element method". In: *Computer Methods in Applied Mechanics and Engineering* 190.46–47 (2001), pages 6183 –6200 (cited on pages 2, 3).

[3] N. Moës, M. Cloirec, P. Cartraud, and J.-F. Remacle. "A computational approach to handle complex microstructure geometries". In: *Computer Methods in Applied Mechanics and Engineering* 192.28 (2003). Multiscale Computational Mechanics for Materials and Structures, pages 3163 –3177 (cited on page 2).

[4] J. Plews and C. Duarte. "Bridging multiple structural scales with a generalized finite element method". In: *International Journal for Numerical Methods in Engineering* 102.3-4 (2015), pages 180–201 (cited on pages 3, 4).

B

Slip surface geometry verification

It is also possible to verify the geometry of a fully developed slip surface of the PM in addition to the verification of the CSN or FOS. This appendix shows some examples of localisation bands with finite width, computed with the SRM and the MSRM. Then the critical slip surface, computed with the SSM, is shown and compared width the localisation bands.

The FE-models and the material properties are given in Chapter 3.1. Figures B.1 up to and including B.6 show the failure modes and localisation bands of the slope, computed with the SRM and the MSRM, and the critical slip surfaces computed with the SSM (blue lines). The colours of the continuum elements represent the equivalent Von Mises strain, computed with the following expression.

$$\epsilon_{eq} = \frac{2}{3}\sqrt{\frac{3\,(e_{xx}^2 + e_{yy}^2 + e_{zz}^2)}{2} + \frac{3\,(\gamma_{xy}^2 + \gamma_{yz}^2 + \gamma_{zx}^2)}{4}} \tag{B.1}$$

Where e_{xx}, e_{yy} and e_{zz} are the deviatoric strains, defined as

$$\begin{aligned} e_{xx} &= +\frac{2}{3}\epsilon_{xx} - \frac{1}{3}\epsilon_{yy} - \frac{1}{3}\epsilon_{zz} \\ e_{yy} &= -\frac{1}{3}\epsilon_{xx} + \frac{2}{3}\epsilon_{yy} - \frac{1}{3}\epsilon_{zz} \\ e_{zz} &= -\frac{2}{3}\epsilon_{xx} - \frac{1}{3}\epsilon_{yy} + \frac{2}{3}\epsilon_{zz} \end{aligned} \tag{B.2}$$

and

$$\gamma_{ij} = 2\epsilon_{ij} \tag{B.3}$$

The equivalent Von-Mises strain is a measure for the amount of shear stress, represented as a scalar value. This value gives a good impression of the localisation band. The critical slip surface in Figure B.5 is computed for the initial values of the friction angle and the cohesion and the critical slip surface in Figure B.6 is computed at the moment of failure of the slope. The moment of failure is computed with a SRM. Then the critical slip surface is computed from this stress state. This is done to check whether the critical slip surface is different at the moment of failure, with respect to the non-reduced situation.

The failure modes and localisation bands in Figures B.1 and Figure B.2 are equal. Therefore, the SRM and the MSRM results in the same localisation band for the corresponding FE-model. The critical slip surfaces in Figures B.3 and B.4, computed with the SSM (the blue lines), are plotted on top of the failure modes of Figures B.1 and B.2. It can be observed that these critical slip surfaces are present in the localisation band. This implies that the critical slip surface, computed with the SSM in the initial phase, is an accurate approximation for the localisation bands of the SRM and the MSRM. This also indicates that the stress distribution does not change a lot until failure of the slope occurs. This last statement is enhanced by the results of Figure B.5 and B.6. The critical slip surfaces shown in these figures, indicate that the critical slip surface is not affected by the reduction of the friction angle and the cohesion. This means that the results of the SSM are robust, which is consistent with the FOSs of the SSM computed in this work.

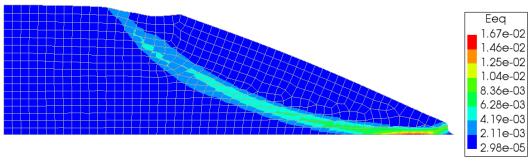

Figure B.1: Failure mode of the slope without a foundation layer, computed with the SRM with Q8 elements. The colors represent the equivalent Von Mises strain. FOS = 1.35

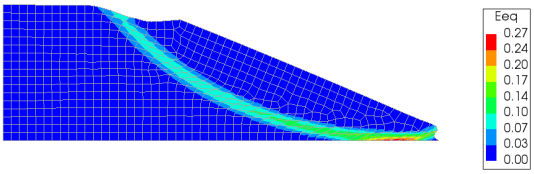

Figure B.2: Failure mode of the slope without a foundation layer, computed with the MSRM with Q8 elements. The colors represent the equivalent Von Mises strain. FOS = 1.375

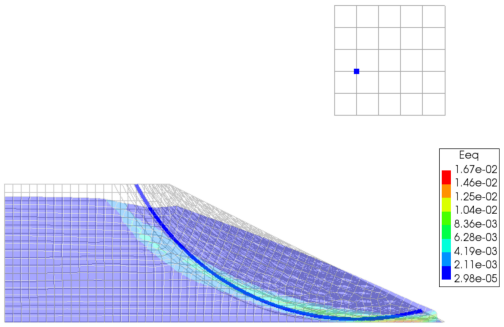

Figure B.3: The opaque colors represent the equivalent Von Mises strain at failure of the slope computed with the SRM. The critical slip surface (blue line) computed with the SSM is plotted on top. FOS SSM = 1.4.

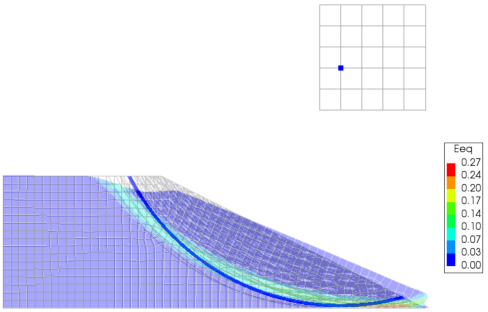

Figure B.4: The opaque colors represent the equivalent Von Mises strain at failure of the slope computed with the MSRM. The critical slip surface (blue line) computed with the SSM is plotted on top. FOS SSM = 1.4.

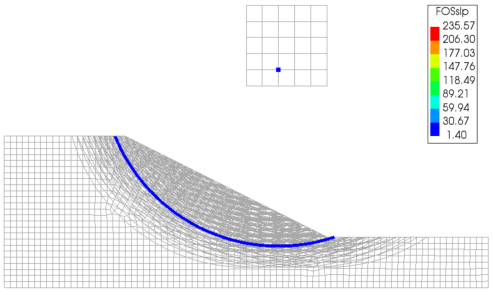

Figure B.5: The critical slip surface computed with the SSM for the initial values of φ and c. The FOS = 1.40.

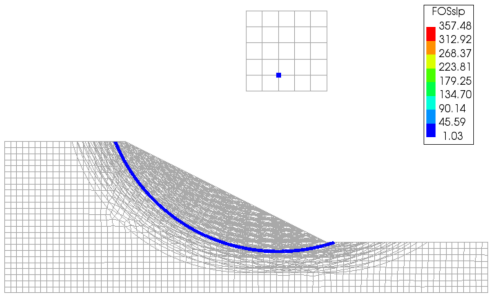

Figure B.6: The critical slip surface computed with the SSM at failure of the slope. The FOS = 1.03.

The slip surface, resulting from an analysis with the PM (combining unit weight increments with reduction of the friction angle as described in Chapter 3.4), should be compared with the critical slip surface of a SSM and with the localisation bands of the MSRM and the SRM in the verification process of the PM. The geometry of the slip surface of the PM is correct if the slip surface is similar to the critical slip surface and localisation band of the SSM and SRM/MSRM respectively. The same can be done for analyses with the PM computing a CSN (increment of the unit weight only). Then the geometry of the resulting slip surface should be verified with the localisation bands obtained by the MLIM or SLIM.

C

Results Leroy and Ortiz

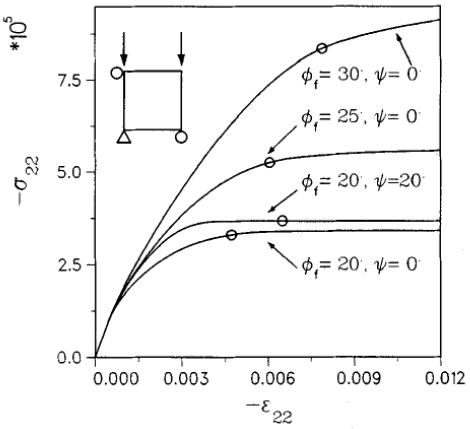

Figure C.1: Plane strain compression stress-strain curves for the material model adopted in the numerical simulations. The onset of bifurcation is indicated on each curve by a circle.

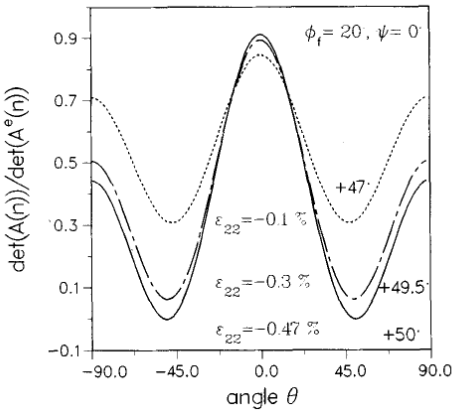

Figure C.2: Evolution of the determinant of the acoustic tensor during the plane strain compression test up to localisation.

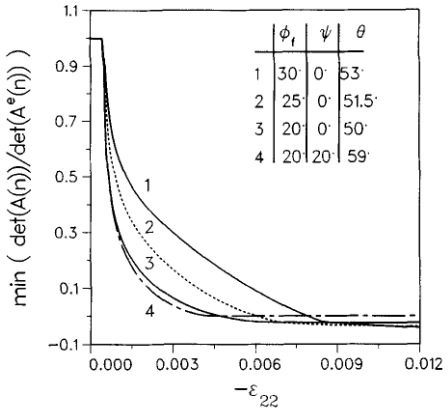

Figure C.3: Evolution of the minima of the determinant of the acoustic tensor during the plane strain compression test.

Bibliography

[1] Bishop A.W. and Morgenstern N.R. Stability coefficients for earth slopes. *Géotechnique*, 10:129–150, 1960.

[2] Diana FEA BV. 2017,. URL https://dianafea.com/manuals/d101/Theory/node71.html#SECTION05263300000000000000. accessed February 2021.

[3] Duarte C.A., Hamzeh O.N., Liszka T.J., and Tworzydlo W.W. A generalized finite element method for the simulation of three-dimensional dynamic crack propagation. *Comput. Methods App. Mech. Eng.*, 190: 2227–2262, 2001.

[4] de Borst R. *Non-linear analysis of frictional materials*. PhD thesis, Technische Hogeschool Delft, 1986.

[5] de Borst R., Crisfield M.A, Remmers J.J.C., and Clemens V. Verhoosel. *Non-linear Finite Element Analysis of Solids and Structures*. John Wiley Sons Ltd, second edition edition, 2012. ISBN 978-0-470-66644-9. p.180.

[6] de Borst R., Crisfield M.A, Remmers J.J.C., and Clemens V. Verhoosel. *Non-linear Finite Element Analysis of Solids and Structures*. John Wiley Sons Ltd, second edition edition, 2012. ISBN 978-0-470-66644-9. p.432.

[7] de Borst R., Crisfield M.A, Remmers J.J.C., and Clemens V. Verhoosel. *Non-linear Finite Element Analysis of Solids and Structures*. John Wiley Sons Ltd, second edition edition, 2012. ISBN 978-0-470-66644-9. p.179.

[8] A. Duarte A., Simone and Aragón A.M. Fundamentals of enriched finite element methods. September 2020.

[9] Griffiths D.V. and Lane P.A. Slope stability analysis by finite elements. *Géotechnique*, 49(3):387 – 403, 1999.

[10] Thomas-Peter Fries. Extended finite element methods (XFEM). pages 1–10, oct 2017. doi: https://doi.org/10.1007/978-3-662-53605-6_17-1.

[11] Simo J.C., Oliver J., and Armero F. An analysis of strong discontinuities induced by strain-softening in rate-independent inelastic solids. *Computational Mechanics*, 12:277–296, 1993.

[12] Melenk J.M. and Babuška I. The partition of unity finite element method: Basic theory and applications. *Computer Methods in Applied Mechanics and Engineering*, 139(1-4):289–314, 1996.

[13] Rudnicki J.W. and Rice J.R. Conditions for the localization of deformation in pressure-sensitive dilatant materials. *J. Mech. Phys. Solids*, 23:371 – 394, 1975.

[14] Runesson K., Ottosen N. S., and Peric D. Discontinuous bifurcations of elastic-plastic solutions at plane stress and plane strain. *International Journal of Plasticity*, 7:99 – 121, 1991.

[15] Stefan Loehnert. A stabilization technique for the regularization of nearly singular extended finite elements. *Computational Mechanics*, 54(2):523–533, mar 2014. doi: 10.1007/s00466-014-1003-7.

[16] Aragón A. M. and Angelo S. The discontinuity-enriched finite element method. *International journal for numerical Methods in Engineering*, 112(11):1589–1613, 2017.

[17] Manzari M.T. and Nour M.A. Significance of soil dilatancy in slope stability analysis. *Journal of Geotechnical and Geoenvironmental Engineering*, 126(1):75 – 80, 2000.

[18] Ottosen N.S. and Runesson K. Properties of discontinuous bifurcation solutions in elasto-plasticity. *Int. J. Solids Structures*, 27:401 – 421, 1991.

[19] Zienkiewicz O.C., Taylor R.L., and Zhu J.Z. *The Finite Element Method Its basis fundamentals*. Elsevier, 6 edition, 2005. p. 458.

[20] Liu P. Extended finite element method for strong discontinuity analysis of strain localization of non-associative plasticity materials. *International Journal fo Solids and Structures*, 72:174–189, 2015.

[21] Hill R. A general theory of uniqueness and stability in elastic-plastic solids. *Journal of the Mechanics and Physics of Solids*, 6:236–249, 1958.

[22] Regueiro R.A., Foster C.D., and Borja R.I. Embedded strong discontinuity finite elements for fractured geomaterials with variable friction. *International Journal for Numerical Methods in Engineering*, 72:549–581, 2007.

[23] Barros R.C., Vasconcelos L.A.C, Nogueira C.L., and Silveira R.A.M. Interface elements in geotechnical engineering - some numerical aspects and applications. 2017. doi: 10.20906/CPS/CILAMCE2017-0174. Conference: CILAMCE 2017 – XXXVIII Ibero-Latin American Congress on Computational Methods in Engineering.

[24] Hammah R.E., Yacoub T.E., and Curran J.H. Serviceability-based slope factor of safety using the shear strength reduction (ssr) method. ISRM-11CONGRESS-2007-285, 2007.

[25] Borja R.I., Regueiro R.A., and Lai T.Y. Fe modeling of strain localization in soft rock. *Journal of Geotechnical and Geoenvironmental Engineering*, 126(4):335–343, 2000.

[26] Sanborn S.E. and Prévost J.H. Frictional slip plane growth by localization dectection and the extended finite element method (xfem). *International Journal for Numerical and Analytical Methods in Geomechanics*, 35: 1278–1298, 2011.

[27] Belytschko T., Gracie R., and Ventura G. A review of extended/generalized finite element methods for material modeling. *Modelling and Simulations in Materials Science Engineering*, 17(17):1–24, 2009.

[28] Wang X., Yu P., Yu J., Yu Y., and Lv H. Simulated crack and slip plane propagation in soil slopes with embedded discontinuities using xfem. *Internatinal Journal of Geomechanics*, 18(12), 2018. doi: 10.1061/(asce)gm.1943-5622.0001290.

[29] Leroy Y. and Ortiz M. Finite element analysis of strain localization in frictional materials. *International journal for numerical and analytical methods in geomechanics*, 13:53–74, 1989.